University of Alberta

Influence of Nanoscale Surface Topographical Heterogeneity on Colloidal Interactions

by

Amir Ehsan Hosseini

A thesis submitted to the Faculty of Graduate Studies and Research
in partial fulfillment of the requirements for the degree of

Master of Science

Department of Mechanical Engineering

Spring 2011
Edmonton, Alberta

To my parents Saeed and Eli

Abstract

In this thesis, measurement and analysis of colloidal forces between an atomic force microscope (AFM) probe and a topographically patterned substrate are reported. The energy between the patterned substrate and a smooth flat plate was characterized mathematically using Surface Element Integration (SEI) method. Hemispherical, conical, and cylindrical shape asperities in form of either protrusions or depressions were arrayed on a square lattice to model the rough surface. The variation of DLVO interaction energies on such nano-patterned surfaces was investigated as a function of the size and density of the asperities. It was demonstrated that roughness elements attenuate the near-field DLVO energy by orders of magnitude, whereas at larger separations, their effect is insignificant. The interaction of an AFM hemispherical model probe and a rough surface was also calculated when the probe laterally moves over the surface. The resulting energy distribution maps reveal how the AFM experimental force-distance measurements can vary depending on the lateral position of the probe on the patterned substrate.

Acknowledgements

It is my pleasure to express my gratitude to my supervisor Dr. Subir Bhattacharjee for his continued source of inspiration, encouragement and support throughout my study. Not only opening the doors of the world of colloidal science to me, but as my teacher, he was the one who proved me the outcome of seriousness in work and being dedicated. I am sure that the lessons I learned from him will always accompany me during my entire life, and help me to quicker reach to my goals. Also, I would like to take this opportunity to thank Dr. Eric M.V Hoek for his valuable suggestions and advice during this research, and Dr. CJ. Kim at the University of California, Los Angeles for kindly providing the sample substrates used in this study.

My parents have always been the main reason of my consistency during my education by endowing their entire resources, support and patience, and by providing invaluable advice. I would like to acknowledge and appreciate all their effort and encouragement.

Finally, I would like to thank all of my friends, specially my colleagues in Colloids and Complex Fluids Lab including Neda, Tania, Jeff, Reeshav, Tathagata and Arnab for providing such a creative and friendly environment.

Contents

List of Tables

List of Figures

List of Symbols

A_c	$= 32\epsilon_0\epsilon_r\kappa\gamma_1\gamma_2\left(\frac{k_BT}{\nu e}\right)^2$
A_H	Hamaker constant (J)
a_p	probe radius
a_s	asperity radius / radius of the probe hemispherical head
b	cylindrical element height
c	attraction force strength characterizing constant ($= \epsilon_D\sigma^6$)
d	conical element height
dA	projected area of differential element dS
dS	differential element
e	magnitude of elementary charge ($1.602 \times 10^{-19}C$)
E_r	interaction energy between a rough and a flat surface
E_s	interaction energy between two smooth flat surfaces
h	height ($h^{'}$,$h^{''}$,H,$H^{'}$)
h	planck's constant (=6.626×10^{-34}, J)
h^*	scaled separation distance (=h/a)
h_0	minimum separation distance
$\mathbf{k}$	unit vector normal to the projected area dA
k_B	Boltzmann constant (1.38×10^{-23} JK^{-1})
M	molarity
$\mathbf{n}$	unit vector normal to the differential element dS
n_i	ionic concentration of the i^{th} ionic species (m^{-3})
$n_{i\infty}$	ionic concentration of the i^{th} ionic species in the bulk solution (m^{-3})
P	pitch distance

r	radius of the integrating element
R	asperity radius / conical asperity base radius
T	absolute temperature (K)
u_{LJ}	Lennard-Jones Potential
U_{DA}	Derjaguin interaction energy approximation
U_{VDW}	van der Waals interaction energy per unit area
U_{Hogg}	HHF expression for electrostatic interaction energy per unit area
X_0	x coordinate of the asperity origin in cartesian system
Y_0	y coordinate of the asperity origin in cartesian system
Z_0	z coordinate of the asperity origin in cartesian system
z_i	ionic valency of the i^{th} ionic species

Greek Symbols

γ_i	$\tanh\left(\frac{\nu e\psi_i}{4k_BT}\right)^2$
ϵ_D	characteristic energy for dipolar interaction
ϵ_0	vacuum permittivity (8.85×10^{-12} $\mathrm{CV^{-1}m^{-1}}$)
ϵ_r	dielectric constant of water 78.5
κ	Debye screening length ($\mathrm{m^{-1}}$)
ν	ionic valence of the electrolyte solution
ρ_i	number of atoms per unit volume within the interacting particle i
ρ_f	volumetric charge density
σ	distance of neutral approach
φ	angle between principle axes of bodies 1 and 2 in Derjaguin approximation
ψ	electric potential (V)
ψ_s	surface electric potential (V)
ψ_p	probe electric potential (V)
Ψ	dimensionless electric potential

Abbreviations

AFM	Atomic Force Microscopy/Microscope
DA	Derjaguin Approximation
DLVO	Darjaguin-Landau-Verwey-Overbeek
EDL	Electric Double Layer
HHF	Hogg-Healy-Fuerstenau
LSA	Linear Superposition Approximation
PB	Poisson-Boltzmann
SEI	Surface Element Integration
SEM	Scanning Electron Microscopy
VDW	van der Waals

Chapter 1

Introduction

1.1 Background and Overview

The term *colloid* arises from the Greek word $'\kappa o\lambda\lambda\alpha'$,- meaning glue. Colloidal particle is usually used to address the particles within the range of 10^{-9} m (1 nm) and 10^{-5} m (10 μm) in size [Russel et al., 1989]. Colloidal dispersion also refers to the suspension of colloidal particles (the dispersed phase) in a continuous medium (dispersant), where it is distinct from homogenous solutions, since the solutes (colloidal particles) do not lose their identity in a dispersion. Hence colloidal dispersion is rather considered as a heterogeneous system. There are lots of examples of colloidal systems based on their dispersed and continuous phase classifications. For instance, for suspension of liquid/solid in gas, or liquid in liquid, aerosols (*e.g.*, sprays or industrial smokes) and emulsions (*e.g.*, milk or pharmaceutical creams) are very common examples. Also for solid/gas in liquid dispersion, biocolloids (*e.g.*, blood) or clay slurries, and foams are the best examples.

Since the surface area per unit volume increases for smaller particles, in colloidal phenomena surface forces play crucial role in the interfacial interactions in colloidal systems. Some of the primary factors which contribute most in the colloidal phenomena and the strength of the interfacial surface forces are:

- Particle size and shape

Table 1.1: Magnitude of the characteristic forces: T=300 K, a=1 μm, A=10^{-20} J, $\psi_s = 0.5$ V, $\epsilon = 8.85\times10^{-10}$ C/Vm, $k_B = 1.381\times10^{-23}$ J/K [Russel et al., 1989].

$\frac{\text{van der Waals force}}{\text{Brownian force}}$	$\frac{A/a}{k_BT/a}$	≈ 1
$\frac{\text{Electrostatic force}}{\text{Brownian force}}$	$\frac{\epsilon\psi_s^2}{k_BT/a}$	$\approx 10^3$

- Surface physical and chemical properties
- Physical and chemical properties of the dispersed phase
- Particle-particle or particle continuous phase (dispersant) molecular interactions

Various interactions that are involved in the colloidal phenomena are:

- Attractive London-van der Waals
- Electrostatic repulsion or attraction (for oppositely or similarly charged particles respectively)
- Brownian force

van der Waals and electrostatic potentials are the most dominant forces in colloidal stability. Colloidal stability and interactions have fundamental importance in separation processes and many other dynamic phenomena in the concept of colloidal dispersion, such as deposition of colloids or bio-particles, filtration process [O'Meila and Stumm, 1967,Rajagopalan and Tien, 1979,Yao et al., 1971] and coagulation. They are also a major concern in other industries such as biotechnology, biochemical engineering and material science. In this regard, the surface quality and physical property is accounted as one of the central problems in enhancing the bio-compatibility of these organs in the body. For instance, it was observed that the rate of adhesions between the

proteins and their biological responses are crucially affected over surfaces with different levels of physical heterogeneities [Brunetti et al., 2010].

1.2 Objectives and Scope

Surface roughness is one of the main concerns in different colloidal phenomena (*e.g.*, deposition), specially when the colloidal interactions are in interest. In this research, it has been primarily attempted to investigate and characterize the variation of colloidal interactions as a result of the surface roughness. Consequently, the impact of surface physical heterogeneities on the rate of particle capture and colloidal deposition can be addressed and clarified. Therefore, it was initially tried to experimentally measure the colloidal forces over a smooth surface. In following, it was attempted to observe the significance of the surface heterogeneities on the measured interactions by conducting the experiments over rough surfaces. In this regard, atomic force microscopy (AFM) [Binnig et al., 1986] was used as a powerful technique to measure the forces between the AFM probe and different set of surfaces.

AFM is mainly used to detect and quantify the topography of a surface and determine the morphological parameters of the nano-structured substrates. However, apart from its primary role of scanning the surfaces, this technique is now widely used to evaluate the near-field interactions due to it high motion sensitivity. Thus, in the experimental phase of this study, the AFM is used both for determining the roughness of the sample substrates, and measuring the interfacial forces, where the different behaviour of the measured forces are ascribed to the morphological properties of the used substrates.

Once the impact of the surface roughness is experimentally observed, the physics behind is tried to be revealed and be interpreted theoretically. This is accomplished through developing and conducting a set of mathematical analyses, in which the behaviour and variation of the colloidal forces are described by considering the roughness. For the characterization of these energy variations, a set of novel analytical equations are derived that comprehensively

elucidate the exact interaction energies between a flat and a rough surface. The roughness elements are modeled as protruding and depressed structures in three different shapes, which are uniformly patterned on the surface. This is to generalize the energy characterization, while simplifying the problem and avoiding the inclusion of unnecessary mathematical constraints, such as random roughness statistical parameters into the calculations.

In addition, the interaction between a spherical particle, which represents the AFM probe by bearing its material property, and a model rough surface is simulated, and geometrically analyzed. This is to assess the precision of the experimentally achieved results from AFM by showing how the obtained energy may vary as a function of the lateral position of the probe over the surface. Finally, the spherical probe, used in the simulations, is modified to a structure that better represents the actual shape of a real AFM probe. The interaction of such a modeled probe with a flat surface is then numerically calculated. By changing the characteristic dimensions of the modeled probe, in this study, it is tried to investigate that how these sizes can change the results. Also, this phase of the research shows how much precision is required, if one is interested to simulate the AFM force measurement process by simulating the exact structure of an AFM probe.

To summarize, the main objectives of the current study are:

a) Measure and quantify the colloidal forces experimentally between an AFM probe and a smooth surface under different conditions to observe overall behaviour of these forces as a function of the separation distance.

b) Conduct AFM force measurements over rough surfaces, to experimentally demonstrate the paramount effect of the surface heterogeneities on the colloidal interactions.

c) Develop theoretical analyses that enable us to characterize the changes in the interaction energy as a result of the surface roughness by providing analytical derivations.

d) Numerically simulate the interaction energy between a spherical probe and a uniformly patterned rough surface as a function of separation distance. This simulation provides the energy distribution as the approaching probe changes its lateral location over the interacting surface.

e) Try to model the exact structure of an AFM probe, and proving the changes in its interaction with a flat surface as a result of varying its geometrical characteristic parameters.

1.3 Organization of the Thesis

This chapter has briefly introduced the colloidal systems along with some of their major applications, where the colloidal interactions are in main interest. The objective of the present research is then described. In Chapter 2, the colloidal forces introduced and their corresponding mathematical equations are defined. Also, a literature survey based on the existing studies about the impact of the surface roughness in different areas along with their correlation with the colloidal interactions is provided. The literature survey also provides information about the previous attempts trying to explain the effect of surface roughness, where the lack of theoretical works is discussed, which creates the milestones of the present theoretical derivations. Chapter 3 presents the theoretical methodology and the mathematical details including all the analytical derivations and the path for numerical calculations. In Chapter 4, AFM force measurement process is briefly introduced, followed by the information about the experimental setup (AFM probe and rough substrates used in the force measurement tests). Chapter 5 presents all the experimental and theoretical results and provides a discussion on the colloidal interaction characterizations for rough substrates based on these results. Finally, in chapter 6, some important conclusions are drawn according to the presented research, where a few suggestions for future studies regarding the particle-surface interactions are also provided.

Chapter 2

Influence of Surface Roughness on Colloidal Interactions

2.1 Introduction

Accurate knowledge about colloidal interaction energies provides critical insights into the behavior of diverse colloidal and interfacial processes, including colloidal particle dispersion, membrane fouling, deposition, adhesion, and heterocoagulation phenomena [Brant and Childress, 2002, Dorobantu et al., 2008, Elimelech et al., 1997, Kihira and Matijevic, 1992, Rizwan and Bhattacharjee, 2007, van Oss, 1993, Zhao et al., 2008]. Moreover, understanding of colloidal interactions are seen to have immense applications in biological and microbial science, such as investigating the biological response or enhancing the bio-compatibility of the neuron cells [Brunetti et al., 2010, Moxon et al., 2004], or examining the functionality of nano-structured biomaterials in simulation of the implanted tissues such as bones [Palin et al., 2005]. Furthermore, a deep knowledge of colloidal interactions seems to be inevitable in the characterization of clay dispersion [Zhao et al., 2008] and stabilization of the oil droplets in oil/water emulsions and their interfacial energies [Liu et al., 2006].

Colloidal forces are basically described by a model originally proposed by Derjaguin, Landau, Verway, and Overbeek, namely, (DLVO) theory [Verwey and Overbeek, 1948, Derjaguin and Landau, 1941]. In this model, the total intermolecular potential energy between two colloidal entities is determined by

considering the attractive London-van der Waals and repulsive electrostatic energies. DLVO theory is based on the assumption of ideally smooth interacting surfaces with uniform physical and chemical properties; however, in real applications, physical and chemical heterogeneities are unavoidable [Bowen et al., 2002]. Many studies have reported significant discrepancies between theoretical interaction forces predicted from DLVO theory, and experimentally measured interactions [Bowen and Doneva, 2000,Bowen et al., 2002]. Some studies ascribed the inconsistency between the theoretically calculated and experimentally observed interactions predominantly by the presence of other short range non-DLVO interactions [Brant and Childress, 2002,Dorobantu et al., 2009,van Oss, 1993]. However, among other factors such as chemical heterogeneities of the interacting colloidal particles, or the properties of the intervening medium, surface physical heterogeneities (roughness) can be considered as a dominant factor in order to reconcile this discrepancy.

In this chapter, each of the DLVO interaction energy components are introduced, and different approaches used to describe these interactions between colloidal entities in a colloidal system and their limitations are discussed. In the following, the previous works discussing about the impact of the surface topographical heterogeneities on the colloidal interactions from experimental observations, and earlier interpretations for the departure between the experimentally observed and theoretically predicted interaction energies have been discussed.

2.2 DLVO Theory

The overall interfacial interaction between two colloidal entities is generally described by combining the attractive London-van der Waals and repulsive electric double layer effect interactions. This forms the basis of the *DLVO Theory* which was developed by Derjaguin, Landau , Verwey and Overbeek [Verwey and Overbeek, 1948,Derjaguin and Landau, 1941]. In this theory, it is assumed that these two interactions are linearly additive, meaning that they can be cal-

culated separately and added up to form the total interaction. Traditionally, different approaches were developed, which by using this theory, tried to describe the colloidal interactions between known geometries, for instance two surfaces, in colloidal systems. However, there are also some inherent assumptions in these approaches that stem from the manner in which the individual components of the potential energies are calculated. For instance, the surface of the interacting bodies are assumed to be flat, and any kind of physical or chemical heterogeneities are ignored in the computation process. Moreover, the intervening solvent is treated as a continuum media, where the size and granular geometries of the ions are neglected.

2.2.1 London-van der Waals Potential

London-van der Waals interaction is an attractive atomic and molecular force between molecules and particles. This interaction is caused due to the simultaneous fluctuation of the electronic cloud around the molecules in two neighboring materials, which creates instantaneous dipoles in the molecules. These spontaneous dipoles in molecules can also be induced by the absorbtion of photons in the ambient. However, once the molecules are brought very close together, the electron clouds overlap, causing the molecules to experience a strong repulsion. Lennard-Jones potential summarize such a behavior by including both attractive and repulsive forces between a pair of atoms in the form of:

$$u_{LJ} = \epsilon_D \left[\left(\frac{\sigma}{r}\right)^{12} - \left(\frac{\sigma}{r}\right)^{6} \right] \tag{2.1}$$

In this equation, ϵ_D is the characteristic energy for dipolar interaction, σ is the constant representing the distance of neutral approach, and r is the separation distance. The first term in Eqn. (2.1) denotes the repulsive force when the atomic electron clouds overlap, when the second negative term, represent the attraction force. The repulsion term, known as Born repulsion, is dominant at separations between 0.1 to 0.3 nm.

The van der Waals interaction for large bodies can be calculated through either a macroscopic model attributed to Lifshitz, or based on the Hamaker's

[Hamaker, 1937] microscopic model. However, due to complexity of the macroscopic Lifshitz model, the van der Waals interaction energy for large colloidal geometries are obtained by employing Hamaker approach. In this model, by defining a cut-off distance of 0.158 nm [Russel et al., 1989], as the closest separation distance possible between two interacting bodies, the van der Waals energy in Lennard-Jones potential is simplified as:

$$u_{LJ} = -\frac{c}{r^6} \tag{2.2}$$

where according to Eqn. (2.1), $c = \epsilon_D \sigma^6$ is a constant characterizing the strength of the attraction between atoms. Employing Hamaker approach, one is able to evaluate the van der Waals energy between two macro-bodies by integrating the Eqn. (2.2) over their entire volume of any arbitrary shapes. In this approach, there are few assumptions considered for such a calculation. Firstly, the interactions between the atoms are assumed to be pairwise additive. Secondly, the density of the atoms in the particles is uniform. According to this model, the van der Waals interaction energy per unit area between two infinite flat plates, separated by a distance of h, is described as:

$$U_{VDW}(h) = -\frac{A_H}{12\pi h^2} \tag{2.3}$$

In this equation, $A_H = \pi^2 c \rho_1 \rho_2$, which is a function of the material properties, is called Hamaker constant, where, ρ_1 and ρ_2 are the number of atoms per unit volume within the interacting particles. It must be noted that the above expression is for non-retarded van der Waals interaction, when the speed of light is assumed to be infinite. Otherwise, the retarded expression has to be considered by including a coefficient as a function of h. Further details are available in the text books by Israellachvili [Israelachvili, 2007], and Masliyah & Bhattacharjee [Masliyah and Bhattacharjee, 2006]. In a similar manner, one may find the van der Waals energy of a flat surface interacting with a sphere, or the energy between two spheres with identical or different radii.

2.2.2 Electric Double Layer Potential

As mentioned earlier in this section, the second component of DLVO theory accounts for the electric double layer or electrostatic interaction energy for modeling the colloidal interactions. This interaction is originated based on the presence of free ions in an electrolyte solution and their interaction with charged surfaces. Solid surfaces and colloidal particles usually attain surface charge when they are intervened in an aqueous media. There are different charging mechanisms through which the surfaces attain charge. For instance, the surfaces can acquire charges by means of dissociation of surface groups (such as COO^-, or NH_3^+), dissolution of the ions from surfaces of sparingly soluble crystals, or by adsorption of the surfactants ions onto the surface [Hunter and White, 1987]. Due to electro-neutrality of the system, the overall surface charge of the immersed body should be exactly equal, but opposite to the ionic charge of the electrolyte solution in each of the mechanisms mentioned above. Absorbtion of counter-ions from the aqueous media to the surface of a charged plate creates a well-known phenomenon of *electric double layer* effect, where two layers of oppositely charged ions surround each side of the plate.

The electrostatic interaction is governed by Poisson-Boltzmann (PB) equation. The spatial distribution of the ions, normal to the charged surface, is explained by Boltzmann distribution.

$$n_i = n_{i\infty} \exp\left(-\frac{z_i e \psi}{k_B T}\right) \tag{2.4}$$

where n_i is the ionic concentration of the i^{th} ionic species at a state where the electric potential is equal to ψ, and $n_{i\infty}$ is the ionic concentration at far separation distances in bulk medium where $\psi = 0$. z_i is the ionic valency, which its sign is determined to be either positive or negative depending on whether the ion is an anion or a cation. $k_B = 1.38 \times 10^{-23}$ JK^{-1} is the Boltzmann constant, and $T = 298$ K is the room temperature. Using the above equation, one is able to analyze the ionic spatial distribution in double layers, or more precisely, relate the spatial variation of the electric potential

to the ionic concentration or vice versa at different locations in diffuse electric double layers.

Poisson's equation on the other hand, describes the distribution of electric potential in a dielectric material carrying free charges, and it is an appropriate equation where the electric permittivity of the medium is assumed to be constant.

$$\epsilon \nabla^2 \psi = -\rho_f \tag{2.5}$$

In the above equation, ϵ is the constant electric permittivity of the aqueous medium, ψ is the electric potential, and ρ_f is the volumetric charge density of the free ions that can be defined as follows:

$$\rho_f = \sum_{i=1}^{N} z_i e n_i \tag{2.6}$$

where z_i and n_i have the same definition as in Eqn. (2.4), e is the magnitude of the elementary charge (1.602×10^{-19} C), and N is the total number of the ionic species in the electrolyte solution. Combining the Eqns. (2.4, 2.5, and 2.6), for one-dimensional variation, it gives rise to the well-known Poisson-Boltzmann (PB) expression as following:

$$\epsilon \frac{d^2\psi}{dx^2} = -\sum_{i=1}^{N} z_i e n_{i\infty} \exp\left(-\frac{z_i e \psi}{k_B T}\right) \tag{2.7}$$

PB equation determines the distribution of the electric potential in the diffuse double layer as a function of separation distance normal to the charged surface. To simplify the problem, if a symmetric ($z:z$) electrolyte solution is considered as the intervening medium (*e.g.*, NaCl, KCl, or $CuSO_4$), the Eqn. (2.7) can be written as:

$$\epsilon \frac{d^2\psi}{dx^2} = 2zen_\infty \sinh\left(\frac{ze\psi}{k_B T}\right) \tag{2.8}$$

This is called *Gouy − Chapman Theory* which is a nonlinear theory. Considering an appropriate boundary condition where surface potential $\psi = \psi_s$ at $x = 0$, and at $x = \infty$, the potential ψ is equal to zero, the previous equation has the solution as following:

$$\Psi = 2 \ln \left[\frac{1 + \exp -\kappa x \tanh(\Psi_s/4)}{1 - \exp -\kappa x \tanh(\Psi_s/4)}\right] \tag{2.9}$$

where the dimensionless potential Ψ is:

$$\Psi = \frac{ze\psi}{k_B T} \tag{2.10}$$

and similarly, $\Psi_s = ze\psi_s/k_B T$ is the dimensionless surface potential. The parameter κ in Eqn. (2.9) is called *Debye length*, and κ^{-1} defines the thickness of the electric double layer. In the other word, Debye length represents a characteristic length in which the electric potential drops to approximately 33% of its value at the charged surface. This parameter is defined as:

$$\kappa^{-1} = \left(\frac{\epsilon k_B T}{2e^2 z^2 n_\infty}\right) = \frac{3.04}{z\sqrt{M}} \times 10^{-10} \tag{2.11}$$

where the second expression is applied only for symmetric electrolyte solutions. Debye-Hückel approximation provides a linearized form of the PB equation, Eqn. (2.7), when the surface potential $\psi_s \ll 0.025$ V, as in the following equation.

$$\frac{d^2\psi}{dx^2} = \frac{2e^2 z^2 n_\infty}{\epsilon k_B T}\psi = \kappa^2 \psi \tag{2.12}$$

Hence, under similar boundary conditions as for Eqn. (2.8), one may obtain the following solution for electric potential ψ based on the Debye-Hückel approximation as:

$$\psi = \psi_s \exp(-\kappa x) \tag{2.13}$$

Further analysis has been conducted by Hogg, Healy, and Fuerstenau (HHF) [Hogg et al., 1966] to determine the electrostatic interaction energy per unit area between two flat surfaces based on the Debye-Hückel approximation:

$$U_{Hogg}(h) = \frac{\epsilon\kappa}{2}\{(\psi_1^2 + \psi_2^2)[1 - \coth(\kappa h)] + 2\psi_1\psi_2 \mathrm{cosech}(\kappa h)\} \tag{2.14}$$

For using the above equation some important assumptions have to be taken care, in order to prevent any error in the energy calculations. Firstly, as explained for Debye-Hückel approximation, this derivation is only valid for low surface potentials, and symmetric electrolyte solutions. Secondly, the surfaces of the interacting plates are assumed to be perfectly smooth (similar condition in Hamaker approach for van der Waals potential energy). It is also

pertinent to mention that HHF expression can be applied for either constant surface potential, or constant charge density boundary conditions. However, in this research, the constant surface potential boundary condition is considered, since it has been indicated in other attempts [Carnie and Chan, 1993, Gregory, 1973, Gregory, 1975, McCormack et al., 1995] that the linearized form of the PB equation, seriously overestimates the electrostatic interaction under the constant surface charge condition.

Another expression for electrostatic interaction energy per unit area for two parallel flat plates is given by *Linear Superposition Approximation* (LSA) [Bell et al., 1970] as following:

$$U_{LSA}(h) = 32\epsilon_0\epsilon_r\kappa\gamma_1\gamma_2\left(\frac{k_BT}{\nu e}\right)^2\exp\left(-\kappa h\right) \tag{2.15}$$

$$\gamma_i = tanh\left(\frac{\nu e\psi_i}{4k_BT}\right)^2 \tag{2.16}$$

where $\epsilon_0 = 8.854 \times 10^{-12}$ $\mathrm{CV^{-1}m^{-1}}$ is the vacuum permittivity, $\epsilon_r = 78.5$ is the dielectric constant of water, ν is the ionic valence of the symmetric electrolyte equal to 1, and ψ_i is the surface potential of each interacting plate. LSA equation can be reasonably replaced by HHF equation for evaluation of the electrostatic interaction; however it facilitates the analytical derivations related to electrostatic energy due to its simpler mathematical form. In this research, both of these equations are employed in numerical analyses, but only LSA expression is used for analytical characterizations.

2.3 Scaling the Interaction Energy between Flat Surfaces to the Corresponding Energy of Curved Bodies

So far, the equations provided for interaction energies in section 2.2 represent the energy per unit area for two smooth flat plates. The expressions derived in the last section, can also be derived for other simple geometries, such as spherical bodies. Nonetheless, to include the effect of surface roughness for

energy calculation in the realistic colloidal systems, one may need to employ some other techniques which can enable to calculate the interaction between curved or even arbitrary geometries. On the other hand, Hamaker approach is only applicable for van der Waals interaction, while HHF and LSA expressions (*i.e.*, Eqns. 2.14 and 2.15) are derived from other mathematical paths, and they also fail to determine the electrostatic energy between macrobodies with more complicated shapes. In the following subsections, two celebrated techniques are introduced that provide the opportunity to evaluate the DLVO interaction energy components for curved geometries.

2.3.1 Derjaguin Approximation

This technique was first proposed by Derjaguin in 1934 [Derjaguin, 1934], when he found that the energy for two interacting spheres at very close separations can be approximated by the interactions between two flat plates at a similar separation distance. Later, this technique was further generalized by White [White, 1983], such that the interaction energy between two curved macrobodies with principle radii of R_1 and $R_1^{'}$ for body 1, and R_2 and $R_2^{'}$ for body 2 can be approximated according to the following equation.

$$U_{DA}(D) = \frac{2\pi}{\sqrt{\lambda_1\lambda_2}} \int_D^{\infty} \frac{U(h)}{A} dh \tag{2.17}$$

where the interaction energy per unit area between two flat surfaces $U(h)$ is rescaled to U_{DA} that is the interaction energy per unit area between the two curved bodies. The closest separation distance is h, and the parameter $\lambda_1\lambda_2$ is defined as:

$$\lambda_1\lambda_2 = \left(\frac{1}{R_1} + \frac{1}{R_1^{'}}\right)\left(\frac{1}{R_2} + \frac{1}{R_2^{'}}\right) + \sin^2\varphi \left(\frac{1}{R_1} - \frac{1}{R_2}\right)\left(\frac{1}{R_1^{'}} - \frac{1}{R_2^{'}}\right) \tag{2.18}$$

Derjaguin approximations (DA) is a useful technique for predicting the energies between curved surfaces, and it can be used identically for both the van der Waals and electrostatic potentials. Yet, this approximation fails to accurately predict the corresponding energy when the interacting bodies are

located at farther separations, or their radii of curvature are in the same size as the separation distance. These limitations can be written in form of:

$$\frac{L_0}{R_0} \ll 1$$
$$\frac{D}{R_0} \ll 1 \tag{2.19}$$

where L_0 is the length scale that the interaction energy decays to zero, and R_0 is the smallest radius of curvature of the two interacting bodies. The limitations explained above, severely restrict the application of the DA in calculation of energy when the roughness of the surface is considered. Specially, when the size of the surface heterogeneities are equal or even less than the size of the approaching curved body. This may also leads to huge errors when the energies are calculated at far distances.

2.3.2 Surface Element Integration

As discussed in section 2.3.1, the DA technique has major shortcomings in terms of the accuracy, when the actual topography of the surface is required to be considered. Particularly, in this research, where the surface roughness is the main criteria in characterization of the colloidal interactions, one may need to implement another mathematical method to be able to assess these interactions based on the exact morphological parameters of the surface. In this regard, the well-known *surface element integration* (SEI) technique [Bhattacharjee and Elimelech, 1997], which is widely used in simulation and modeling of different colloidal phenomena, where the colloidal interactions and the morphological parameters of the surfaces are of great interest. This technique can be employed for both the van der Waals and electrostatic potential energies. The basis of the SEI approach is that the total interaction energy between two macrobodies with arbitrary shapes are obtained by integrating the interaction energy per unit area between two infinite flat plates over the both surfaces surrounded in the projected areas between the interacting bodies.

Using the $U(h)$ expressions provided in Eqn. (2.3) for non-retarded van

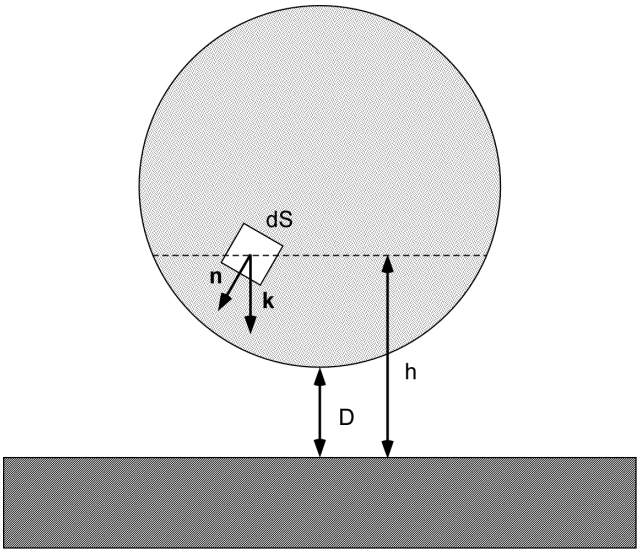

Figure 2.1: 2D schematic illustrating the differential element dS, separated with a distance h, in a spherical particle interacting with a flat plate, where the closest distance between the two bodies is D. $\mathbf{n}$ is a unit vector normal to dS element, and $\mathbf{k}$ is the unit vector normal to the projected area dA of element dS over the flat plate.

der Waals, and Eqns. (2.14 or 2.15) for electrostatic potenial energy per unit area, the energy between a small element dS (see Figure 2.1) and a flat plate is derived as $dU = \mathbf{n}.\mathbf{k}U(h)dS$. Therefore, the total energy between the two bodies is given as:

$$\begin{aligned} U(D) &= \int_S \hat{\mathbf{n}}.\hat{\mathbf{k}}U(h)dS \qquad (2.20) \\ &= \int_A \frac{\hat{\mathbf{n}}.\hat{\mathbf{k}}}{|\hat{\mathbf{n}}.\hat{\mathbf{k}}|}U(h)dA \\ &= \iint_{x,y} \frac{\hat{\mathbf{n}}.\hat{\mathbf{k}}}{|\hat{\mathbf{n}}.\hat{\mathbf{k}}|}U(h)dxdy \end{aligned}$$

where dA is the projected area of the differential element dS over the flat plate. The result of the above integration for van der Waals interaction energy for a sphere of radius a interacting with a flat plate is identical to the van der Waals energy expression, calculated based on the Hamaker approach for such a system.

$$U_{SEI}(D) = -\frac{A_H}{6}\left[\frac{a}{D} + \frac{a}{D+2a} + \ln\left(\frac{D}{D+2a}\right)\right] \tag{2.21}$$

However, as explained earlier, SEI technique is not restricted to only simple geometries, and may be employed to more complicated shapes by reducing the number of integrations in Hamaker approach, but it also can be implemented for calculation of electrostatic energy.

2.4 Surface Roughness and Colloidal Interactions

Many studies have announced major disagreements between the theoretically calculated colloidal interactions according to the DLVO theory, and their real values based on the experimental evidences in various colloidal systems. Bowen and Doneva [Bowen and Doneva, 2000] used atomic force microscopy in conjunction with the colloidal probe technique for quantifying the fouling at different locations of a rough membrane in a NaCl electrolyte solution. It was observed in their experiments that the magnitude of the EDL repulsion predicted by DLVO theory at the valleys was greatly overestimated. Later, in extension to their experiments, they incorporated a numerical solution for non-linear PB equation for a surface constant charge boundary condition, and they observed that the discrepancy between theory and experiment is higher at higher ionic strengths [Bowen et al., 2002]. Elimelech *et al.* [Elimelech et al., 1997] also reported that the use of DLVO energy might not accurately explain the experimental observations for the fouling of silica colloids onto composite membranes.

Brant and Childress [Brant and Childress, 2002] showed that the DLVO theory might not support the experimental fouling behavior on highly hydrophobic surfaces at very short ranges due to its weak attractive van der Waals part. Zhao *et al.* [Zhao et al., 2008] also studied about the clay dispersion by investigating the colloidal interactions of a silica sphere, used in the AFM colloidal probe technique, with a clay basal plane and edge surfaces.

While the force profiles in plane surface (pH independent) can be well fitted with DLVO theory prediction, the force profiles at edged surfaces could not reasonably be fitted with the classical DLVO theory. Dorobantu *et al.* [Dorobantu et al., 2008] experimented the microbial adhesion to the surfaces by examining the interacting forces between AFM probe and bacterial species exhibiting different phyisiochemical cell surface properties. Similar to the previous works, the AFM profiles could not be described by the classical DLVO theory.

2.4.1 Inclusion of non-DLVO forces

Some studies explained the inconsistency between the theory and experimental works through the presence of other non-DLVO forces. For instance, Van Oss [van Oss, 1993] reviewed the roll of acid-base (AB) interfacial interactions as the driving force for hydrophobic attractions, and for hydrophilic repulsions in excess to long-range van der Waals and short-range electrostatic energies (Extended- DLVO). In that review, the salient aspects of including the acid-base interactions were inspected in various applications such as particle suspension, protein adsorption, and cell-cell interaction. In summary, the use of AB interactions in colloidal systems depicted novel aspects of the total interaction energy between the particles at different ranges.

Similarly, Brant *et al.* [Brant et al., 2006] has also tried to justify the interaction energies between mica and polymeric surfaces within the framework of extended DLVO theory by inclusion of AB interactions. Dorobantu *et al.* [Dorobantu et al., 2009] conducted an extensive research on the adhesion of the AFM tip to the bacterial species. Similarly, they have reported a difficulty in explaining the experimentally achieved forces based on the DLVO interaction theory. Consequently, they attributed the observed deviation to the presence of acid-base interactions and other steric interactions due to the structure of the bacterial cell surfaces to form the extended DLVO model. In their attempt, it was shown that by accounting the acid-base forces in the theory, the experimental results have come to closer agreement with theory.

2.4.2 Experimental Works Reporting the Effect of Surface Roughness

As an alternate approach, and apart from the inclusion of other non-DLVO forces or the chemical heterogeneities [Kemps and Bhattacharjee, 2005,Rizwan and Bhattacharjee, 2009] of the surfaces, some other works have addressed the profound influence of the physical heterogeneities or roughness of the interaction membranes as a possible source of error in the experimental force measurements. Initially, Elimelech and O'Melia [Elimelech and O'Melia, 1990] investigated the rate of the polystyrene particles deposition onto glass beads in a porus media, and addressed a severe contrast with theory, in that the variations of the deposition rate with respect to the ionic concentrations were insensitive to the polystyrene particles size. They further explained that as one possibility, this has been observed due to the failure of the DLVO theory to consider the roughness of the surface.

Likewise, in their membrane fouling inspection, Bowen and Doneva [Bowen and Doneva, 2000] have quantified the influence of the membrane roughness on the adhesion rate of the silica particles onto the rough surfaces consisting of peaks and valleys. They experimentally observed that the particle adhesion rate may vary in peaks and in valleys up to more than a factor of 20, having less magnitudes at the peaks. They have also assessed that the low adhesion can be described by theory, while higher deposition rates must be ascribed to the surface roughness. Furthermore, they have advocated the demand of accounting for exact shape of surface roughness in future computational works using surface element integration (SEI). However, by developing a numerical solution for non-linear PB equation [Bowen et al., 2002], they successfully characterized the deviation of the experimental observations in membrane fouling from the theoretical expectations for EDL energy. In this regard, they interpreted that this departure increases as the surface roughness become greater in magnitude than the Debye length of the used electrolyte solution.

Considine and Drummond [Considine and Drummond, 2001] employed AFM to measure the interaction force between the pairs of silica colloids (pos-

sessing nano-scale roughness), where one particle was attached to the AFM probe, and the other one was mounted on an oxidized silicon wafer. Similar to the previous works, DLVO theory had only partial agreement with the force-separation curves, in a way that the experimental force-separation curves did not manifest weak van der Waals forces expected theoretically. They finally proposed the surface roughness as a possibility for attenuation of the van der Waals force during the experiments. Brant *et al.* [Brant et al., 2006] have also added that surface roughness is a possible source of error between the measured zeta potential of the surface and its original value under higher ionic strengths when the Debye screening length is in the range of the surface nano-scale heterogeneities. In the other words, the impact of roughness on the measurement of the surface potential increases as ionic strength increases. Rizwan and Bhattacharjee [Rizwan and Bhattacharjee, 2007] have also reported that profound influence of surface asperities on the deposition of polystyrene particles onto composite membranes specially when the radii of the particles are less than the size of the surface heterogeneities.

Similarly, in a research conducted by Zhao *et al.* [Zhao et al., 2008], the force profiles obtained for the interaction of the silica colloidal probes with the clay basal surfaces (with random roughness) could not be reasonably fitted classical DLVO theory, unless they considered the surface roughness. They additionally observed that the resulting interactions are sensitive to the position of the probe over the surface, meaning that the random roughness will result in changing the behavior of the force profiles. In a recent study [Kang and Elimelech, 2009], the interaction forces of live cell probes and quartz surfaces were investigated with AFM, which states that the widely scattered force distributions for the live cell probes are generally attributed to the roughness (heterogeneities) of the cell surfaces.

2.4.3 Numerical Analyses Based on Surface Roughness

In the previous subsection, some of the existing experimental studies depicting the impact of surface morphology on colloidal forces were shown. It was dis-

cussed that according to some experimental observations, the deviation of the interaction forces from the expected theoretical values implicated the presence of surface physical heterogeneities, and their effect on colloidal interactions. In this section, however, some earlier studies in which the influence of surface roughness has been attempted to be mathematically analyzed in order to reconcile the reported inconsistency, are briefly discussed in accordance to their published year.

In a very first effort, Suresh and Walz [Suresh and Walz, 1996] tried to investigate the effect of roughness on a particle than a surface. So, they simulated rough polymeric particles interacting with a flat surface. They developed a set of analytical equations for determining the van der Waals and electrostatic interaction energy between a particle consisting hemispherical asperities of fixed radii and a smooth plate. van der Waals component was calculated based on the Hamaker approach, while the electrostatic energy was calculated by employing linear superposition approximation (LSA). In these calculations, they assumed that the hemispherical asperities on the particle surface are treated as spheres, and that the total interaction is achieved by summation of the interaction of the particle and the interaction of the individual asperities on its surface. Accordingly, the effects of asperity size and density were investigated, and it was concluded that at closer separations the repulsive barrier in the DLVO theory is lower, hence the rate of particle capture is higher. This yield to qualitative agreement with experiments.

Bhattacharjee *et al.* [Bhattacharjee et al., 1998] employed surface element integration technique, bypassing the limitations in Derjaguin's approximation DA, to determine the DLVO interaction potentials over a rough surface interacting with a flat plate. The roughness in their study was introduced by defining a set of randomly distributed asperities in form of hemispherical protrusions and depressions. In a second approach, the roughness was applied as uniform ripples on the surface of a sphere, where it was interacting with a flat surface. The corresponding interaction energy in both cases were then compared with the case of two flat plates and a flat plate interacting with a

pure sphere respectively, separated by a equivalent distance to the mean separations between the model rough surfaces and the flat plate. HHF equation was used for EDL interaction. For both cases, the resulting interaction energies were considerably reduced, specially at closer separations, depicting that even minor asperities on the surface of a particle can considerably attenuate the interactions.

In a similar Endeavor, Hoek *et al.* [Hoek et al., 2003] revealed the consequences of surface roughness on colloidal deposition and fouling phenomena by employing surface element integration for their numerical calculations. The calculations for EDL component is based on the HHF expression. In their study, the interaction of a rough surface, comprising hemispherical protrusions and depressions of different radii, was investigated with a spherical probe rather than a flat surface. Different modeled rough surfaces were supposed to simulate some actual polymeric surfaces. DLVO Energy of the spherical probe was evaluated at different separation distances over the model rough surface. It was reported that the heterogeneities significantly altered the magnitude of the DLVO interaction energy, such that it makes the surface more favorable for deposition.

Later in 2006, in accordance to the previous study, Hoek *et al.* [Hoek and Agarwal, 2006] investigated the roughness effect based on the extended DLVO approach using surface element integration. Additionally, they provided a very brief discussion about the geometrical consideration about minimum separation distance, which helped in justifying the interaction energy between the rough surface and spherical particle for protrusive and depressive hemispherical elements over the surface. In this regard, they discussed that even with a similar minimum separation, the resulting energy is higher when the particle is trapped in a depressive element, having lower average surface separation with the opposite surface. Apart from this discussion, they have attempted to determine the minimum, average and maximum interaction energy over each of the modeled surfaces.

Martines *et al.* [Martines et al., 2008] implemented Hamaker and HHF

expressions into the surface element integration to analyze the interaction between a large (micro-scale) sphere with a rough surface patterned with protruding and depressive nano-scale cylinders that are distributed in a square lattice. The interaction energies were acquired for different heights and cross-sectional diameters of the asperities, and it was found that the asperity diameter is a more influential parameter. Again, in this work, the results illustrated that the protruding cylindrical asperities cooperate in higher rate of deposition by lowering the repulsive energy barrier, meaning that cylindrical depressions induced less significant changes in the DLVO energy than the protruding elements. They addressed that this is observed more when the radius of curvature of asperities decreases.

In Zhao *et al*. [Zhao et al., 2008] study, the interaction energy between an infinite half space and a rough surface has been numerically evaluated by employing surface element integration. The rough surface is reconstructed based on the topographical parameter of edged clay basal surfaces which was used in their experimental force measurement via AFM colloidal probe technique. The main goal of this numerical analysis was to investigate the effect of surface roughness as a source of discrepancy between the experimentally observed interactions and the interactions predicted by DLVO theory (over a flat surface). Incorporating the numerical calculations to include random roughness of the surface, could substantially decrease the observed discrepancy.

In a very recent study done by Huang *et al*. [Huang et al., 2010], surface element integration was employed to numerically determine the potential interactions between spherical particles and nanopatterned surfaces based on extended DLVO theory. The roughness features were modeled as hemispherical pumps (protrusions), and hemispherical holes (depressions). In this study, it was mainly concluded that as the size of the spherical particle increases with respect to the constant size of the asperities, the interaction energy decreases as a result of existing roughness. Also, it was shown that by decreasing the density of the asperities, the influence of the surface roughness is less pronounced. The range of the electrostatic interaction was reduced up to higher

extents than the van der Waals interaction, meaning that the morphological elements make the surface more attractive. These conclusions were true for both protruding and depressed elements. Moreover, by including acid-base interactions into the analysis, they have observed that the effect of surface morphology is as important as the surface chemistry in determining the total interfacial energies.

2.5 Summary

In this chapter, the DLVO theory and its energy components were introduced. Additionally, different existing mathematical techniques for calculating these potential energies for two-body interaction scenarios were presented and their limitations were discussed. Surface element integration (SEI) technique was introduced, and based on the shortcomings of the other methods, it was discussed that this technique provides the most suitable mathematical platform for theoretical calculations if the interaction between complicated geometry bodies is required. SEI can be employed for both the van der Waals and electrostatic interaction energy.

In addition, a literature survey was also provided, in which some other previous studies were presented. These studies have reported the profound influence of morphological properties of the surface on interfacial or suspension forces. In this regard, some studies acknowledged a considerable discrepancy between their experimental observations in different colloidal or biological phenomena, and the predicted theoretical values by calculation of the colloidal interactions based on the classical DLVO theory. In summary, the rate of adhesion or particle deposition was reported to be higher on rough surfaces and the overall interaction is less repulsive than the forces over smooth surfaces. It was shown that some researchers have attempted to ascribe such an inconsistency to the existence of other non-DLVO energies in real colloidal systems. On the other hand, other studies attempted to investigate the effect of surface roughness as a reason of the divergence between the experiments

and theory. In experimental attempts, AFM colloidal probe technique was used to investigate either the rate of deposition by examining the surface topography of a surface after fouling or sedimentation process, or to measure the interaction force between the AFM probe and the surface. These studies could successfully address that the surface roughness considerably affects the interfacial colloidal forces.

Following to the experimental efforts, earlier theoretical studies on the subject of surface roughness and colloidal interfacial energies were discussed. According to the current knowledge, most of these investigations have been conducted by implementing numerical calculations for simulating the colloidal systems and the corresponding interfacial energies. On the other hand, a lack of analytical study on energy characterizations based on the influence of surface roughness was evident in this survey. Moreover, although the previous numerical studies could clearly prove that the surface roughnesses can reasonably affect the colloidal energies, there are still some ambiguities about the mechanism of the particle-surface interactions. For instance, the subject of minimum separation distance between an approaching particle and the model rough surface is not thoroughly discussed yet. This subject seriously broadens the modeling processes and force characterizations, due to the fact that every parametric studies on colloidal interactions (such as the effect of asperity density or size), must be followed by considering the local minimum separation distance. Conducting such an analysis, the variation of the energy as a function of lateral position of the probe over the surface can also be derived.

Therefore, in the present study, according to the above literature survey, it is initially attempted to experimentally demonstrate the effect of surface roughness. To this end, AFM is used for force measurement, when the AFM original sharp tip was used instead of attaching a colloidal particle to the probe (colloidal probe technique). This is to determine whether AFM is able to detect very small forces and the fluctuations in the forces as a result of nano-scale variation in surface heterogeneities or not. This was not possible in colloidal probe technique. Afterward, as the main goal, it is aimed to

characterize the influence of surface roughness by developing a set of analytical relations for explaining the attenuation in energy observed as a result of surface roughness. In these derivations, SEI technique was employed to characterize the reduction of energy between a flat and rough surface by modeling different shapes of the asperities. Then, by repositioning a model spherical particle over a rough surface consisting the hemispherical protrusions, the distribution of energy is investigated numerically, when the subject of minimum separation distance comes into consideration. In excess to this simulation, to improve the accuracy in the probe modeling, the inaccurate hemispherical probe model is replaced with more precise shapes of an AFM probe. These shapes, however, are only used to investigate their difference with previously used hemispherical probe. In this regard, it is numerically attempted to observe that how the DLVO interaction energy between such probe models and a flat surface varies by changing the geometrical parameters of the simulated probe. In these simulations, the surface roughness analysis is ignored.

Chapter 3

Theoretical Modeling of DLVO Interaction Energy for Rough Surfaces

3.1 Introduction

In this chapter, the mathematical methodology and numerical simulations developed in this study will be introduced. These simulations are implemented to assess the colloidal interaction energy between a model AFM probe and a model physically heterogenous surface as a function of the separation distance between them. These analyses will be used to investigate how the range of these energies are influenced by the roughness of the surface. The calculations for the interaction energy between the surface and the probe are developed based on the DLVO (Derjaguin-Landau-Verwey-Overbeek) theory [Derjaguin and Landau, 1941, Verwey and Overbeek, 1948]. Assuming the components of the DLVO energy are additive, the total interaction energy between the probe and the rough surface can be represented as the summation of the attractive van der Waals and the repulsive electrostatic double layer energies. The approaching probe has been assigned different geometries, namely, hemispherical, conical and pyramidal shapes in this study. In this way, a precise understanding in terms of the correlation between the probe geometrical parameters and the corresponding interaction energy is achievable. Physical heterogeneities of the surface are also modeled based on a set of different geo-

metrical shapes distributed on the surface in a specific configuration. In section 3.2, the computational generations of rough surfaces are explained. Similarly, generation of the different interacting probe geometries are addressed. In section 3.3, the DLVO interaction energy components are calculated for a variety of rough surfaces interacting with a flat plate (which can be considered as an artificially enlarged probe with infinite radius of curvature) to depict the influence of the surface roughness on these energies. Subsequently, a numerical method based on surface element integration (SEI) approach [Bhattacharjee and Elimelech, 1997] is described to assess the interaction between a probe and the model substrate. Finally, the numerical models are validated against the analytical calculations derived for simplified cases using existing analytical expressions based on Hamaker approach [Hamaker, 1937] and Derjaguin approximation [Derjaguin, 1934, White, 1983]. As a result, the accuracy of the numerical approach can be assessed in terms of the DLVO components.

3.2 Geometrical Modeling of Uniformly Patterned Heterogeneous Surfaces and Approaching Probes

3.2.1 Rough Surface Modeling

This subsection introduces the method implemented to generate a rough surface. Other studies have tried to investigate the influence of the surface physical heterogeneities on the DLVO interaction energy by defining a set of randomly distributed asperities on the surface [Hoek et al., 2003, Cooper et al., 2001, Eichenlaub et al., 2006]. In this study, however, the rough surfaces are defined based on uniformly patterned asperities of hemispherical, conical, and cylindrical shapes. By positioning the asperities in a uniformly distributed pattern, one is able to analyze the relation between the lateral position of the probe over the surface, and the interaction energy as a result of the local separation distance. The minimum separation distance is imposed by the relative lateral positions of the probe and the surface. In the current study,

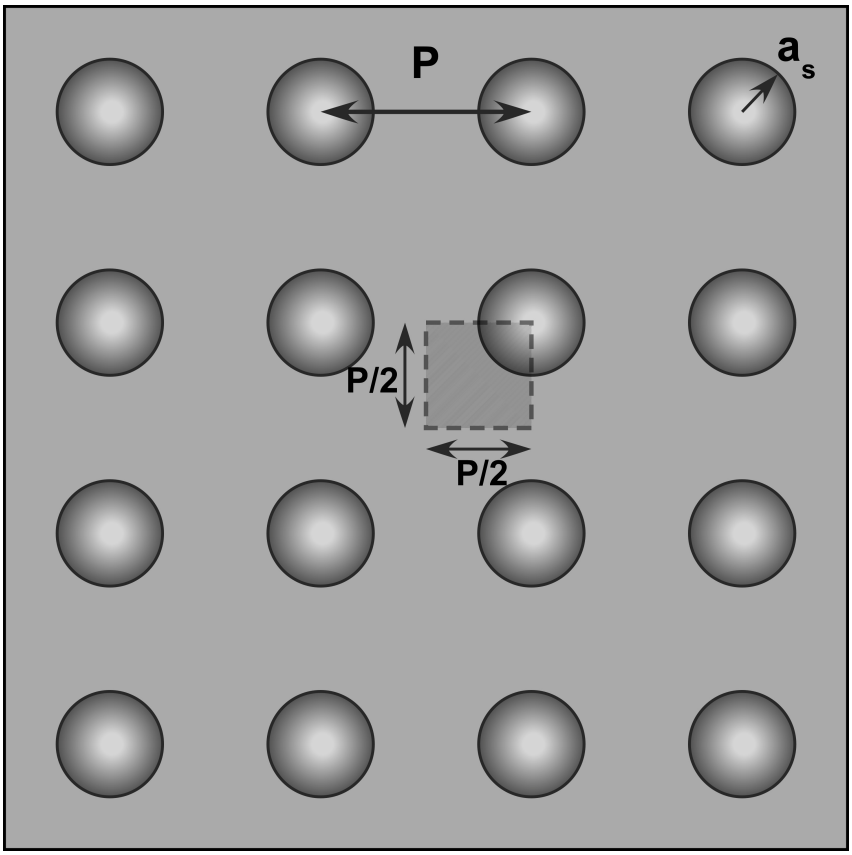

Figure 3.1: 2D schematic representation of a uniformly patterned rough surface, consisting hemispherical asperities. The pitch distance P is defined as the center to center distance between two adjacent asperities. The unit cell is also defined as a $P/2$ by $P/2$ square.

the asperities are arranged on a square lattice; However, one may also apply a hexagonal lattice. This unit cell is illustrated in Figure 3.1. As shown in this figure, the pitch distance P is defined as the distance between the centers of two adjacent asperities. The minimum pitch distance is $P = 2a_s$, where a_s is the asperity base radius, to prevent the overlap of adjacent asperities.

Figure 3.2a depicts a 3D schematic of a numerically generated rough surface with uniformly distributed hemispherical bumps. The hemispherical asperities on the surface are numerically generated using the governing equation of a sphere in Cartesian coordinate system,

$$Z = Z_0 - \left[r^2 - (X - X_0)^2 - (Y - Y_0)^2\right]^{\frac{1}{2}} \tag{3.1}$$

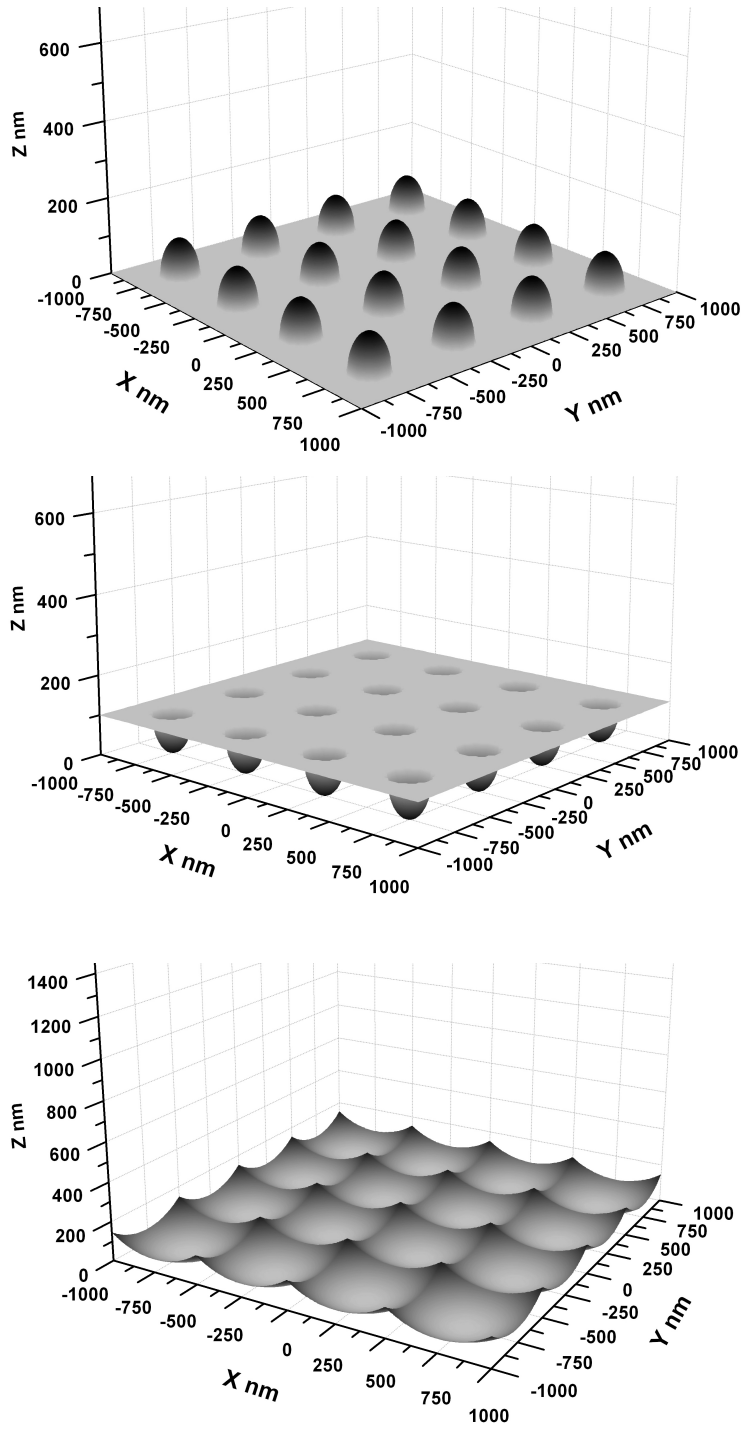

Figure 3.2: 3D schematics of a numerically generated rough surface consisting of hemispherical **(a)** protrusions, and **(b)** depressions. The radius of asperities are 100 nm, and the pitch is 500 nm. In part **(c)**, the asperities are in depression form, but the asperity size, and the pitch distance are both set to 500 nm. Therefore, the hemispherical depressions interfere with each other and result in a pointy head shape roughness. In all cases, the projected area of the surface is 2000 nm $\times$ 2000 nm.

where (X_0, Y_0, Z_0) represent the coordinates of the asperity origin, and r is the asperity radius.

Likewise, the conical shape roughness can be produced mathematically using the following relation:

$$Z = Z_0 + \sqrt{\frac{X^2 + Y^2}{(r/h)^2}} \tag{3.2}$$

where r and h represent the cone base radius and its vertical height respectively.

The computation associated with generation of the rough surfaces requires the size of the surface, pitch distance, and the asperity size as input parameters. If the asperities are in depression form as in Figure 3.2 b, by decreasing the pitch to values less than $2a_s$, one will be able to produce a rough surface with pointed heterogeneities, having different amplitudes as illustrated in Figure 3.2 c.

3.2.2 Approaching Probe Modeling

In this subsection, the geometrical modeling and parametric equations of the approaching probe are described. The actual geometry of an atomic force microscopy (AFM) probe is pyramidal as shown in Figure 4.1. This figure is a scanning electron microscopy (SEM) image of a Veeco DNP-S20 silicon nitride (Si_3N_4) AFM tip. This type of probe geometry is widely used in contact mode scanning with AFM. The base of the probe is a 4 μm $\times$ 4 μm square, where its vertical height is almost 6 μm long, and the wall angle is roughly calculated as 70 degrees. At the top edge of the probe, there is a spherical cap as shown in the SEM image in Figure 4.1b, where its radius has been approximately measured with SEM dimension measurement tool in the range of 18 to 20 nm.

Apart from the real structure of the DNP-S20 probe, which comprises both the pyramidal and hemispherical sections, the hemispherical portion of the probe needs to be simulated individually. Incorporating the modeling for this segment of the probe, not only simplifies the calculations, but also by increas-

(a)

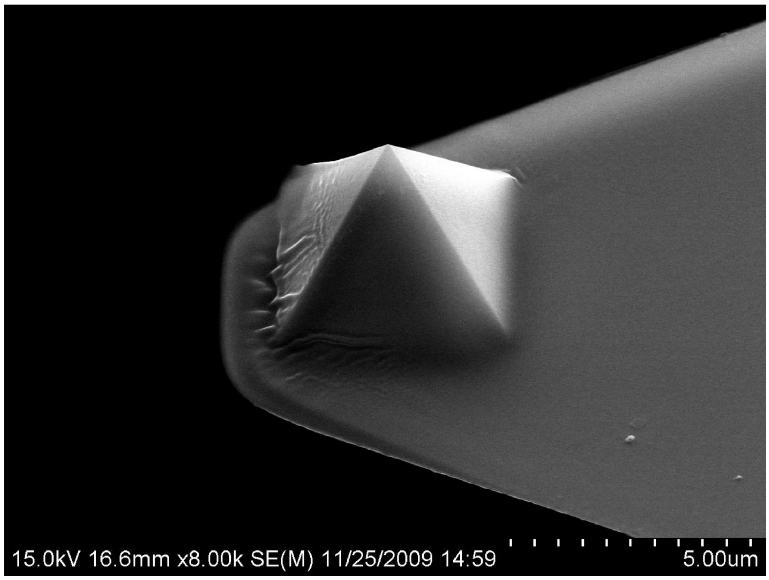

(b)

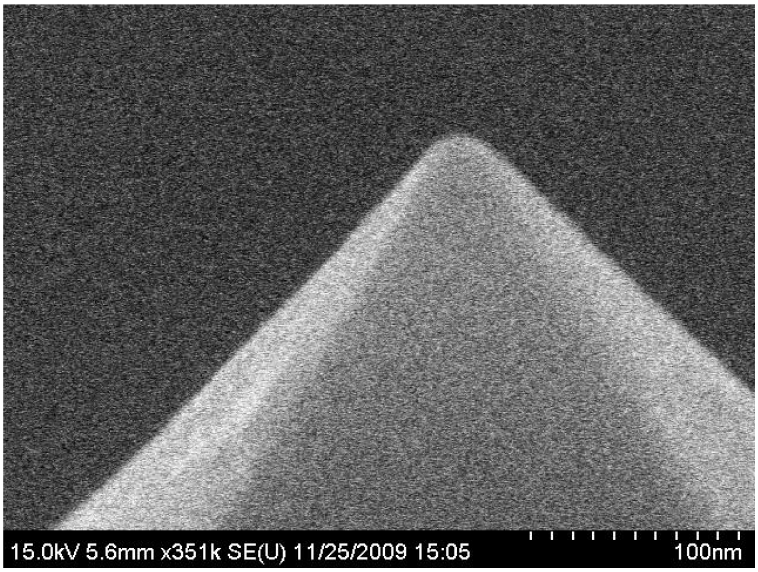

Figure 3.3: SEM images of AFM silicon nitride (Si_3N_4) DNP tip. **(a)** 45° titled zoom-out image of the pyramidal tip attached to the cantilever. **(b)** 0° titled zoom-in image of the same tip. The total height of the probe is roughly 6 μm, while the base is a 4 μm × 4 μm square. The spherical tip radius is roughly between 18 to 20 nm. The images were taken by Daniel Salamon, the technical officer, with a Hitachi SEM in the National Institute for Nanotechnology (NINT).

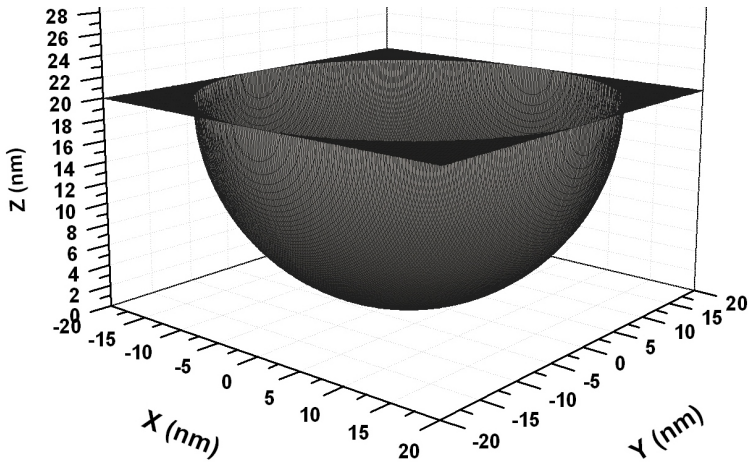

Figure 3.4: 3D schematic of a model hemispherical probe. The radius of the probe is 20 nm and its origin is located at (0, 0, 20) in X, Y, and Z Cartesian coordinates.

ing the size of the model hemispherical probe, the colloidal probe technique (as described in chapter 2) can be simulated. Moreover, varying the size of the model hemispherical probe allows one to investigate the correlation between the minimum possible separation distance between the approaching probe and the rough substrate and the corresponding interaction energy. The minimum separation distance mentioned above is not unique in all experiments, depending on different surface and probe geometrical characteristics, and the lateral position of the probe with respect to the surface.

Figure 3.4 illustrates the 3D schematic of a hemispherical probe with the radius of 20 nm, generated in the same way as in the hemispherical asperities (Figure 3.2), using Eqn. (3.1), where the (X_0, Y_0, Z_0) and r are set to (0, 0, 20 nm) and 20 nm, respectively, for the schematic shown in Figure 3.4. The probe is faced downward, meaning that the interacting model surface will be on the $Z = 0$ plane, similar to the actual configuration of the probe and the substrate in an AFM force measurement. As explained earlier, the DNP-S20 probe consists a hemispherical section attached to a larger truncated pyramid. In other probes, this pyramidal section could be modeled as a conical shape. In this way, the short-range colloidal interactions considered in the

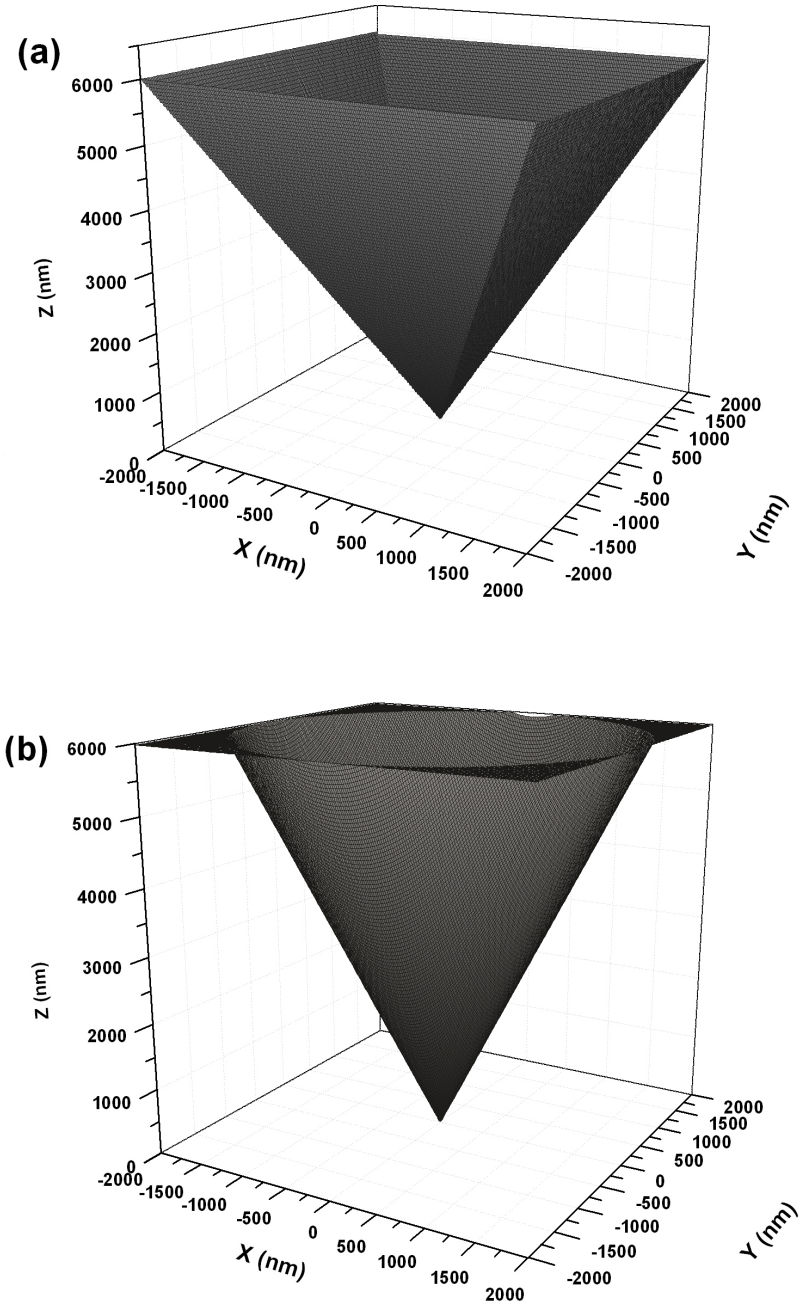

Figure 3.5: 3D schematic of a mathematically modeled **(a)** pyramidal, and **(b)** a conical shape probe. The height in both cases is 6 μm, and the base is a 4 $\mu m \times 4$ μm square. The wall angle is set to 70 degrees The peak point of the probe is located at(2000, 2000, 0) μm in X, Y, and Z Cartesian coordinates (The associated codes for generation of these structures can be found in the appendix section).

AFM experimental force measurements using a sharp silicon nitride tip as shown in Figure 4.1 will be analyzed in the numerical simulations. Moreover, by increasing or decreasing the size of the attached hemispherical tip, the effect of the tip convolution observed in experimental force remeasurements can be also addressed.

Figure 3.5 depicts the mathematically generated models of a pyramidal and conical shape probe with a 4 μm $\times$ 4 μm square base, and 6μm height. The wall angle θ is set to 70 degrees in both cases. The structures shown in this figure do not include the hemispherical section modeled in Figure 3.4. In the present study, to generate a model which accurately represents the AFM probe, two different approaches are proposed. The model probe is assembled by attaching the truncated pyramidal ($e.g.$, for Si_3N_4 probe) or conical structure to a spherical cap. In the first approach, the tip is a hemisphere, and is attached to the truncated shape, such that the total height of the structure (H) is equivalent to the desired height of the simulated probe ($e.g.$, 6μm). In other words, in Figure 3.6a, $H = h + R$, where h is the height of the truncated shape, and R is the hemispherical cap radius. In this approach, attaching a hemispherical shape to the bottom edge of the truncated pyramid/cone will result in an edge angle at the junction of the two geometries on the probe wall. Considering the difference between the magnitude of $H = 6\mu m$, and $R = 20nm$, this approach still provides good estimation in modeling the AFM probe. However, to increase the level of precision in the calculation of the DLVO interaction energies for larger hemispherical tips, a more realistic model is developed, in which only a portion of sphere is used which does not cause any edge (wall angle) when it attaches to the truncated geometry.

The 2D schematics of the modeling approaches explained above are illustrated in Figure 3.6. The sketches shown here improve upon both the conical and pyramidal probes modeled in Figure 3.5. The actual height of the probe generated based on the second approach can be calculated as below:

$$L^{'} = 2R\sin\theta \tag{3.3}$$

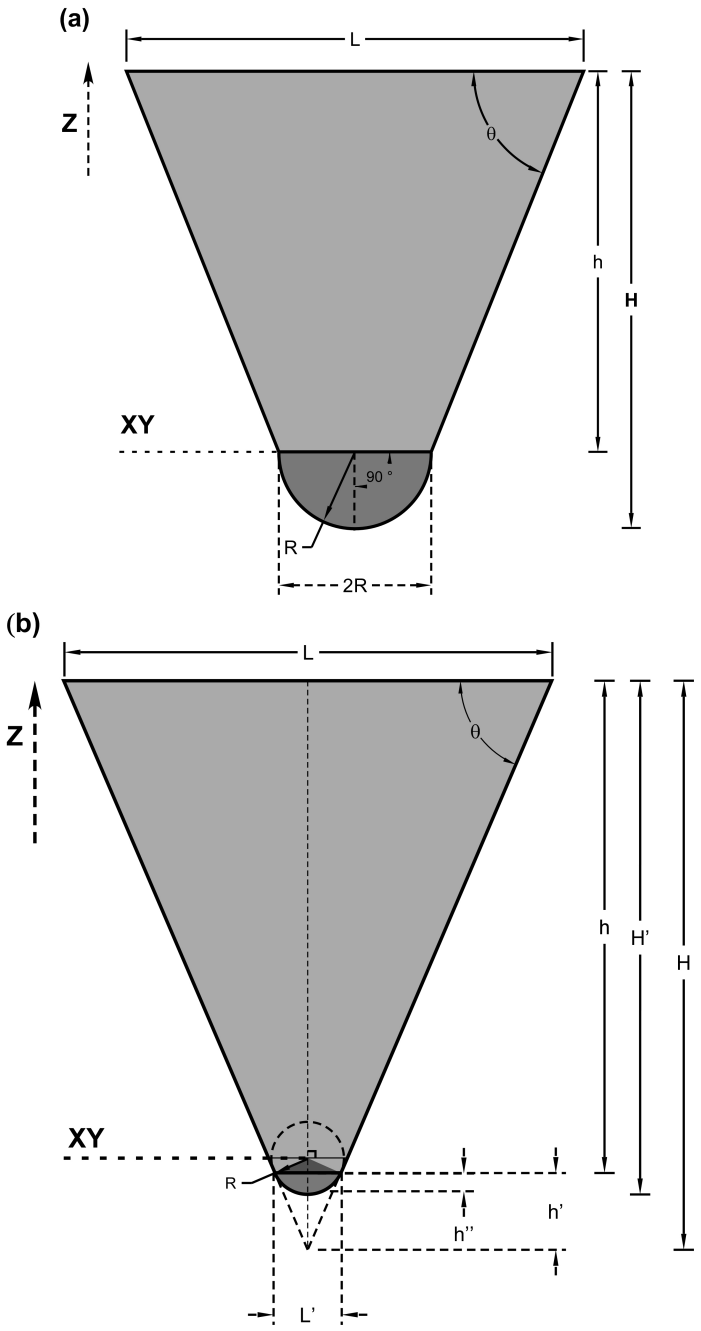

Figure 3.6: 2D sketches of the two mathematical models used to create the interacting probe. The light section represents the truncated pyramidal or conical structure, while the dark region represents a tip attached to the upper part: **(a)** The tip is a full hemisphere with radius R , which causes an edge angle at the joint surface between the two sections. **(b)** The tip is conceived as only a portion of the sphere in part (a), such that in the attachment it avoids any edge angle on the wall.

$$h^{'} = \frac{2HR\sin\theta}{a} \tag{3.4}$$

$$h^{''} = R\left(1-\cos\theta\right) \tag{3.5}$$

$$Height = H^{'} = H - h^{'} + h^{''} = H - \frac{2HR\sin\theta}{a} + R\left(1-\cos\theta\right) \tag{3.6}$$

It is obvious that $h = H - h^{'}$, which is the height of the truncated pyramidal/conical shape in Figure 3.6b, is larger than its value h in Figure 3.6a.

It must be noted here that the calculations associated to the second approach (Figure 3.6b) require the angle θ, the tip radius R, and the height H as inputs, where H is the height of a complete pyramid or cone. According to Eqn. (3.6), if the inputs have the values of $H = 6\mu m$, and $\theta = 70^0$, the resulting height will be $H^{'} = 5962nm$. Considering the magnitudes already mentioned for the actual AFM probe, if the input H is selected as 6040 nm with $\theta = 70°$, or $H = 6030nm$ with $\theta = 69°$, the output height, $H^{'}$, (Figure 3.6b) will exactly meet its required magnitude of $6\mu m$.

3.3 Analytical Calculation of the DLVO Interaction Energy between a Model Rough Surface and an Infinite Flat Plate

Many other studies have attempted to characterize DLVO or extended DLVO energies for two interacting bodies to investigate the effect of surface roughness on the interaction energy [Hoek et al., 2003, Huang et al., 2010, Suresh and Walz, 1996, Martines et al., 2008]. In this section, the van der Waals (VDW) and the electrostatic double layer (EDL) interaction energies per unit area are analytically calculated between a nanostructured rough substrate and an infinite smooth flat plate. Different asperities in the form of protrusions or depressions were mathematically generated on a square lattice to represent the rough surface. The size of the asperities and the pitch (separation)

between their centers were varied. These derivations will help to assess the coupling between the range of the interactions and the roughness features of the substrate by comparing the ratios of the rough surface to smooth surface interaction energies per unit area. Conventionally, the VDW interaction is calculated employing Hamaker's technique, which is an integration of the attractive Lennard-Jones interaction over the volumes of the interacting bodies [Hamaker, 1937]. For arbitrary shapes, analytical evaluation of integrals in Hamaker approach becomes cumbersome. The EDL interaction is evaluated by solving the Poisson-Boltzmann (PB) equation. Solving the PB equation by employing numerical schemes, such as, boundary element, finite difference, or finite element analysis, pose substantial computational burden in the case of arbitrary shapes.

The Derjaguin approximation (DA) can be applied as an alternative for calculation of both the VDW and EDL interaction [Derjaguin, 1934, White, 1983]. The DA scales the interaction energy per unit area of two infinite flat plates to the corresponding energy between two curved bodies. However, the approximation is valid only for cases where the separation distance between the interacting bodies are much smaller than the principal radii of curvature of the surfaces. Alternatively, assuming that roughness features are arranged in a periodic order, the interaction energy per unit area between the two surfaces can be analytically derived using surface element integration technique (SEI). Here, a new set of analytical expressions have been derived via (SEI), which accounts for the influence of roughness features on DLVO interaction potentials, by comparing the ratios of nanopatterned rough surface potentials to the corresponding flat plate potentials. Accordingly, without invoking any numerical computations, the effect of surface roughness on DLVO interaction energy can eventually be illustrated.

The DLVO theory expresses the overall interaction energy between two colloidal entities as the sum of attractive van der Waals and repulsive electrostatic double layer interactions according to:

$$U_{total} = U_{VDW} + U_{EDL} \tag{3.7}$$

Here, the non-retarded van der Waals interaction per unit area between two infinite flat plates separated by a distance h is used:

$$U_{VDW}(h) = -\frac{A_H}{12\pi h^2} \tag{3.8}$$

where A_H is the Hamaker constant for the two materials interacting through the media (assumed water herein). To simplify the analytical calculations, the electrostatic double layer interaction, defined from the linear superposition approximation (LSA) expression [Gregory, 1975] for two infinite flat plates at constant potential is expressed as:

$$U_{LSA}(h) = 32\epsilon_0\epsilon_r\kappa\gamma_1\gamma_2\left(\frac{k_BT}{\nu e}\right)^2\exp(-\kappa h) \tag{3.9}$$

$$\gamma_i = tanh\left(\frac{\nu e\psi_i}{4k_BT}\right)^2 \tag{3.10}$$

where $\epsilon_0 = 8.854 \times 10^{-12}$ $\text{CV}^{-1}\text{m}^{-1}$ is the vacuum permittivity, $\epsilon_r = 78.5$ is the dielectric constant of water, κ is the inverse Debye screening length, ν is the ionic valence of the symmetric electrolyte equal to 1, and ψ_i is the surface potential of each interacting plate.

3.3.1 Hemispherical Asperities

Protrusions:

To develop the analytical expressions for the interaction energy per unit area between a smooth surface and a rough surface consisting of hemispherical protrusions, according to the SEI approach, the interaction energies per unit area between two infinite flat plates (*i.e.*, Eqns. 3.8 and 3.9) have to be integrated over the surface of one unit square cell, with asperities as depicted in Fig. 3.7a. The corresponding van der Waals interaction energy is derived as:

$$E_r = -\frac{A_H\left(P^2 - \pi a_s^2\right)}{12\pi\left(h_0 + a_s\right)^2} + 2\pi\int_0^{a_s} rdr\left[\frac{-A_H}{12\pi h^2}\right] \tag{3.11}$$

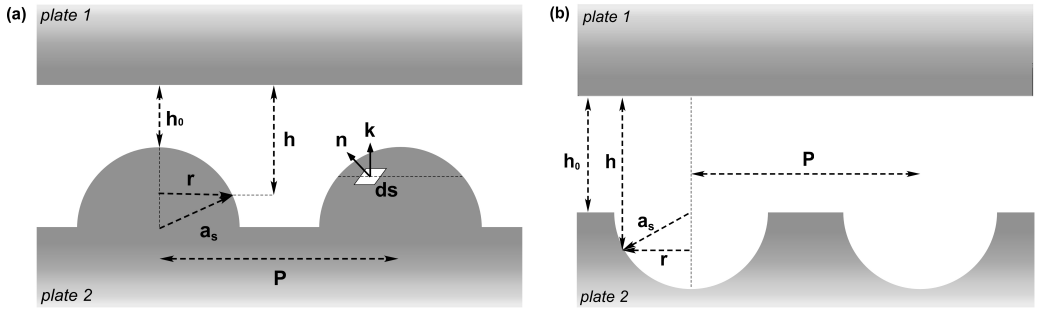

Figure 3.7: Geometrical schematic of roughness elements for hemispherical **(a)** protrusions, and **(b)** depressions.

where according to Figure 3.7a, h, which is the separation between the integrating element and the interacting flat surface, can be defined as:

$$h = h_0 + a_s - \sqrt{a_s^2 - r^2} \tag{3.12}$$

substituting Eqn. (3.12) into Eqn. (3.11), one can continue as:

$$E_r = -\frac{A_H\left(P^2 - \pi a_s^2\right)}{12\pi\left(h_0 + a_s\right)^2} + \frac{A_H}{6}\left[\ln\left(1 + \frac{a_s}{h_0}\right) - \frac{a_s}{h_0}\right] \tag{3.13}$$

Defining the unit area a P by P square, the VDW interaction energy per unit area for a rough surface consisting of hemispherical protrusions is:

$$\begin{aligned} E_r/A &= \frac{E_r}{P^2} = -\frac{A_H}{12\pi}\frac{\left[1 - \pi\left(a_s/P\right)^2\right]}{\left(h_0 + a_s\right)^2} + \frac{A_H}{6P^2}\left[\ln\left(1 + \frac{a_s}{h_0}\right) - \frac{a_s}{h_0}\right] \\ &= -\frac{A_H}{6}\left[\frac{1 - \pi\left(a_s/P\right)^2}{2\pi\left(h_0 + a_s\right)^2} + \frac{a_s}{h_0 P^2} - \frac{\ln\left(1 + \frac{a_s}{h_0}\right)}{P^2}\right] \end{aligned} \tag{3.14}$$

Having the VDW interaction energy per unit area for two smooth flat plates from Eqn. (3.8), the ratio E_r/E_s is found as:

$$\frac{E_r}{E_s} = \frac{\left[1 - \pi\left(a_s/P\right)^2\right] + 2\pi\left(1 + \frac{a_s}{h_0}\right)^2\left(\frac{h_0}{P}\right)^2\left[\frac{a_s}{h_0} - \ln\left(1 + \frac{a_s}{h_0}\right)\right]}{\left(1 + \frac{a}{h_0}\right)^2} \tag{3.15}$$

Using Eqns. (3.9) and (3.10), the EDL interaction energy can similarly be evaluated as:

$$\begin{aligned} E_r &= \left(P^2 - \pi a_s^2\right) A_c \exp\left[-\kappa\left(h_0 + a_s\right)\right] + 2\pi \int_0^{a_s} r dr A_c \exp\left(-\kappa h\right) \\ &= \left(P^2 - \pi a_s^2\right) A_c \exp\left[-\kappa\left(h_0 + a_s\right)\right] \\ &+ \frac{2\pi A_c}{\kappa^2}\left[\exp\left(-\kappa\left(h_0 + a_s\right)\right) + \left(\kappa a_s - 1\right)\exp\left(-\kappa h_0\right)\right] \end{aligned} \tag{3.16}$$

where h is given by Eqn. (3.12), and A_c is a constant:

$$A_c = 32\epsilon_0\epsilon_r\kappa\gamma_1\gamma_2\left(\frac{k_B T}{\nu e}\right)^2 \tag{3.17}$$

Accordingly, the ratio of the EDL interaction energy per unit area for a rough surface interacting with a smooth flat plate to the corresponding interaction between two infinite flat surface will be:

$$\frac{E_r}{E_s} = \exp\left(-\kappa a_s\right)\left[1 - \pi\left(a_s/P\right)^2\right] + \frac{2\pi}{\left(\kappa P\right)^2} + \frac{2\pi\left(\kappa a_s - 1\right)}{\left(\kappa P\right)^2} \tag{3.18}$$

Interestingly, the energy ratio in Eqn. (3.18) is independent of the separation distance h_0.

Depressions:

Figure. 3.7b depicts the geometrical parameters used to evaluate the interaction energy per unit area for a rough surface consisting of identical hemispherical depressions (plate 2) interacting with an infinite flat surface (plate 1). In the following, the DLVO energy components are derived individually. Defining $h = h_0 + \sqrt{a_s^2 - r^2}$, the VDW interaction can be calculated as:

$$\begin{aligned} E_r &= -\frac{A_H}{12\pi}\frac{\left(P^2 - \pi a_s^2\right)}{h_0^2} - \left[\frac{-A_H}{6}\int_a^0 \frac{r dr}{\left(h_0 + \sqrt{a_s^2 - r^2}\right)^2}\right] \\ &= -\frac{A_H}{12\pi}\frac{\left(P^2 - \pi a_s^2\right)}{h_0^2} + \frac{A_H}{6}\left[\frac{1}{1 + h_0} + \ln\frac{1}{1 + 1/h_0}\right] \end{aligned} \tag{3.19}$$

Having E_s per unit area defined in Eqn. (3.8), the ratio $\frac{E_r}{E_s}$ is found as:

$$\frac{E_r}{E_s} = 1 - \pi \left(a_s/P\right)^2 - \frac{2\pi h_0^2}{P^2}\left[\frac{a_s}{a_s + h_0} + \ln\frac{h_0}{h_0 + a_s}\right] \tag{3.20}$$

Based on the Eqns. (3.9, 3.10, and 3.17), the electrostatic part of the DLVO interaction energy for hemispherical depressions is evaluated as following.

$$\begin{aligned} E_r &= \left(P^2 - \pi a_s^2\right) A_c \exp\left(-\kappa h_0\right) - 2\pi \int_{a_s}^{0} r dr A_c \exp(-\kappa h) \\ &= \left(P^2 - \pi a_s^2\right) A_c \exp\left(-\kappa h_0\right) + 2\pi A_c \int_{0}^{a_s} \exp\left[-\kappa\left(h_0 + \sqrt{a_s^2 - r^2}\right)\right] r dr \\ &= \left(P^2 - \pi a_s^2\right) A_c \exp\left(-\kappa h_0\right) + \frac{2\pi A_c}{\kappa^2}\left[\exp(-\kappa h_0) - (\kappa a_s + 1)\exp(-\kappa(a_s + h_0))\right] \end{aligned} \tag{3.21}$$

Finally, the ratio E_r/E_s for a surface patterned with hemispherical depressions is:

$$\frac{E_r}{E_s} = 1 - \pi(a_s/P)^2 + \frac{2\pi}{(\kappa P)^2}\left[1 - (\kappa a_s + 1)(\exp(-\kappa a))\right] \tag{3.22}$$

Similar to the E_r/E_s, expression of EDL interaction energy for protrusions, the energy ratio in Eqn. (3.22) is independent of the scaled separation h_0.

3.3.2 Conical Asperities

Protrusions:

In this subsection, the DLVO interaction energy components are analytically formulated individually for a scenario when an infinite flat plate is interacting with a heterogenous surface, for which the roughness elements are modeled with either protruding, or depressed conical shape asperities. Figure 3.8, clearly depicts the geometrical parameters used in the following analytical expressions. It is pertinent to highlight that the size a_s in Figure 3.8 is defined as the cone base radius, rather than the hemispherical radius previously used in Figures. 3.7. Here, h is defined as:

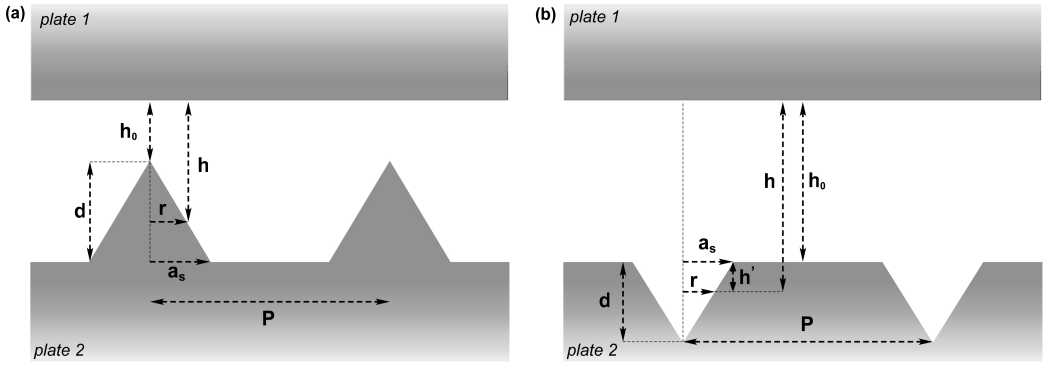

Figure 3.8: Geometrical schematic of roughness elements for conical **(a)** protrusions, and **(b)** depressions.

$$E_r = -\frac{A_H\left(P^2-\pi a_s^2\right)}{12\pi\left(h_0+d\right)^2} + 2\pi\int_0^{a_s} rdr\left[\frac{-A_H}{12\pi h^2}\right] \tag{3.23}$$

$$h = \frac{rd}{a_s} + h_0 \tag{3.24}$$

then the corresponding VDW interaction energy between the rough and smooth surfaces for a P by P area can be evaluated as:

$$\begin{aligned} E_r &= -\frac{A_H}{12\pi}\frac{\left(P^2-\pi a^2\right)}{\left(h_0+d\right)^2} - \frac{A_H}{12\pi}\int_0^{a_s}\frac{2\pi r dr}{\left(h_0+\frac{rd}{a_s}\right)^2} \\ &= -\frac{A_H}{12\pi}\frac{\left(P^2-\pi a^2\right)}{\left(h_0+d\right)^2} + \frac{A_H}{6}\left(\frac{a_s}{d}\right)^2\left[\frac{d}{h_0+d}+\ln\frac{h_0}{h_0+d}\right] \end{aligned} \tag{3.25}$$

Dividing Eqn. (3.25) by Eqn. (3.8), one can obtain:

$$\begin{aligned} \frac{E_r}{E_s} &= \frac{\left(1-\pi\left(a_s/P\right)^2\right)}{\left(1+d/h_0\right)^2} \\ &\quad -2\pi\frac{h_0^2}{P^2}\left(a_s/d\right)^2\left[\frac{d/a_s}{h_0/a_s+d/a_s}+\ln\left(\frac{h_0/a_s}{h_0/a_s+d/a_s}\right)\right] \end{aligned} \tag{3.26}$$

The electrostatic interaction energy for this surface is evaluated as follows:

$$
\begin{aligned}
E_r &= E_{r1} + E_{r2} \qquad (3.27)\\
&= \left(P^2 - \pi a_s^2\right) A_c \exp\left[-\kappa\left(h_0 + d\right)\right] + 2\pi \int_0^{a_s} r dr A_c \exp\left(-\kappa h\right)\\
&= E_{r1} + 2\pi \int_0^{a_s} r dr A_c \exp\left(-\kappa(\frac{rd}{a_s} + h_0)\right)\\
&= E_{r1} - \frac{2\pi A_c a_s}{\exp(\kappa h_0)(d\kappa)^2}\left[\exp(-\kappa d)(1+\kappa a) - 1\right]
\end{aligned}
$$

Therefore, the E_r/E_s ratio is:

$$
\frac{E_r}{E_s} = \frac{(P^2 - \pi a_s^2)\exp(-\kappa d)}{P^2} + \frac{2\pi a_s^2}{P^2(\kappa d)^2}\left[1 - \exp(-\kappa d)(1+\kappa d)\right] \qquad (3.28)
$$

Depressions:

For conical depressions shown in Figure 3.8b, where $h = h_0 + d - rd/a_s$ one may obtain the following E_r/E_s relation for the van der Waals interaction:

$$
\frac{E_r}{E_s} = 1 - \frac{\pi a_s^2}{P^2} + 2\pi(\frac{h_0 a_s}{Pd})^2[\frac{d+h_0}{h_0} + \ln(\frac{h_0}{d+h_0}) - 1] \qquad (3.29)
$$

And for electrostatic interaction the E_r/E_s ratio is as follows:

$$
\frac{E_r}{E_s} = 1 - \frac{\pi a_s^2}{P^2} + \frac{2\pi\exp(-\kappa d)a_s^2}{P^2}\left[\frac{\exp(\kappa d)(\kappa d - 1) + 1}{(\kappa d)^2}\right] \qquad (3.30)
$$

In Eqns. (3.26, 3.28, 3.29, and 3.30) d stands for the asperity height as shown in Figure 3.8.

3.3.3 Cylindrical Asperities

Protrusions:

In this subsection, the roughness elements are in cylindrical form. Similar analyses as in the last two subsections have been performed for the DLVO interaction energy per unit area:

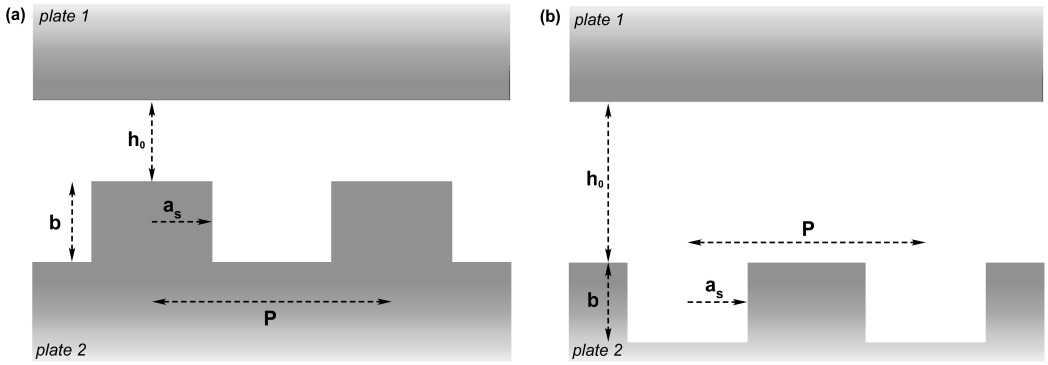

Figure 3.9: Geometrical schematic of roughness elements for cylindrical **(a)** protrusions, and **(b)** depressions.

$$E_r = -\frac{A_H}{12}\left[\frac{(P^2 - \pi a_s^2)}{(b+h_0)^2 + \frac{\pi a_s^2}{h_0^2}}\right] \tag{3.31}$$

$$\frac{E_r}{E_s} = \frac{h_0^2}{(h_0+b)^2}\left[1 + \pi\left(a_s/P\right)^2\left(b/h_0\right)\left(2 + \left(b/h_0\right)\right)\right] \tag{3.32}$$

For the electrostatic interaction energy:

$$E_r = (P^2 - \pi a_s^2)A_c \exp\left[-\kappa(h_0+b)\right] + \pi a_s^2 A_c \exp\left[-\kappa h_0\right] \tag{3.33}$$

Hence the E_r/E_s ratio is:

$$\frac{E_r}{E_s} = \frac{(P^2 - \pi a_s^2)\exp(-\kappa b)}{P^2} + \frac{\pi a_s^2}{P^2} \tag{3.34}$$

Depressions:

For cylindrical depressions as in Figure 3.9b, the following equations have been derived for van der Waals and electrostatic interaction energies.

$$\frac{E_r}{E_s} = 1 - \pi(\frac{a_s}{P})^2 + \pi(\frac{a_s h_0}{(h_0+b)P})^2 \tag{3.35}$$

$$\frac{E_r}{E_s} = 1 + \frac{\pi a_s^2(\exp(-\kappa b) - 1)}{P^2} \tag{3.36}$$

Table 3.1: Ratio of the van der Waals interaction energy per unit area derived for model rough surfaces interacting with a flat plate to the Hamaker's expression for interaction energy per unit area between two infinite flat plates. $a_s = 158$ nm, $h_0 = 1.58$ nm, $P = d = b = 316$ nm.

Asperity	E_r/E_s **Expression**	**Value**
Hemispherical protrusions	$\frac{\left[1-\pi(a_s/P)^2\right]+2\pi\left(1+\frac{a_s}{h_0}\right)^2\left(\frac{h_0}{P}\right)^2\left[\frac{a_s}{h_0}-\ln\left(1+\frac{a_s}{h_0}\right)\right]}{\left(1+\frac{a}{h_0}\right)^2}$	0.0150
Hemispherical depressions	$1-\pi\left(a_s/P\right)^2-\frac{2\pi h_0^2}{P^2}\left[\frac{a_s}{a_s+h_0}+\ln\frac{h_0}{h_0+a_s}\right]$	0.2144
Conical protrusions	$\frac{\left(1-\pi(a_s/P)^2\right)}{\left(1+d/h_0\right)^2}-2\pi\frac{h_0^2}{P^2}\left(a_s/d\right)^2\left[\frac{d/a_s}{h_0/a_s+d/a_s}+\ln\left(\frac{h_0/a_s}{h_0/a_s+d/a_s}\right)\right]$	1.74×10^{-4}
Conical depressions	$1-\frac{\pi a_s^2}{P^2}+2\pi(\frac{h_0a_s}{Pd})^2[\frac{d+h_0}{h_0}+\ln(\frac{h_0}{d+h_0})-1]$	0.2222
Cylindrical protrusions	$\frac{h_0^2}{(h_0+b)^2}\left[1+\pi\left(a_s/P\right)^2\left(b/h_0\right)\left(2+\left(b/h_0\right)\right)\right]$	0.7854
Cylindrical depressions	$1-\pi(\frac{a_s}{P})^2+\pi(\frac{a_sh_0}{(h_0+b)P})^2$	0.2146

Table 3.2: Ratio of the electrostatic interaction energy per unit area derived for model rough surfaces interacting with a flat plate to the LSA expression for interaction energy per unit area between two infinite flat plates. $a_s = b = d = 158$ nm, $P = 316$ nm, $\kappa a = \kappa b = \kappa d = 10$.

Asperity	E_r/E_s	**Value**
Hemispherical protrusions	$\exp(-\kappa a_s)\left[1-\pi\left(a_s/P\right)^2\right]+\frac{2\pi}{(\kappa P)^2}+\frac{2\pi(\kappa a_s-1)}{(\kappa P)^2}$	0.1571
Hemispherical depressions	$1-\pi(a_s/P)^2+\frac{2\pi}{(\kappa P)^2}\left[1-(\kappa a_s+1)(\exp(-\kappa a))\right]$	0.2303
Conical protrusions	$\frac{(P^2-\pi a_s^2)\exp(-\kappa d)}{P^2}+\frac{2\pi a_s^2}{P^2(\kappa d)^2}\left[1-\exp(-\kappa d)(1+\kappa d)\right]$	0.0157
Conical depressions	$1-\frac{\pi a_s^2}{P^2}+\frac{2\pi\exp(-\kappa d)a_s^2}{P^2}\left[\frac{\exp(\kappa d)(\kappa d-1)+1}{(\kappa d)^2}\right]$	0.3560
Cylindrical protrusions	$\frac{\left(P^2-\pi a_s^2\right)\exp(-\kappa b)}{P^2}+\frac{\pi a_s^2}{P^2}$	0.7854
Cylindrical depressions	$1+\frac{\pi a_s^2(\exp(-\kappa b)-1)}{P^2}$	0.2146

3.3.4 Summary

In the preceding subsections, the analytical expressions for van der Waals and electrostatic interaction energy per unit area have been derived for a model rough surface comprising hemispherical, conical, and cylindrical roughness elements interacting with a smooth flat surface. To summarize, these expressions have been collected in Tables 3.1, and 3.2.

Detailed analysis of the interactions for nanopatterned substrates based on the above analytical results will be discussed in chapter 5.

3.4 Numerical Calculation of the DLVO Interaction Energy between a Probe and Rough Surface and their Validation

3.4.1 Mathematical Model

In the previous section, the influence of surface roughness on the colloidal interactions was analyzed between a rough surface and a flat plate based on the SEI technique. The analytical derivations for interaction energies per unit area shown in Tables 3.1 and 3.2 can represent a large probe interacting with a rough surface with comparatively small heterogeneities, such that the probe radius is assumed to be infinite. One may employ the Derjaguin approximation [Derjaguin, 1934,White, 1983] (*cf.*, Chapter 2) to rescale these expressions for a curved body instead of an infinite flat plate, through an expression of the form

$$U(h) = \frac{2\pi}{\sqrt{\lambda_1 \lambda_2}} \int_h^\infty \frac{U(H)}{A} dH \tag{3.37}$$

where U is the interaction energy per unit area between the two curved bodies with the closest separation distance of h, and the parameter $\lambda_1\lambda_2$ is:

$$\lambda_1\lambda_2 = \left(\frac{1}{R_1} + \frac{1}{R_1'}\right)\left(\frac{1}{R_2} + \frac{1}{R_2'}\right) + \sin^2\varphi \left(\frac{1}{R_1} - \frac{1}{R_2}\right)\left(\frac{1}{R_1'} - \frac{1}{R_2'}\right) \tag{3.38}$$

Here, R_1 and R_2 are the principle radii of curvature of body 1, $R_1^{'}$ and $R_2^{'}$ are the principle radii of curvature of body 2, and φ is the angle between the principal axes of bodies 1 and 2. For a sphere of radius a_p interacting with a flat surface, $\lambda_1\lambda_2$ becomes:

$$\lambda_1\lambda_2 = \frac{1}{a_p^2} \tag{3.39}$$

This technique is only suitable for small separation distances between the two interacting bodies, and still not suitable for small size probes. Moreover, considering a rough surface, due to the variation of separation distance at different locations on the projected area between the probe and the surface, Derjaguin approximation fails to represent the exact interaction energy. The height variation is imposed by surface heterogeneities and their size relative to the interacting probe radius. On the other hand, an analytical study similar to the section 3.3 to determine the interaction between an exact shape probe, and a heterogeneous surface is not feasible.

Consequently, a numerical approach based on surface element integration [Bhattacharjee and Elimelech, 1997] (SEI) method is proposed to determine the DLVO interaction energy between the exact shape of a model probe and a model heterogenous surface as illustrated in Figures 3.2 or 3.5. In this regard, the van der Waals and electrostatic energy per unit area expressions have to be integrated over the surfaces of the two interacting bodies. The interaction energy per unit area for van der Waals energy is given by Eqn. (3.8). For electrostatic interaction the LSA expression (Eqn. 3.9) was used in the analytical derivations in section 3.3, in order to make the calculations straight forward. However, in the numerical analysis, both the LSA, and HHF [Hogg et al., 1966] expressions have been employed as the energy per unit area to compute the electrostatic energy. The HHF expression for the electrostatic interaction energy per unit area between two infinite flat plates (which has been discussed more in depth in chapter 2) is:

$$U_{Hogg} = \frac{\epsilon\kappa}{2}\{(\psi_1^2 + \psi_2^2)[1 - \coth(\kappa h)] + 2\psi_1\psi_2 \mathrm{cosech}(\kappa h)\} \tag{3.40}$$

Here, ψ_1, and ψ_2 are the surface potentials for the probe and the heterogenous surface respectively, and κ is the inverse Debye screening length.

The flowchart in Figure 3.10 depicts the steps through which the numerical methodology has been developed to investigate the DLVO interaction between an AFM probe and a substrate as a function of separation distance. This flowchart describes the calculation steps associated with the electrostatic component of the DLVO interaction energy. The calculations for van der Waals energy follows the same structure, except the dashed part shown in Figure 3.10, which represent the expressions for interaction energy per unit area. For electrostatic interaction energy, these expressions can be obtained from Eqns. (3.9, 3.40), while for van der Waals interaction energy, one needs to replace the above expressions by Eqn. (3.8). Based on the DLVO energy selected component, a set of constant parameter/parameters related to that energy have to be imported to the program. For van der Waals interaction energy, the Hamaker constant A_H, which is proportional to the magnitude of the dispersion force needs to be imported. This constant is a function of the material properties of both the interacting bodies, and can be estimated through the following equation [Butt et al., 2003].

$$A_H = 3/4k_BT\left(\frac{\epsilon_1-\epsilon_3}{\epsilon_1+\epsilon_3}\right)\left(\frac{\epsilon_2-\epsilon_3}{\epsilon_2+\epsilon_3}\right) + \frac{3h\nu_e}{8\sqrt{2}}\frac{(n_1^2-n_3^2)(n_2^2-n_3^2)}{\sqrt{n_1^2+n_3^2}\sqrt{n_2^2+n_3^2}(\sqrt{n_1^2+n_3^2}\sqrt{n_2^2+n_3^2})} \tag{3.41}$$

In this equation, $k_B = 1.381 \times 10^{-23}\ JK^{-1}$ is the Boltzmann constant, $h \simeq 6.626 \times 10^{-34}\ Js$ is the Planck's constant, and $\nu_e \simeq 3.3 \times 10^{15}$ Hz is the mean ionization frequency. Index i refers to the materials of the interacting bodies, and the intervening aqueous medium. In order to imitate the actual force measurement by AFM, the materials for indices $i = 1, 2$, and 3 are selected as silicon nitride Si_3N_4, silica, and water. ϵ_i is the dielectric permittivity, which is 7.4, 3.8, and 80 (for water) respectively. n_i is the reflective index, which is 1.988, 1.448, and 1.33 for $i = 1,\ 2$, and 3. Therefore, the Hamaker constant

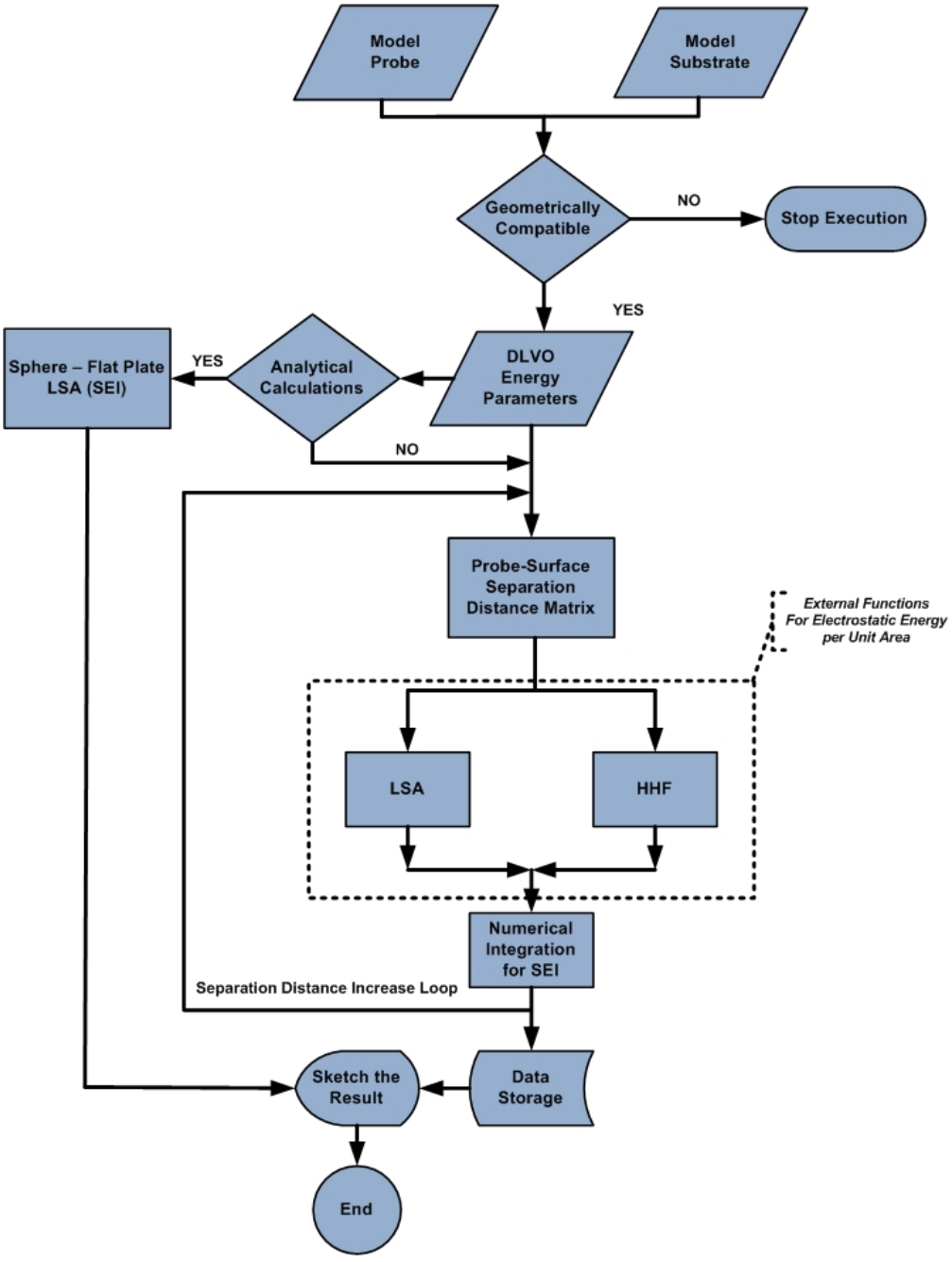

Figure 3.10: A flowchart describing the numerical approach proposed by employing SEI to derive the electrostatic interaction energy between a model probe and a model substrate.

can be evaluated as:

$$A_H \quad = 2.258 \times 10^{-20} J \tag{3.42}$$

For the electrostatic interaction energy, a set of other constant parameters need to be imported to the computations as the inputs, regardless of whether LSA expression, Eqn. (3.9), or HHF Expression, Eqn. (3.40), is selected. Some of these parameters, such as the vacuum permittivity, $\epsilon_0 = 8.854 \times 10^{-12}$, dielectric constant of water, $\epsilon_r = 78.5$, elementary charge, $e = 1.602 \times 10^{-19}$C, Boltzmann constant $k_B = 1.381 \times 10^{-23}$, and temperature, $T = 298K$, are globally set to a constant value. However other parameters need to be calculated or estimated depending on the electrolyte solution and the material properties of the system. These parameters are: the ionic valence of the symmetric electrolyte, ν, Debye screening length, κ^{-1}, and the surface potentials, ψ_1 and ψ_2. As stated in chapter 2, κ is a function of electrolyte solution ionic concentration or molarity M, and is calculated using the following equation [Masliyah and Bhattacharjee, 2006].

$$\kappa^{-1} = \frac{3.04}{z\sqrt{M}} \times 10^{-10} \text{ m} \tag{3.43}$$

where z is the valance of the ionic species, that for KCl is equal to 1. As addressed earlier in Chapter 2 (section 2.2.2), the electrostatic double layer energy based on the linearized form of Poisson-Boltzmann (PB) equation ($i.e.$, HHF expression), is seriously overestimated under constant surface charge boundary condition. Therefore, in this study, the surfaces have been assigned to have a constant surface potential, rather than a constant charge density. The magnitude of the surface potential ψ has been assumed to be in the range of $\pm$ 25 mV to $\pm$ 70 mV in other studies [Bowen and Doneva, 2000, Chapel, 1994, Considine and Drummond, 2001, Ducker et al., 1992, Horn et al., 1989, Janusz et al., 2003]. Thus in the present study, ψ_1, and ψ_2 are equally set to -50 mV, which falls within the above range.

As the flowchart shows, the model probe and substrate must also have been generated earlier in separate files, and then be imported to the energy

calculation program as two individual inputs. These inputs are in the form of two individual $n \times 3$ matrices, and must be compatible with each other. It means that the first two columns of both the matrices, which represent the X and Y addresses of the modeled structures in the Cartesian coordinate system, must be exactly identical. To this end, the length and mesh size of the modeled geometries in X and Y directions must have the same values. If this criteria fails to be met, further energy calculations will be terminated.

Once the input parameters are inserted, and the input model geometries are checked to be compatible with each other for interaction energy calculations, the user is asked to select the energy per unit area expression which will be used in SEI calculations. As illustrated in Figure 3.10, for electrostatic energy, LSA, Eqn. (3.9), or HHF, Eqn. (3.40), expressions can be selected, while for van der Waals energy, the Hamaker's expression, Eqn. (3.8), is the only option for numerical calculations. As an alternative to the numerical analysis, the analytically calculated interaction energy is provided for a restrictive case of a spherical probe interacting with a smooth flat plate based on Hamaker's approach and Derjaguin approximation. Likewise, the interaction of a hemispherical probe and a flat plate is analytically calculated based on SEI technique. These analytical expressions will be used to check the accuracy and precision of the proposed numerical approach (*cf*. section 3.4.3). For electrostatic interaction energy, the corresponding analytical relation is derived by employing the LSA expression into the SEI technique. However, for van der Waals interaction energy, in addition to the SEI calculations, the well-known Derjaguin, and Hamaker's expressions have also been included (*cf*. section 3.4.3).

Apart from analytical equations subroutine, as the next step in the numerical analysis, an initial height matrix will be generated, which has the same size of the model probe or model substrate matrix. The height matrix is produced by subtracting each element of the third column of the model substrate matrix from the corresponding element in the model probe matrix. As it was stated in section 3.2.2, the third column of the matrix represents the Z (height) value

of the modeled body. In other words, this matrix gives the initial separation distance between the two modeled surfaces in the XY plane. The minimum separation between the closest points of the probe and the substrate is set at the van der Waals cut-off distance, which is $h_0 = 0.158$ nm [Masliyah and Bhattacharjee, 2006]. It is important to explain here, that all of the sizes of the modeled geometries in the energy calculations are scaled with respect to the size (radius) of the asperities of the rough surface. If the probe is interacting with a smooth flat plate, rather than a rough surface, the sizes are scaled with respect to radius of the interacting probe spherical cap. In the next step, the minimum separation distance increases gradually with a certain step, which enables the program to calculate the interaction energy as a function of the separation distance. Subsequently, this matrix will be converted to a square matrix in which its rows represent the coordinates of the meshes along the X direction, and its columns represent the coordinates of the meshes along the Y direction. The values of each element in this matrix is assigned by an element in the third column of the previous $(n \times 3)$ matrix, which corresponds to that specific X and Y coordinates in the squared matrix. This conversion is to facilitate the numerical integration in the Cartesian coordinates system.

According to the interaction energy per unit area expression selected by the user, the values of the interaction energy will be calculated for all of the elements in the separation distance matrix individually. Then, the numerical integration over the surfaces of model probe and model substrate will be performed, first along the X direction, and then along the Y direction. For numerical integration process of the SEI technique, the trapezoidal rule [Press et al., 1992] is employed which has the following form in one dimensional integration.

$$\int_{x_1}^{x_2} f(x)\,dx \simeq \frac{\Delta x}{2}(f_1 + 2 + f_2 + 2f_3 + \ldots + 2f_n + f_{n+1}) + \mathbf{O}(\Delta x^3 f'') \quad (3.44)$$

Here, x_1 and x_2 are the integration limits, and Δx is the size of the discretized integration interval along the X direction. The approximation shown

in Eqn. (3.44) can be extended for a multi-dimensional integration as:

$$\int_{y_1}^{y_2}\int_{x_1}^{x_2} f(x,y)\,dxdy \simeq (\frac{\Delta x}{2})(\frac{\Delta y}{2})\sum_{j=1}^{m}\sum_{i=1}^{n} w_{i,j}f_{ij} \tag{3.45}$$

where Δx and Δy are the step sizes in X and Y direction, and n and m are the number of intervals. $w_{i,j}$ is a n by m coefficient matrix in the form of:

$$w_{i,j} = \begin{bmatrix} 1 & 2 & 2 & \dots & 2 & 1 \\ 2 & 4 & 4 & \dots & 4 & 1 \\ 2 & 4 & 4 & \dots & 4 & 1 \\ . & . & . & \dots & . & . \\ . & . & . & \dots & . & . \\ . & . & . & \dots & . & . \\ 2 & 4 & 4 & \dots & 4 & 1 \\ 1 & 2 & 2 & \dots & 2 & 1 \end{bmatrix}_{n\times m} \tag{3.46}$$

In the current study, Δx and Δy are chosen such that $\left|\frac{\Delta x}{x_2-x_1}\right|$ or $\left|\frac{\Delta y}{y_2-y_1}\right| \leq 0.01$. Then, with such a griding resolution, the numerical SEI calculations become sufficiently accurate.

The total interaction energy between the probe and substrate calculated from Eqn. (3.45), is stored in a separate matrix. This process is repeated until the distance reaches the desired value set by the user. The normalized interaction energy is then plotted with respect to the scaled separation, $h^* = h/a$, where a is either equal to a_s (radius of the roughness asperity), or a_p (probe radius), if the substrate is considered to be a flat surface. A correction in the calculated interaction energy is also provided in the program as an option. This correction is only applicable to the conical or hemispherical probes, when interacting with a flat surface, and stems from the regions in the structure of the modeled probe that are spurious. These extra parts are observed in Figures 3.4 and 3.5b as four flat portions at the top surface of the probe. The correction process is described later in section 3.4.3.

3.4.2 Energy Distribution as a Result of Probe Lateral Movement

Using the numerical approach proposed in section 3.4.1, one is able to investigate the DLVO interaction energy as a function of the separation distance between a model probe and a model substrate. However, as stated in section 3.2.1, the minimum separation distance h_0 between the two modeled geometries will vary based on the relative lateral position of model probe over the model surface, and also the relative size of the asperities in comparison with the probe radius. This has been depicted in Figure 3.11, where in Figure 3.11a the influence of the lateral position, and in Figure 3.11b the influence of the relative asperity size a_s on h_0 are illustrated. Neglecting the effect of the minimum separation distance may result in completely misleading results for short-range interaction energies, and hence a deceptive conclusion about the energy characterization based on the surface roughness. Other studies [Hoek and Agarwal, 2006, Zhao et al., 2008] have conducted the SEI numerical analysis to distinguish the influence of surface roughness, regardless to this phenomenon. However, they have tried to reconcile the effect of minimum separation distance by presenting an average of the interaction energies.

To this end, in this study, it has been attempted to establish a geometrical analysis, employing a regular geometrical pattern, in order to investigate the energy distribution as a function of the probe position. Assuming that roughness asperities are patterned in a uniformly distributed form shown in Figure 3.1, one can define a geometrical condition for the radius of probe, which determines whether it is possible that the probe touches the bottom flat part of the substrate or not. This relation is a function of asperity radius and the pitch distance as shown below:

$$a_p \leq 1/2 \left(\frac{P^2}{2a_s} - a_s \right) \tag{3.47}$$

Only if the inequality in Eqn. (3.47) holds, the probe is able to come into contact with the bottom flat surface of the substrate, depending on its lateral

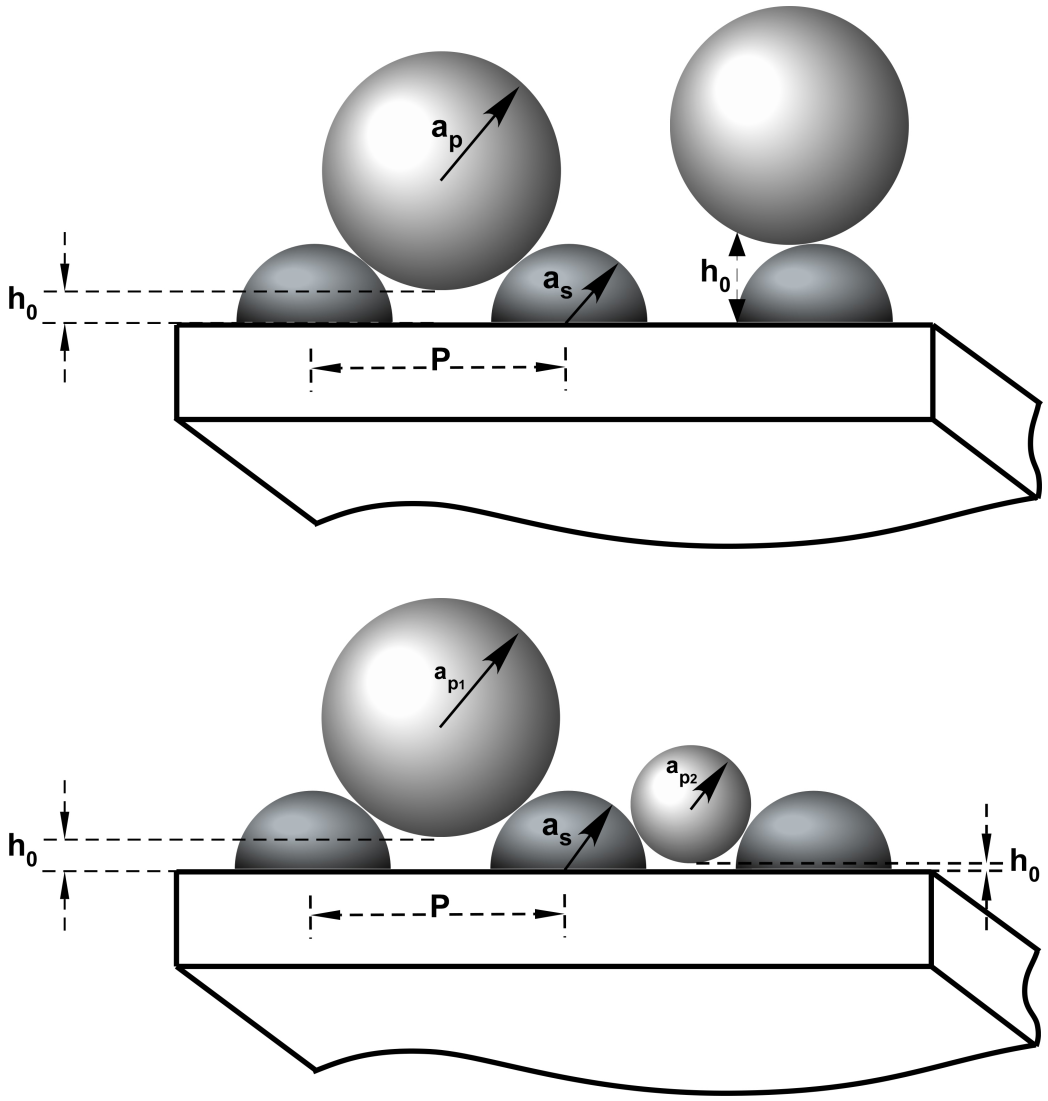

Figure 3.11: A schematic depicting the minimum possible separation as a result of: **(a)** lateral location of probe with respect to the asperity, and **(b)** relative size of probe and surface roughness.

configuration with respect to the asperities. Otherwise, the probe will always remain at a certain height away from the bottom surface, while touching the top of the asperities similar to the left spherical probe with radius a_{p1} in Figure 3.11 b.

On the other hand, regardless to geometrical condition in Eqn. (3.47), the minimum separation between the lowest point of probe and the bottom flat surface of the substrate is assigned by the lateral position of the probe as shown in Figure 3.11a. Assuming the origin of the spherical asperity in the unit cell has (0,0,0) coordinates, and the bottom point of a spherical probe (*e.g.*, Figure 3.11) is at (x_0, y_0, z_0), the minimum separation distance h_0 can be found from the following relation.

$$h_0 = z_0 = -a_p + \sqrt{(a_s + a_p)^2 - (x_0)^2 - (y_0)^2} \tag{3.48}$$

A similar numerical analysis using SEI technique as in section 3.4.1 is developed, such that the energy distribution based on minimum separation distance criteria will be investigated. The flowchart in Figure 3.12 illustrates the steps followed by the program for these calculations. In this analysis, the probe is relocated along the unit cell in Figure 3.1, and the corresponding interaction energy is stored for each location. The stored data will be used to create a 3D energy distribution map. The results for the energy distribution are discussed in chapter 5, where it is attempted to mathematically formulate these maps by curve fitting. It is pertinent to mention that due to periodicity of surface roughness, the aforementioned unit cell represents the entire surface.

3.4.3 Validation of the Numerical Calculations

Before proceeding to the numerical analysis to characterize the influence of surface roughness on the DLVO interactions, the accuracy of the numerical model proposed in the last subsection has to be investigated. Therefore, the interaction between a simplified case of a hemispherical probe and a flat plate is simulated, in order to compare the values of the numerically obtained energies against the corresponding analytical results for the DLVO interaction energy

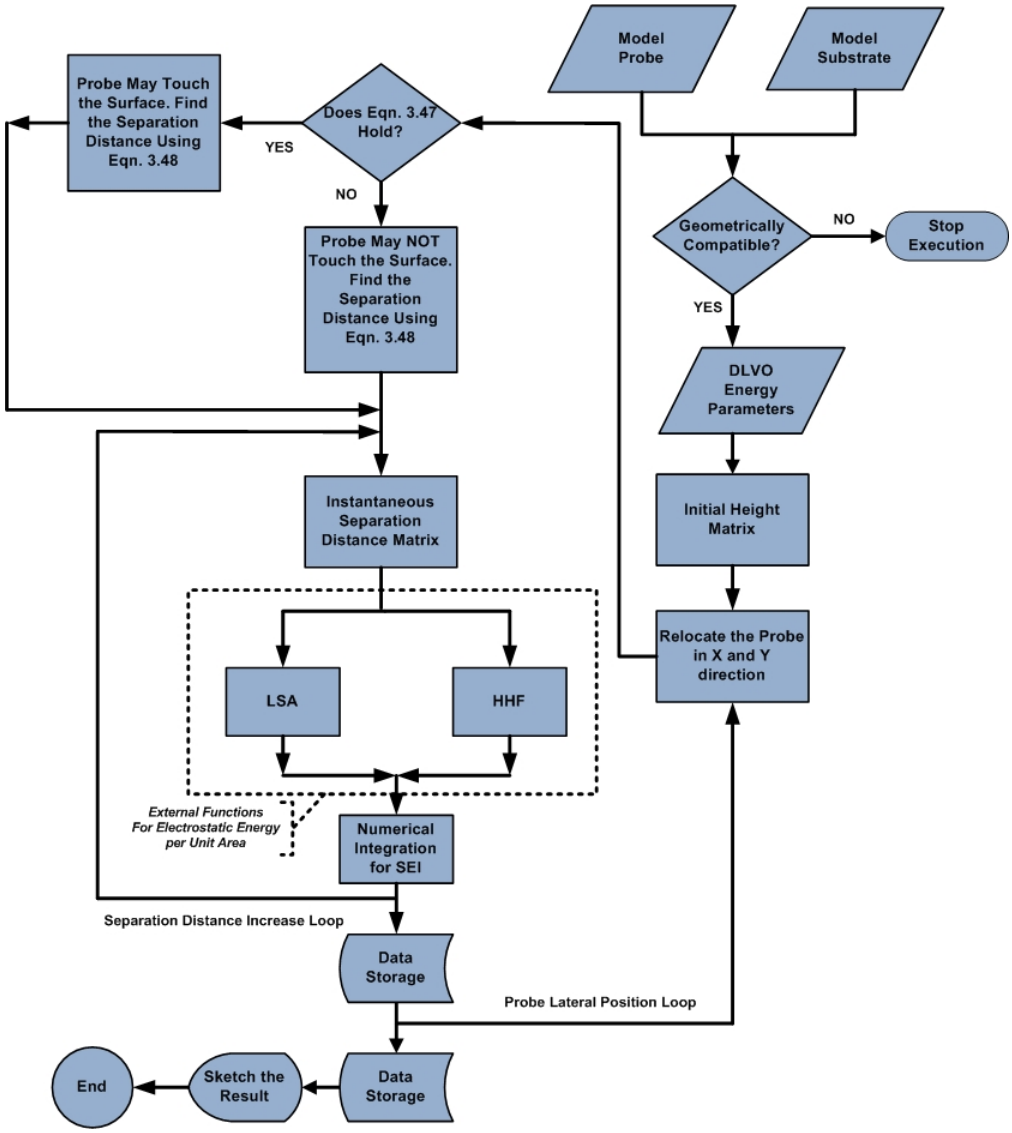

Figure 3.12: A flowchart describing the program associated to the SEI numerical calculation of electrostatic energy distribution along a unit cell (*cf.*, Figure 3.1) to investigate the influence of minimum separation distance.

components. In this regard, a 20 nm radius probe is modeled similar to the structure shown in Figure 3.4. The mesh size in both the model probe and the interacting smooth flat plate in this case is 0.2 nm by 0.2 nm.

van der Waals Interaction

Assuming the energy per unit area for the van der Waals interaction as Eqn. (3.8), by employing SEI technique, the exact interaction between a hemispherical probe with radius a_p and a smooth flat plate with the minimum separation distance of h_0 can be analytically derived as:

$$U_{VDW_{(SEI)}} = -\frac{A_H}{6}\left[\frac{a_p}{h_0} + \ln(\frac{h_0}{a_p + h_0})\right] \tag{3.49}$$

The van der Waals energy expression based on the Hamaker approach for a sphere interacting with a smooth surface is:

$$U_{VDW_{(Hamaker)}} = -\frac{A_H}{6}\left[\frac{a_p}{h_0} + \frac{a_p}{h_0 + 2a_p} + \ln(\frac{h_0}{h_0 + 2a_p})\right] \tag{3.50}$$

The Derjaguin approximation method suggests the corresponding interaction energy as:

$$U_{VDW_{(DA)}} = -\frac{A_H a_p}{6h_0} \tag{3.51}$$

Figure 3.13 depicts the van der Waals interaction energy versus the scaled separation for interactions obtained from the numerical model, and also the analytical results based on the Eqns. (3.49) to (3.51). In this plot, the interaction energy is normalized with respect to the Hamaker constant A_H. The numerical results based on SEI illustrated with triangular symbols have overlapped to the analytical results predicted based on the SEI technique in Eqn. (3.49) shown as solid line. Therefore, the numerical model proposed in this study sufficiently provides a good accuracy in the van der Waals interaction energy calculations by employing the SEI approach.

On the other hand, the Hamaker's expression in Eqn. (3.50) predicts a lesser interaction energy as illustrated with circular symbols. This is due to the

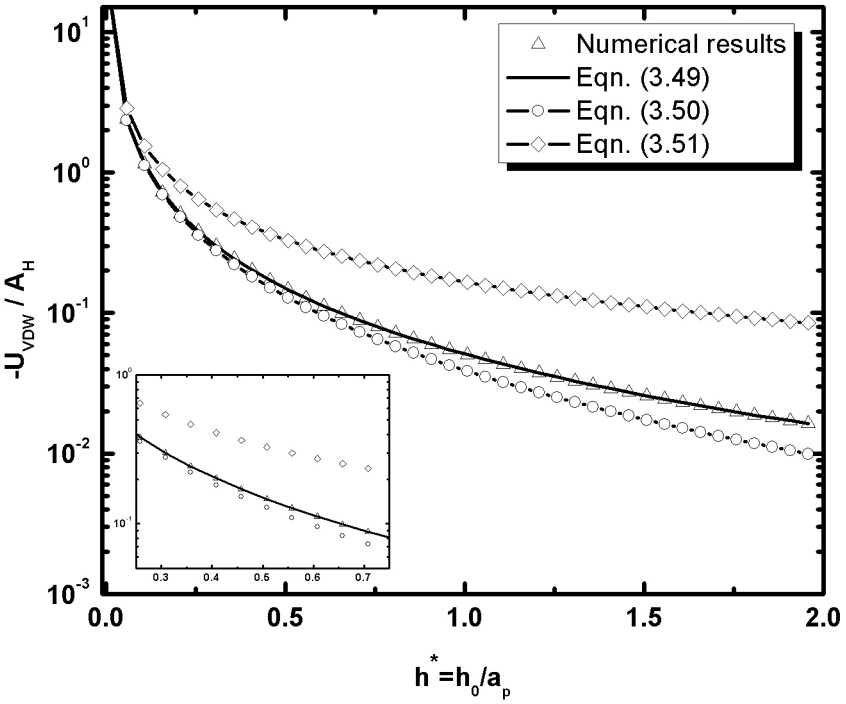

Figure 3.13: Variation of normalized van der Waals interaction energy versus the scaled separation distance for a hemispherical probe with radius of 20 nm, interacting with a flat plate. Solid line depicts the interaction energy corresponding to the SEI analytical expression, diamond symbols represent the Hamaker's expression Eqn. (3.50), and triangular symbols represent the numerically obtained interaction energies. The separation distance is scaled with respect to the probe radius a_p.

reason that the Hamaker's equation (Eqn. 3.50) declares the interaction energy for a spherical body, while the results based on SEI technique, depict the van der Waals energy for an open hemispherical geometry. The SEI technique is developed based on the divergence theorem (Gauss' theorem), which considers that the integrating surface is a closed surface. Owing to the fact that a hemisphere is an open surface, the energies resulted from SEI for a hemisphere also corresponds to the energy of a hypothetical cylinder with infinite height attaching on top of the hemisphere.

The results based on Derjaguin approximation shown in diamond symbols determines the interaction energy quite accurately at small separation distance, while it fails to provide a good estimation at larger distances as it was expected.

Electrostatic Interaction

The numerical results for electrostatic interaction energy also need to be validated. Both HHF and LSA expressions (*i.e.*, Eqns. (3.40) and (3.9), respectively) were applied in the numerical computations. However, the results are validated based on the analytically derived expressions for the electrostatic interaction based on LSA expressions as:

$$U_{EDL_{(LSA)}} = A_c \exp(-\kappa h_0) \left[\frac{\exp(-\kappa a_p) + \kappa a_p - 1}{\kappa^2} \right] \tag{3.52}$$

where A_c is:

$$A_c = 64\pi\epsilon_0\epsilon_r\kappa \tanh(\frac{\nu e\psi_1}{4k_BT}) \tanh(\frac{\nu e\psi_2}{4k_BT})(\frac{k_BT}{\nu e})^2 \tag{3.53}$$

Figure 3.14 shows the variation of the normalized electrostatic interaction energy for a hemispherical probe interacting with a smooth flat plate against their scaled separation distance. The solid line represents the interactions associated with the analytical calculations based on LSA expression. The diamond, and triangular symbols depict the numerical results based on LSA, and HHF expressions, respectively. Based on these results, The numerical

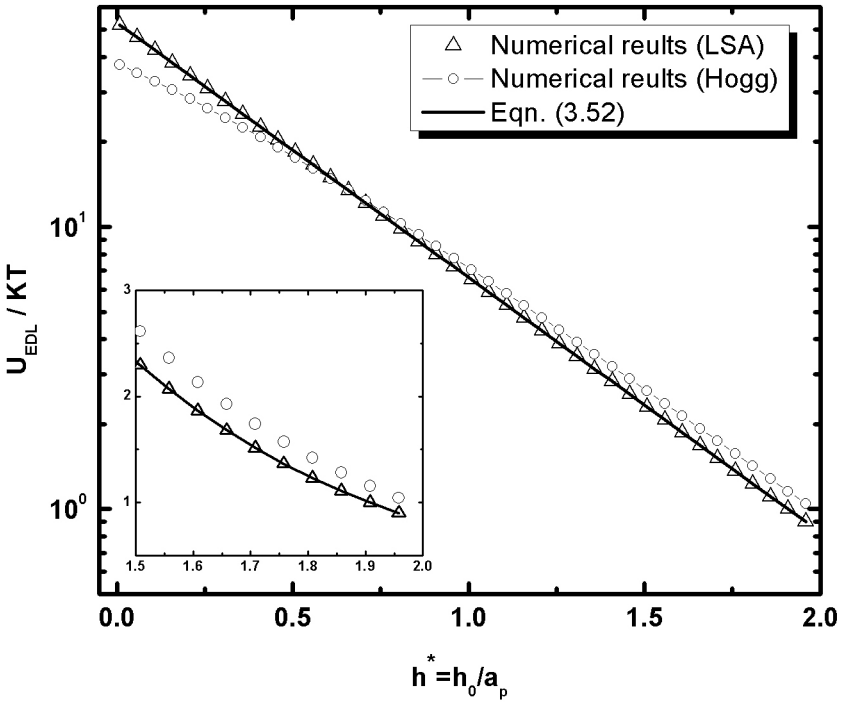

Figure 3.14: Variation of normalized electrostatic interaction energy versus the scaled separation distance for a hemispherical probe with radius of 20 nm, interaction with a flat plate. Solid line depicts the interaction energy corresponding to the SEI analytical derivation based on LSA expression, while square and triangular symbols represent the numerically obtained interactions based on the LSA, and the Hogg *et al*. expressions employed in SEI technique, respectively. The separation distance is scaled with respect to the probe radius.

model provides sufficiently accurate results for electrostatic component of the DLVO interaction energy as well.

3.5 Assessing the Interaction Energy for a Model Probe with Circular Base

As stated in section 3.2.2, in the present study, the AFM probe is mathematically modeled as a pyramidal, conical, or hemispherical shape. Both the hemispherical and conical shape model probes (Figures 3.4, and 3.5b) have a circular base. In SEI calculations however, the interaction energy is investigated for the space trapped between the surface of the probe and its projected area over the interacting substrate. Since the model substrate is a square in XY plane, to facilitate the numerical integration in SEI calculations, four extra flat corners have been added to the circular base of the model probe, in order to make its projected area identical to the projected area of the substrate. However, Eqns. (3.49) and (3.52), used to validate the numerical results, account only for the interaction energy resulting from the real geometry of a hemisphere. As a result, they must have predicted less energy. For a hemisphere with radius a_p the area of the excessive corners is $(4a_p^2 - \pi a_p^2)$. Therefore the corresponding van der Waals interaction is

$$U_{VDWcorners} = -\frac{A_H(4a_p^2 - \pi a_p^2)}{12\pi h^2} \tag{3.54}$$

and the corresponding electrostatic interaction based on LSA expression is given by:

$$U_{EDLcorners} = A_c(4a_p^2 - \pi a_p^2)\exp(-\kappa h) \tag{3.55}$$

where h is the instantaneous separation distance between the top flat base of the probe and the interacting substrate. h is equal to a_p, when the probe is in contact with the surface.

Figure 3.15 illustrates the deviation in the interaction energy imposed by considering the 4 excessive corners into the energy calculation for a 20 nm radius hemispherical probe interacting with a flat plate. For both the van der Waals and electrostatic energies, this deviation is very small.

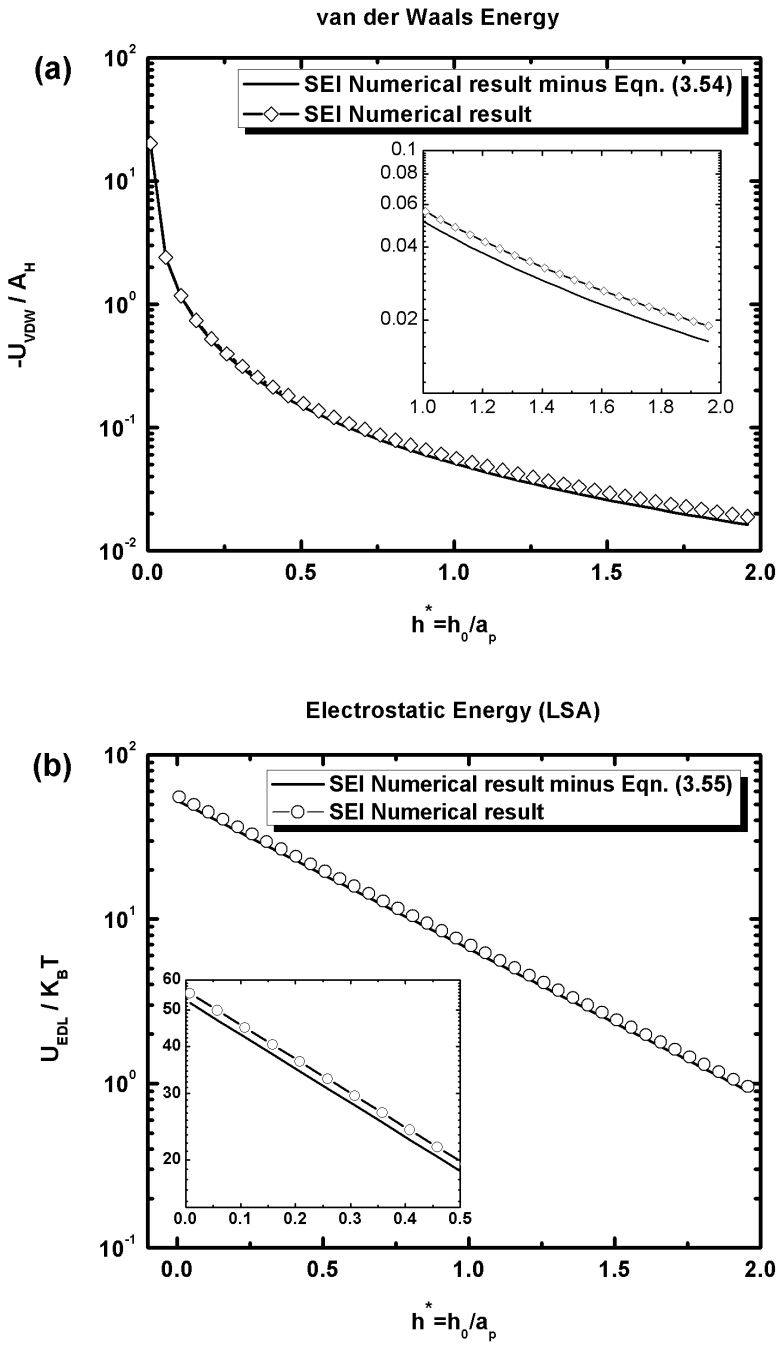

Figure 3.15: The deviation in **(a)** van der Waals, and **(b)** electrostatic interaction energies between a 20 nm radius hemispherical probe, and a flat surface resulting from the excessive areas considered in the mathematical model of the hemispherical probe. The solid lines represent the corrected values of the energies.

3.6 DLVO Interaction Force between AFM Probe and a Flat Surface

As mentioned earlier in Chapter 2, in this study, to experimentally deal with the correlation of colloidal interactions and surface heterogeneities, AFM is employed to find the interaction force between a DNP-S20 probe and the substrate underneath. In order to verify the accuracy of the experimental results, in this section the interaction energy between a model probe as in Figure 3.6a and a flat surface are calculated theoretically. These calculations can be used to compare the AFM results over glass (as a smooth surface) with theoretically calculated forces.

Integrating the Hamaker's expression (*i.e.*, Eqn. (3.8) over the surface of the hemispherical tip, one can find the van der Waals interaction energy $U_{S_{VDW}}$ for the hemispherical section with radius a_s, separated at a distance h_0 from the smooth surface as following.

$$U_{S_{VDW}} = -\frac{A_H}{6}\left[\frac{a_s}{h_0} + \ln\left(\frac{h_0}{a_s + h_0}\right)\right] \tag{3.56}$$

This equation is similar to the second term in Eqn. (3.13), which was used to explain the interaction between a rough surface consisting of hemispherical asperities and a smooth flat plate. Correspondingly, the interacting force can be derived by differentiating the Eqn. (3.56) with respect to distance h_0 as:

$$F_{S_{VDW}} = -\frac{dU_{S_{VDW}}}{dh_0} = -\frac{A_H}{6}\left[\frac{h_0^2}{h(a_s h_0 + h_0^2)}\right] \tag{3.57}$$

Similarly, the equations for electrostatic interaction energy and force for hemispherical model probe are derived using the LSA expression as:

$$U_{S_{EDL}} = \exp(-\kappa h_0)\left[A_c\left(\frac{\exp(-\kappa a_s) + \kappa a_s - 1}{\kappa^2}\right)\right] \tag{3.58}$$

$$F_{S_{EDL}} = -\frac{dU_{S_{EDL}}}{dh_0} = \kappa\exp(-\kappa h_0)\left[A_c\left(\frac{\exp(-\kappa a_s) + \kappa a - 1}{\kappa^2}\right)\right] \tag{3.59}$$

where in the above two equations A_c is a constant defined as:

$$A_c = 64\pi\epsilon_0\epsilon_r\kappa \tanh\left(\frac{\nu e\psi_1}{4k_BT}\right)\tanh\left(\frac{\nu e\psi_2}{4k_BT}\right)\left(\frac{k_BT}{\nu e}\right)^2 \tag{3.60}$$

The interaction energies corresponding to the truncated conical section of the model tip are calculated by integrating the interaction energies per unit area over its surface in polar form, while the instantaneous separation distance h between in the integrating element and the flat surface is:

$$h = h_0 + a_s + \left(\frac{r - a_s}{b - a_s}\right) H \tag{3.61}$$

Here, r is the radius of the integrating ring element with a separation distance h from the flat surface, a_s (*i.e.*, hemispherical tip radius) and b are the radius of the truncated cone upper and lower circular bases, and H is its height. These geometrical parameters can be defined according to the labels shown on Figure 3.6a as: $a_s = R$, $b = L/2$, and $H = h$.

The van der Waals interaction energy for this geometry is:

$$\begin{aligned} U_{C_{VDW}} &= -\frac{A_H}{6}\left(\frac{b - a_s}{H^2}\right)\left[(b - a_s)\ln\left(\frac{a_s + h_0 + H}{a_s + h_0}\right)\right] \\ &\quad -\frac{A_H}{6}\left(\frac{b - a_s}{H^2}\right)\left[\left(a_s^2 + (H + h_0 - b)a_s - bh_0\right)\right] \\ &\quad \left[\left(\frac{H}{(a_s + h_0)(a_s + h_0 + H)}\right)\right] \end{aligned} \tag{3.62}$$

Subsequently, the van der Waals force can be calculated as:

$$\begin{aligned} F_{C_{VDW}} &= \frac{A_H}{6}\left(\frac{b - a_s}{H^2}\right)\left[\frac{2H(a_s - b)}{(a_s + h_0 + H)(a_s + h_0)}\right] \\ &\quad -\frac{A_H}{6}\left(\frac{b - a_s}{H^2}\right)\left[\frac{H(2a_s + 2h_0 + H)[a^2 + (H + h_0 - b)a_s] - bh}{(a_s + h_0)^2(a_s + h_0 + H)^2}\right] \end{aligned} \tag{3.63}$$

The electrostatic interaction energy and force for this shape are also presented in Eqns. (3.64) and (3.65)

$$U_{C_{EDL}} = -A_c B_c \exp(-\kappa h_0 - \kappa a_s) \tag{3.64}$$

$$F_{C_{EDL}} = -A_c B_c \kappa \exp(-\kappa h_0 - \kappa a_s) \tag{3.65}$$

where A_c is replaced from Eqn. (3.60), and B_c is defined as:

$$B_c = \frac{(a_s - b)\left[\exp(-\kappa H)(a_s - b - \kappa H b) - (a_s - b - \kappa H a_s)\right]}{(\kappa H)^2} \tag{3.66}$$

Thus, to predict the overall DLVO interaction energy between a model probe depicted in Figure 3.6a and a flat surface, all the attractive van der Waals and repulsive electrostatic components represented in Eqns. (3.57, 3.59, 3.63, and 3.65), must be added together to form the DLVO energy curve. This curve is used to verify how realistic and accurate the forces measured experimentally with AFM are.

3.7 Summary

In this chapter, the theoretical methodology developed for calculation of DLVO energy by considering the effect of surface roughness was explained. It was shown that how rough surfaces are modeled for such energy characterizations by defining uniformly distributed asperities in different predefined shapes. Modeling of an approaching probe was also explained. The geometry of the modeled probe is either in simple downward faced hemispherical, or more realistic pyramidal or conical shape, representing a DNP-S20 AFM probe. Moreover, even the pyramidal or conical structures can be generated by two different methods for attaching the spherical cap of the probe.

Surface element integration technique was used to derive a set of analytical equations that can comprehensively explain the DLVO energy between a flat and a rough surface consisting the mathematically generated uniform asperities. Such asperities have hemispherical, conical or cylindrical geometries in protruding or depressed forms. These equations can be used to characterize

the interfacial energies based on the magnitude of influence of surface roughness in these energies in terms of the shape, size, and distribution density of the mathematical asperities.

Additionally, the numerical methodology for finding the interaction between an approaching probe (instead of a flat surface) and a rough surface was explained. These numerical analyses are to firstly find the energy variation as a hemispherical probe change its lateral position over the rough surface as a function of the minimum separation distance. Furthermore, these numerical calculation can be used to replace the interacting flat surface with previously described model probes. Such an investigation gives a better insight into the simulation of the AFM force measurement process. The Numerical calculations were validated by comparing the existing analytical expressions for simpler cases, and the precision of the results were reasonably satisfactory.

Chapter 4

Atomic Force Microscopy as a Tool for Measurement of Colloidal Interactions

4.1 Introduction

In this study, atomic force microscopy (AFM) [Binnig et al., 1986] technique was used to measure the colloidal forces, in order to investigate the influence of surface roughness, and the impact of physical heterogeneities on the interaction energies. Many other studies [Giesbers, 2001,Liu, 2004,Zhao, 2009], previously, used the well-known method of *Colloidal Probe Technique*, first developed by Ducker *et al.* [Ducker et al., 1991,Ducker et al., 1992] and Butt [Butt, 1991]. In this method, a particle of 1 to 50 μm radius is attached to the AFM cantilever to determine the forces. However, the use of a large-size particle causes larger interaction, and also decreases the sensitivity of detection of the nano-scale heterogeneities. To this end, the AFM force measurements, in this study, are conducted by employing the original sharp-tip end AFM probes which would provide accurate information about the surface topography, as well as the interfacial interactions between the probe and the sample surface. The substrates used in these analyses have been selected such that they comprise reasonable variation of surface topography, so that different force profiles are expected to be seen in experimental measurement as a result of this variety. In section 4.2.1 the two general AFM scanning operations are briefly intro-

duced, and then the geometrical information regarding the interacting probe and substrates are presented. Following to this, an AFM topographical and roughness analysis over the sample heterogenous surfaces is explained, and the limitations of the AFM scanning are assessed. Section 4.3 describes the AFM force measurement operation, and it also provides the experimental set-up and procedure in the current study. Finally, section 4.4 provides a post-processing method regarding the calculation of the Hamaker constant A_H based on the experimental force measurement.

4.2 AFM Topography Analysis

4.2.1 AFM Imaging

To determine the surface topography, an Atomic Force Microscope (Veeco, Digital Instruments (DI), Santa Barbara, USA) was used to scan the surface, employing the Contact Mode (CM) and Tapping Mode (TM) techniques in air. In contact mode scanning, the AFM probe is continuously in a gentle contact with the surface. Due to the topographical features of the sample surface, a deflection is imposed to the cantilever as it scans the surface. To minimize the force on the sample surface, a feedback loop attempts to keep the deflection of the cantilever constant, as the cantilever tip scans over the surface, by moving the piezo-electric tube (cantilever support) up and down. Conversely, in tapping mode, the cantilever oscillates at its resonance frequency, and is brought close to surface until the probe briefly contacts the sample surface at the bottom of each oscillation cycle. The contact between the cantilever and surface causes a reduction of oscillation amplitude. During scanning, similar to the contact mode, a feedback loop adjusts the vertical position of the piezo-electric tube, such that the amplitude of cantilever oscillation is at its initial value. This mode is suitable for a wide variety of substrates with soft surfaces where the frictional force resulting from the movement of the probe over the surface may damage the asperities or deposited particles.

The scanning probes are obtained from Veeco NanoProbe^{TM}. The DNP-

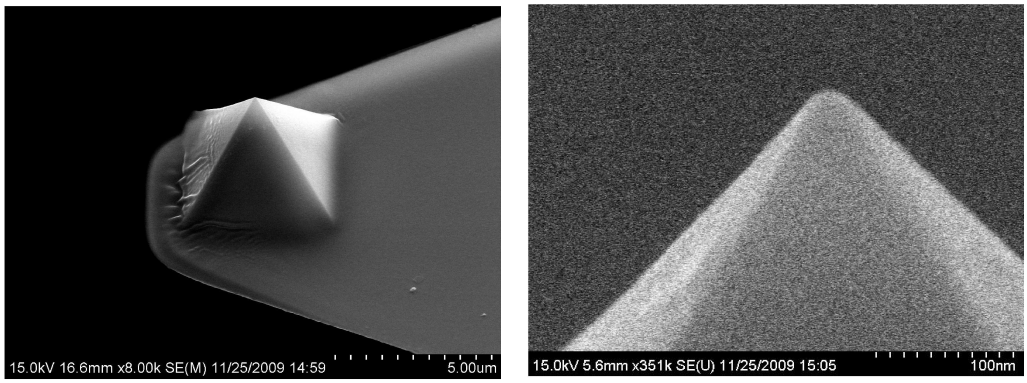

(a) (b)

Figure 4.1: SEM images of AFM silicon nitride (Si_3N_4) DNP tip. **(a)** 45° titled zoom-out image of the pyramidal tip attached to the cantilever. **(b)** 0° titled zoom-in image of the same tip. The total height of the probe is roughly 6 μm, while its base is a 4 μm × 4 μm square. The spherical tip radius is roughly between 18 to 20 nm. The images were taken with a Hitachi SEM in the National Institute for Nanotechnology (NINT) SEM facility. (Images are taken by Daniel Salamon, technical officer, Electron Microscopy, NINT).

Table 4.1: Scanning probe geometrical information

	DNP-S20	**RTESP7**
Material	Silicon Nitride	Silicon
Cantilever Length μm	120, 205	125
Cantilever Width μm	25, 40	35
Tip Height μm	2.5 to 8	15 to 20
Tip Radius nm	20	15
Frequency (KHz)	18 to 57	300
k (N/m)	0.06 to 0.58	40

Table 4.2: Rough sample substrates geometrical information

Substrate	**Pitch** μm	**Tip Edge Radii nm**	**Height Step nm**
nanopost-low	0.23	-	10-20
nanopost-mid	0.23	-	100-200
DI standard	10	-	200
TGT01	3	10	500-1000
TGX01	3	-	600

S20 series (Figure 4.1) are used for contact mode, and RTESP7 series are used for tapping mode imaging. The specifications of the scanning probes are available in Table 4.1. In DNP-S20 series, four cantilevers are mounted on the chip, two of them are 120 μm long, and the other two are 205 μm in length. Each of the cantilevers are either $wide - legged$, or $thin - legged$.

The cantilever deflection results in a change in the position of laser beam reflected from the back side of the cantilever onto a photodiode detector. In both contact and tapping mode, a topographical map is created by recording the motion of the piezoelectric tube required to keep the deflection or oscillation amplitude constant. All the post-processing operations are performed using the Nanoscope^{TM} IIIa imaging software Version: 5.12b36 (Digital Instruments, USA).

In order to experimentally analyze the change in interaction energy induced by the morphological properties of the surface, five different substrates, having different set of topographical parameters, were used. Figure 4.2 and Figure 4.3 show the 2D and 3D AFM images of these five different substrates, respectively. All of the substrates are made from silicon wafers. The $nanopost - low$, and $nanopost - mid$ substrates shown in Figures 4.2a and 4.2b were kindly provided by Dr. CJ. Kim's group at University of California, Los Angeles *et al.* [Choi et al., 2007]. The substrates in Figures 4.2c to 4.2e are standard substrates, which are originally used as calibration grids in AFM scanning, and are manufactured by Veeco Digital Instruments (Santa Barbara, CA, USA) (Figure 4.2c), and NT-MDT Integrated Solutions for Nanotechnology (Moscow, Russia) (Figures 4.2d, 4.2e). Exact geometrical information of the substrates shown in Figures 4.2, and 4.3 are listed in Table 4.2. These parameters are reported by manufacturers. The images of $nanopost - low$, and $nanopost - mid$ substrates [Figures 4.2(a) and (b)] are obtained employing tapping mode technique, whereas the rest of the images are obtained by performing contact mode technique. The scanning resolution in all of the images is set to 512 by 512 pixels. This is the maximum possible lateral X and Y resolution in Veeco Digital Instrument AFM.

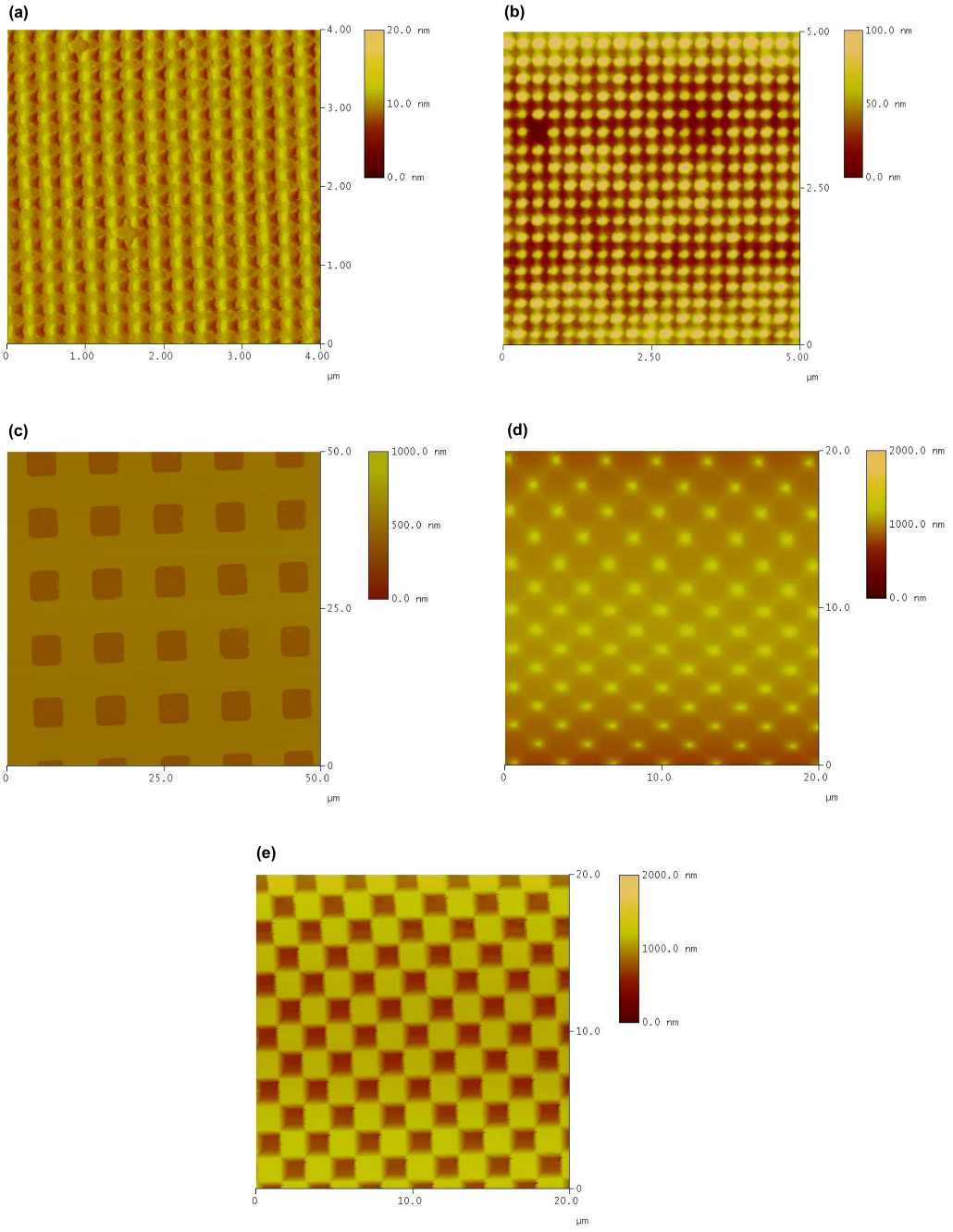

Figure 4.2: 2D AFM images of **(a)** *nanopost − low*, **(b)** *nanopost − mid*, **(c)** DI standard, **(d)** TGT01, and **(e)** TGX01 substrates in air using RTESP7 (a,b), and DNP-S20 (c-e) probes. The scan size is different in each sample.

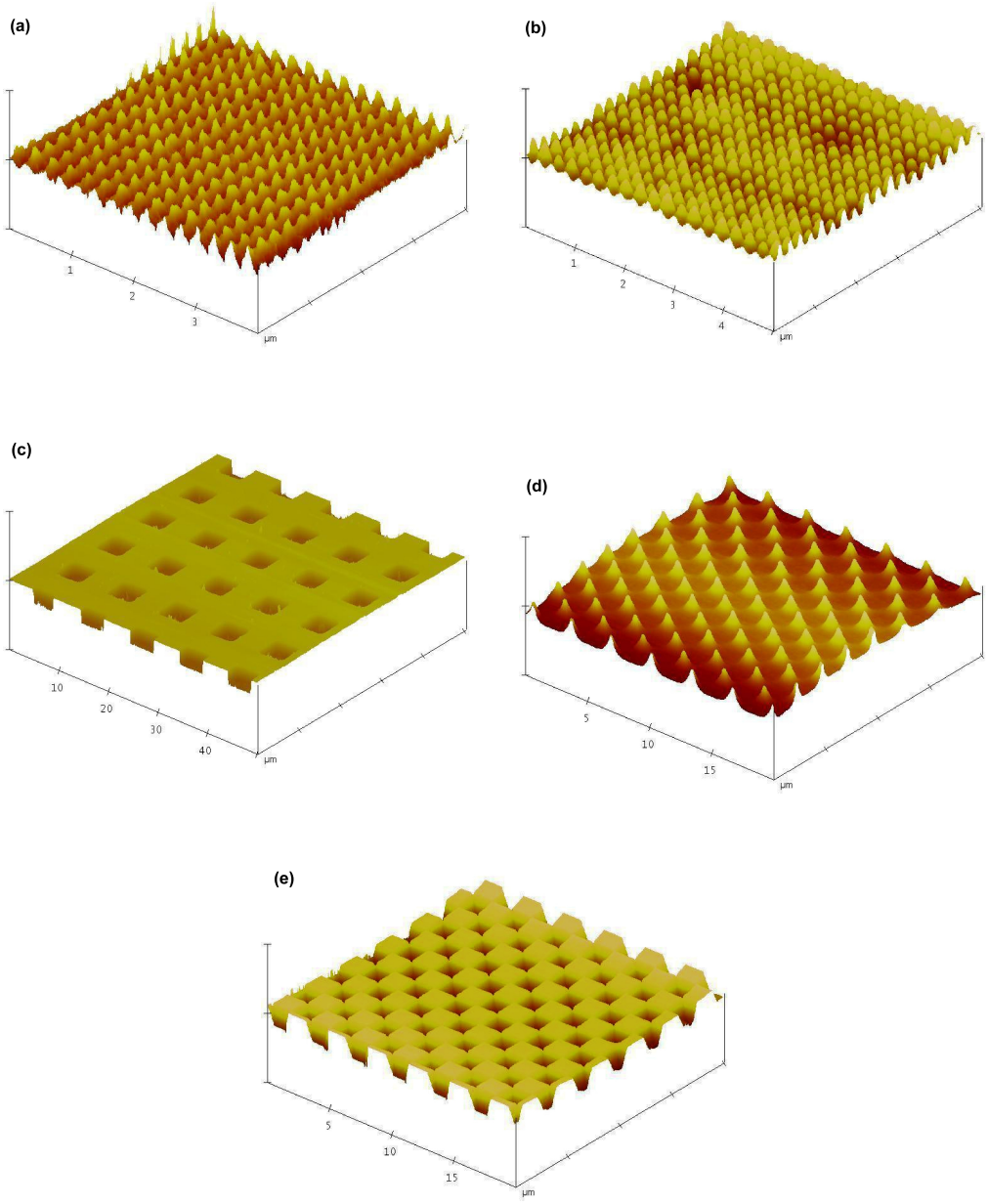

Figure 4.3: 3D AFM images of **(a)** *nanopost − low*, **(b)** *nanopost − mid*, **(c)** DI standard, **(d)** TGT01, and **(e)** TGX01 substrates in air using RTESP7 (a,b), and DNP-S20 (c-e) probes. Data scales (Z values) are identical to the Z bars shown individually for each sample in Figure 4.2.

The original shape of the asperities in *nanopost* substrates are stated by Choi *et al.* [Choi et al., 2007] to be sharpened bearing needle or blade-like shape at their peak. However, as it is observed in Figures 4.2(a) and (b), the asperities have curved heads. This distortion in the images is due to similarity between the size of the probe tip, the asperities height and their peak radii [Kitching et al., 1999]. This distortion is known as tip convolution effect. In fact, since the asperities peak radius is relatively in the range of the probe tip radius (*i.e.*, 15-20 nm), and on the other hand, the lateral resolution in AFM scanning is limited (*e.g.*, 512 by 512 pixels), the probe is not capable of detecting the peak point of the asperities. However, as the asperity size grows, and the pitch distance increases, keeping the same pointed end structure in the asperities peak as in Figure 4.2d, AFM provides a highly accurate information about the peak of the samples. As depicted in table 4.2, the size of the asperities in $nanopost - low$ is between 10 to 20 nm, while the probe tip radius is almost 20 nm. For $nanopost - mid$ substrate, one may employ Eqn. (3.47) (chapter 3) to find the maximum probe radius a_p, which allows the probe to reach the bottom flat surface of the substrate. Assuming the average asperity radius to be 150 nm, and pitch distance equal to 230 nm in $nanopost - mid$ sample, the largest spherical probe which meets the above criteria has to have a radius of 13.68 nm, that is smaller than the DNP probe tip radius. Moreover, the calculation denoted in Eqn. (3.47) refers to a spherical probe, while the DNP probes have a pyramidal structure with an average wall angle of 70 degrees as depicted in SEM images shown in Figure 4.1. According to the geometrical information provided in Table 4.2, and the DNP probe tip radius a_p =15 to 20 nm, the inequality in Eqn. (3.47) holds for all of the rough samples used in this study, except the $nanopost - mid$ substrate. Scan rate which defines the probe lateral velocity along X and Y direction is also another parameter that may affect the image quality, specially for surfaces with low amplitude asperities. In Figures 4.2 and 4.3, the scanning sizes for different sample substrates are selected based on their geometrical parameters, such that their heterogeneities become more visible.

In order to compare the force analysis results obtained for the introduced rough heterogeneous surfaces with the observations over a smooth surface, one may consider a glass or mica sheet to be replaced as smooth flat plate. In this study, a cleaned glass slide was chosen to represent the smooth flat plate, where its Rms (R_q)was calculated to be less than 0.3 nm.

4.2.2 Roughness and Section Analysis

Table 4.3: Mathematical description of roughness statistical parameters.

Parameter	**Calculation**
Z_{mean}	$\frac{1}{n}\sum_{i=1}^{n} Z_i$ where n = data points, Z = height deviation
Rms (R_q)	$\sqrt{\frac{1}{n}\sum_{i=1}^{n}(Z_i - Z_{mean})^2}$
R_a	$\frac{1}{n}\sum_{i=1}^{n}\lvert Z_i - Z_{mean}\rvert$
R_p, R_v	Measured
R_{max}	$R_p + R_v$
Surface Area Difference	$\left[\frac{\sum(\text{surface area})}{\sum(\text{projected area})} - 1\right] \times 100\%$

To quantitatively assess the roughness of the sample surfaces, a roughness analysis is conducted for the AFM images using the Nanoscope^{TM} IIIa software. In this section, the statistical parameters used in this analysis are defined, and their values are evaluated for five samples introduced in section 4.2.1. These parameters are defined as follows: Z_{mean} is the average of all Z values within a closed area; R_q is the standard deviation of the Z values; R_a is the average of the absolute Z values; R_p, R_v are the maximum peak and valley depths respectively. In other words, R_p, R_q indicate distances from the

Table 4.4: Geometrical Parameters of Rough Substrates

	nanopost-low	**nanopost-mid**	**DI standard**	**TGT01**	**TGX01**
$Z_{mean}nm$	0.016	-0.30	0.78	1.051	-6.06
Rms (R_q) nm	1.534	22.59	78.96	99.97	203.62
R_a nm	1.18	18.42	65.71	75.89	178.34
R_p nm	9.17	81.23	149.30	478.12	363.72
R_v nm	-5.21	-45.28	-322.01	-241.50	-573.24
R_{max} nm	14.389	126.51	471.31	719.62	936.96
SAD %	0.275	16.52	1.58	4.32	25.78

mean plane to the highest/lowest point in the evaluation area. R_{max} is the maximum vertical distance between the highest and lowest point in the data. The last parameter is surface area difference (SAD) in percentage, which is defined as the ratio of the sum of surface area minus sum of projected area to the sum of projected area. Here, surface area is the 3D surface obtained by the sum of the triangles formed by three adjacent points, and the projected area is the 2D surface produced by projecting the surface onto the threshold plane.

The mathematical description of these parameters are listed in Table 4.3, and their values are calculated for each sample substrate in Table 4.4. In addition, a section analysis, as shown in Figure 4.4, provides the cross-sectional view of the surfaces. Since the samples surfaces are periodic in terms of the asperity size and their arrangement, the cross sectional views across the line shown in Figure 4.4 for individual substrates can reasonably represent the roughness of the corresponding surface along different pathes. This figure clearly illustrates whether the probe has reached the bottom surface as discussed in section 4.2.1. One may also observe the tip convolution effect in parts **(a)** and **(b)** of the same figure. This is most likely due to very small pitch distance in $nano - post$ substrates, and the fact that the size of the AFM tip and the asperities amplitude are relatively the same.

4.3 AFM Force Profile and Data Analysis

4.3.1 AFM Force Measurement Operation

In AFM force measurement, one of the 4 cantilevers mounted on DNP-S20 probe is used depending on the range of interaction force, and the stiffness required for that range. During force measurement experiment, the probe is repeatedly brought into contact and then retracted away from the surface. In AFM force measurement, despite to AFM imaging, the movement of probe is only in Z direction, and the lateral movement of the piezo-electric tube on which the probe is mounted, is switched off. The schematic in Figure 4.5

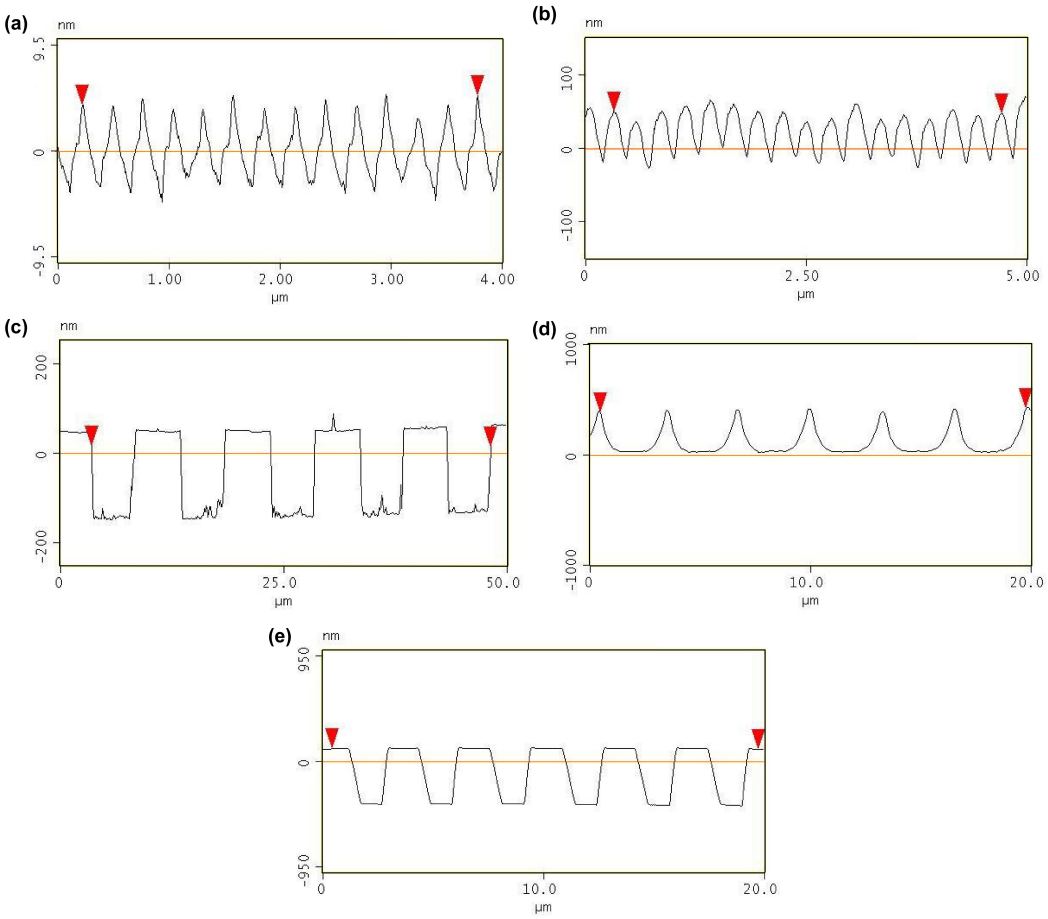

Figure 4.4: Cross section analysis showing the cross-sectional view of the sample rough substrates. **(a)** $nanopost - low$, **(b)** $nanopost - mid$, **(c)** DI standard, **(d)** TGT01, and **(e)** TGX01.

illustrates the cyclic steps and configuration of the probe as it approaches, and moves away from, the surface.

At far distances, the probe and surface have no interaction to each other, therefore the cantilever does not sense any force, hence no deflection occurs as it can be observed in step **(I)**. At closer distance, hydrodynamic and electrostatic interaction repulsions cause an upward (positive) deflection in the cantilever as shown in step **(II)**; However, this repulsive force strongly depends on the magnitude of the electrostatic force, and in many cases when this force is negligible, the cantilever bending is barely observed in this step. An increasing attractive force, due to van der Waals interaction energy, between the probe and the surface, which causes a downward (negative) deflection in the cantilever is observed as the probe is brought closer. This has been depicted in part **(III)**. As the probe tip contacts the surface, provided that the probe and surface do not indent, a positive bending initiates in the cantilever, which increases linearly as a function of the cantilever vertical position. It implies that as the piezo-electric tube is moved downward over a certain distance, the cantilever end is moved upward over the same distance (see parts **(VI)** and **(V)**). This part of the experiment is called *constant compliance region*.

In the second half of the force measurement cycle, the piezo-electric tube movement is reversed, and it starts retracing back to its initial position. However, due to an adhesion force between the probe and the surface, the probe tip sticks to the surface and cause negative deflection in the cantilever, until the bending provides the required force to detach the AFM tip from the surface. This force is called $pull - off$ force (see steps **VI** and **VII**). As soon as a force equivalent to the $pull - off$ force is exerted to the tip, the cantilever abruptly bounces back. With further separation distance, the cantilever does not experience any force, and it leads to a zero degree deflection as can be observed in parts **VIII-IX**. Total vertical range of trace-retrace cycle is manually adjustable, and is defined as $ramp - size$. The maximum $ramp - size$ in Digital Instruments AFM is 5557 nm. The scan rate at which the vertical velocity of probe is defined in traction and retraction intervals can also be adjusted.

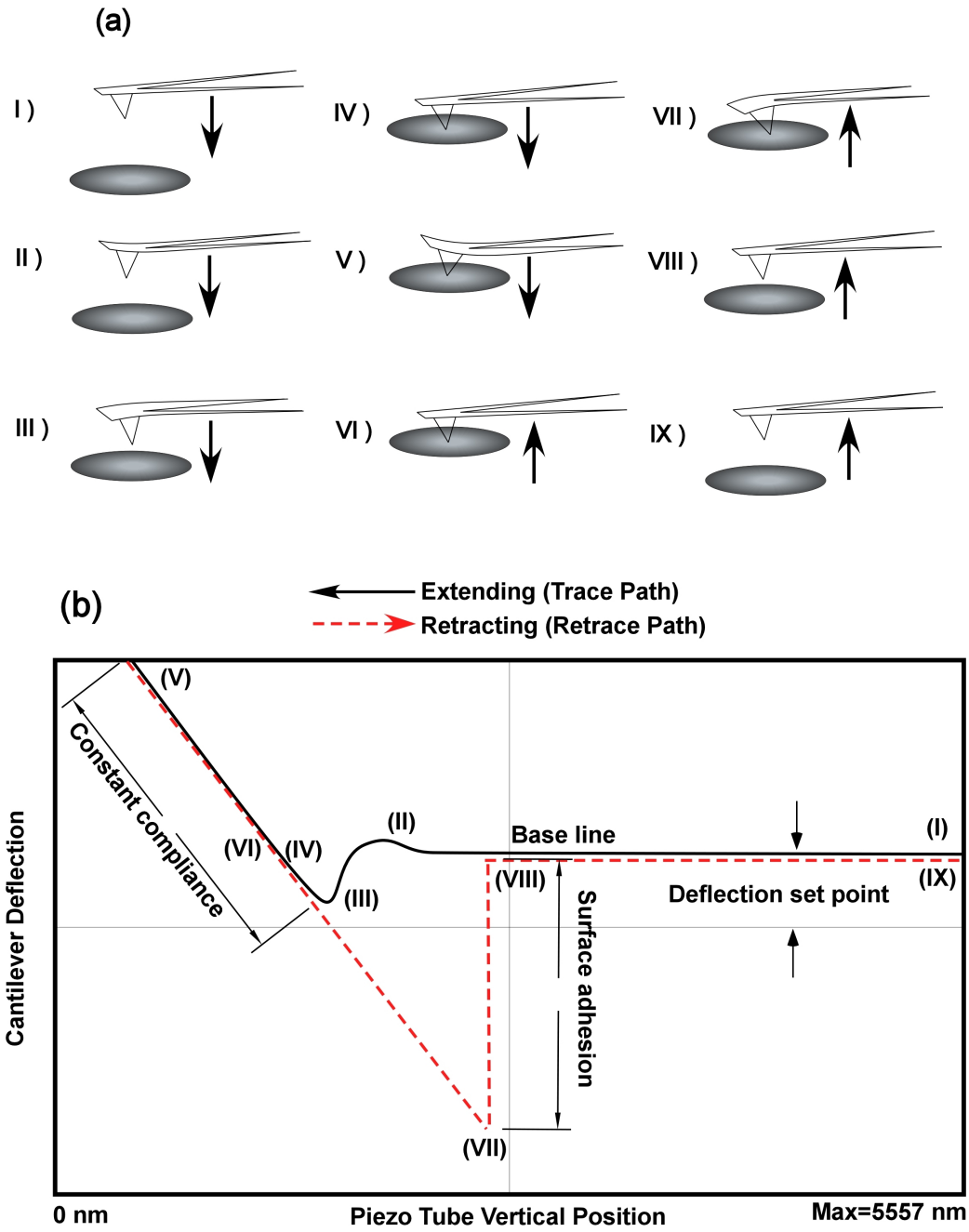

Figure 4.5: **(a):** Schematic depiction of AFM probe cantilever configuration during force measurement.**(b):** A sample force profile, depicting the cantilever deflection versus the piezo-electric tube vertical position. The steps **(I)** through **(IX)** of the trace-retrace cycle are labeled on the graph.

4.3.2 Experimental Procedure

In this study, the long $thin - legged$ cantilever with spring constant of $k = 0.06$ N/m (Bruker AFM Probes Corporation Website) was selected. Its sensitivity to external forces is highest among the four cantilevers. In order to account for electrostatic interaction energy, all of the experiments were conducted under a aqueous medium. In this study, Milli-Q deionized water and potassium chloride KCl (1:1) were used as electrolyte solution. The ionic concentration values of KCl solution, selected for force measurement experiments, were 0.1, 1, 10, and 100 mM respectively. The reason of such a selection is to experimentally illustrate the correlation of increasing or decreasing the Debye screening length κ^{-1}, with the magnitude of DLVO energy. Besides, the AFM sensitivity can be investigated by observing how precisely the AFM can distinguish the magnitude of the interaction forces for electrolyte solutions with different molarities.

The DNP-S20 probe was cleaned by being submerged in acetone for 10 minutes before the experiment. The probe was then drowned in deionized (Milli-Q) water for a couple of minutes. This process was repeated for the second time, to ensure that the dirts were removed, however this time for a shorter period. Similar cleaning must be done for the cantilever holder (when the experiments are performed under liquid). The cleaned probe and the cantilever holder were then dried very gently by nitrogen gas. It is very essential to completely dry these two components before they are used in a force measurement experiment. This is to prevent two problems as follows: Firstly, any remaining moisture may cause the generation of bulb between the probe and the cantilever holder, hence a huge error in force measurements. Secondly, since the cantilever holder is placed on the piezo-tube by inserting its four metallic needles to the grooves on the cantilever holder, and that the needles may carry electricity (not for regular force measurement tests), any remaining moisture in the groove may damage the AFM and cause a short circuit. It is also necessary to clean the probe and its holder when the

intervening medium with higher molarity is replaced with the lower molarity solutions. The substrates were also cleaned by putting a drop of acetone, and then a layer of replicating tape on top of the surface for almost 30 seconds. The tape was removed afterward.

During the force measurement, since the experiments are conducted under liquid medium, as it was mentioned earlier in this section, and owing to the fact that the long $thin - legged$ cantilever is used ($i.e.$, $k = 0.06$ N/m), meaning that it is highly flexible, the scan rate must be adjusted to a very low value. This is to reduce the effect of hydrodynamic forces [Valle-Delgado et al., 2005], and unnecessary bending of cantilever imposed by the fluid drag forces. To this end, the scan rate was set to 0.1 Hz. The ramp size was set between 1.5 to 2 μm, meaning that the vertical velocity of the probe was between 300 to 400 nm/s. The final force measurement for each sample took almost 5 minutes, excluding the time required for cleaning and AFM pre-processing settings.

Nanoscope^{TM} IIIa postprocessing software then provided a force profile which represented the cantilever deflection versus the piezo-electric tube vertical position. A sample regenerated force profile is depicted in Figure 4.5b. The steps **(I)** through **(IX)**, described in the section 4.3.1, are labeled on the plot. The force plot is obtained by collecting 16 to 64000 sample in Z direction, or on the other word, the piezo-electric tube vertical position ($i.e.$, the horizontal axis in Figure 4.5b). Additionally, each plot represents the average values of 1 to 1024 trace-retrace cycle. These parameters can be adjusted manually. For the experiments in the present study, each test was the average of 25 trace-retrace cycle, where the force plots included 10240 data points. The deflection versus piezo-electric tube position raw date need to be converted to the force versus actual separation distance, allowing one to conduct the force analysis. To obtain the force-separation curve, the *base line* illustrated in Figure 4.5b must be corrected by deducting the constant value of deflection set point from the raw data. Following to this, the *constant compliance region* must be removed from the force-plot data. This region starts when the cantilever deflection (Y axis) varies linearly with respect to the piezo-tube position (X axis).

As explained earlier, this is due to the constant contact of the AFM tip with the surface. Once the *base line* is corrected, and the *constant compliance region* is removed, the magnitude of cantilever deflections must be multiplied by its spring constant to obtain the actual force-separation distance curve. In these curves, positive forces are associated with repulsion, whereas negative forces indicate attraction between the AFM tip and the surface. The force measurement results obtained for sample rough substrates introduced in section 4.2.1 are discussed in chapter 5.

4.4 Hamaker Constant and JKR Adhesion Theory

As described earlier in section 4.3, in the retraction cycle of AFM force measurement a negative (downward) deflection occurs in the cantilever due to an adhesion force existing between the probe and the surface. The force required to detach the cantilever from the surface are called $pull-off$ force. Johnson-Kendall-Roberts (JKR) theory [Johnson et al., 1971] states that the adhesion force between two incompressible bodies is related to their work of adhesion by the following relation.

$$F = 2\pi \left(\frac{R_1 R_2}{R_1 + R_2} \right) W_{12} \tag{4.1}$$

where R_1, and R_2 are the radius of curvature of the interacting bodies, and $W_{12} = 2\gamma$ is the adhesion work (surface energy per unit area) in their between, when γ is the surface tension energy. However, real particles are not realistically incompressible, and they will deform when they come into contact with each other due to influence of attractive forces. As a result, under an external force F, a finite contact area of radius a will form at the interface of the two bodies. According to JKR theory this radius is given by:

$$a^3 = \frac{R}{K}[F + 3\pi R W_{12} + \sqrt{6\pi R W_{12} F + (3\pi R W_{12})^2}] \tag{4.2}$$

Here, $R = R_1R_2/(R_1 + R_2)$, where for a sphere of radius R_1 and a flat surface ($R_2 = \infty$), having the same material with elastic moduli K, under zero external force the contact area radius will be:

$$a_0 = (6\pi R^2 W_{12}/K)^{1/3} = (12\pi R^2\gamma)^{1/3} \tag{4.3}$$

Equation 4.2 further explains that the surfaces will separate under a negative (opposite to the direction of adhesion) force F_s of:

$$F_s = -3\pi R\gamma \tag{4.4}$$

and the contact area radius a_s at the separation time will be:

$$a_s = (3\pi R^2\gamma)^{1/3} = 0.63a_0 \tag{4.5}$$

Giving the fact that the adhesion work $W_{12} = 2\gamma$ is equal to the attractive potential energy per unit area between the surfaces, and assuming that the van der Waals energy U_{VDW} is the only potential accounting as the interfacial interaction energy, one may calculate the Hamaker constant A_H by employing Eqns. (4.2) and (4.4). According to Hamaker approach the van der Waals interaction energy per unit area between a sphere of radius R_1 and a flat plate separated by a distance of h_0 is:

$$U_{VDW} = -\frac{A_H}{6}\left[\frac{R_1}{h_0} + \frac{R_1}{R_1 + 2h_0} + \ln(\frac{h_0}{h_0 + 2R_1})\right] \tag{4.6}$$

Therefore, the expression for van der Waals force per unit area is simply calculated as:

$$F_{VDW} = \frac{dU_{VDW}}{dh_0} = -\frac{A_H}{6}\left[\frac{R_1}{h_0^2} + \frac{R_1}{(h_0 + 2R_1)^2} + \frac{1}{h_0 + 2R_1} - \frac{1}{h_0}\right] \tag{4.7}$$

Replacing the expression $U_{VDW} = W_{12} = 2\gamma$ and Eqn. (4.4) [absolute value] into the Eqn. (4.6), and rearranging it for Hamaker constant A_H, one may obtain:

$$A_H = \frac{4F_s/\pi R_1}{\left[\frac{R_1}{h_0} + \frac{R_1}{R_1+2h_0} + \ln(\frac{h_0}{h_0+2R_1})\right]} \tag{4.8}$$

In Eqn. 4.8, F_s is the only unknown which can be obtained from AFM force measurements. As described earlier in section 4.3, the $pull - off$ force in AFM force profile is calculated by multiplying the magnitude of the maximum negative deflection observed in cantilever due to adhesion (see step **(VII)** in Figure 4.5b) by the spring constant k. It is pertinent to highlight that the JKR analysis is valid only for spherical particles adhering on flat surfaces, while the AFM probe is not exactly in a spherical shape, hence the above analysis can only provide an approximation for A_H values in AFM experiments.

4.5 Summary

In this chapter, the experimental procedure and analysis using the atomic force microscopy (AFM) technique is introduced. This technique was employed in this research to determine and characterize the forces between two interacting surfaces. The concepts in this chapter provide essential information about the physics of the AFM measurements, including AFM topography analysis and AFM force measurement, and their relation to the surface roughness and force analysis. The set-up and the required materials for these analyses are reported. The experimental observations based on AFM force measurement are presented and discussed in the next chapter.

Chapter 5

Results and Discussion

5.1 Introduction

In this chapter, the experimental force measurements achieved using a Veeco Digital Instrument AFM and by employing a DNP-S20 long $thin-legged$ sharp tip are presented in section 5.2. Based on these results, the accuracy and precision of the AFM force measurement are assessed, and the colloidal interactions are investigated over five model rough substrates. Following this, the results of the analytical derivations presented in section 3.3 of chapter 3 are presented in section 5.3. These analytical expressions reveal and characterize the influence of surface roughness on the DLVO energy components without invoking any numerical computation. It is discussed that how different shapes of the model asperities attenuate the overall interaction energy, and how this reduction correlates with the geometrical parameters of the modeled asperities. However, these results correspond to the interfacial interactions per unit area between a flat and a rough surface. Next, results of the numerical analysis developed to replace the flat plat with a spherical probe are presented. The numerical simulations are employed to demonstrate how the energies between the probe and a rough surface vary with the location of the probe over the surface. Thereafter, in order to enhance the precision of the interaction energy versus separation distance numerical simulations, different approaches for modeling the exact shape of an AFM sharp tip are evaluated numerically.

5.2 Experimental Observations

5.2.1 Experimental Force Measurement over Glass

The experimental force measurement results obtained using AFM over glass substrates are presented in this section. As explained in Chapter 4, the intervening electrolyte solutions are 0.1, 1, 10, or 100 mM KCl solutions. The forces obtained experimentally on a smooth glass substrate are compared against the corresponding values of calculated interactions based on DLVO theory. To more precisely consider the DNP-S20 tip real geometry, and hence more accurately predict the interaction energy between the tip and glass theoretically, a model probe as shown in Figure 3.6a is used to calculate the DLVO energy. The details of this calculation was provided in section 3.6 of Chapter 3.

In the following, the force versus separation distance plots obtained by conducting AFM force measurement, using DNP-S20 probe, are presented. These results are provided in Figure 5.1 and 5.2.

Figure 5.1a illustrates the variation of the experimentally obtained forces in nano-Newton with respect to the separation distance between the closest point of the DNP-S20 tip and the surface. In this test, the concentration of the electrolyte solution is 0.1 mM. It is observed that the maximum magnitude of force sensed by AFM at the separation distance of less than 5 nm, 0.21 nN, is reasonably close to DLVO force at this location, 0.24 nN. The attenuation in experimental forces, however, are more pronounced between 5 to 40 nm, where both the DLVO curve and experimental forces decrease to almost 0 nN at separation distance of 100 nm.

Figure 5.1b depicts the experimental forces obtained under a 1 mM KCl solution. In this graph, the maximum force observed in experimental measurement is 0.11 nN at separation distance of 4 nm, whereas the maximum force in DLVO curve is 0.07 nN at a distance of 2 nm from the surface. In comparison with the experimental results for 0.1 mM solution, in Figure 5.1a, the general trend of the AFM result in Figure 5.1b is correct, since it shows that by increasing the ionic concentration, the Debye length κ^{-1} and the maximum

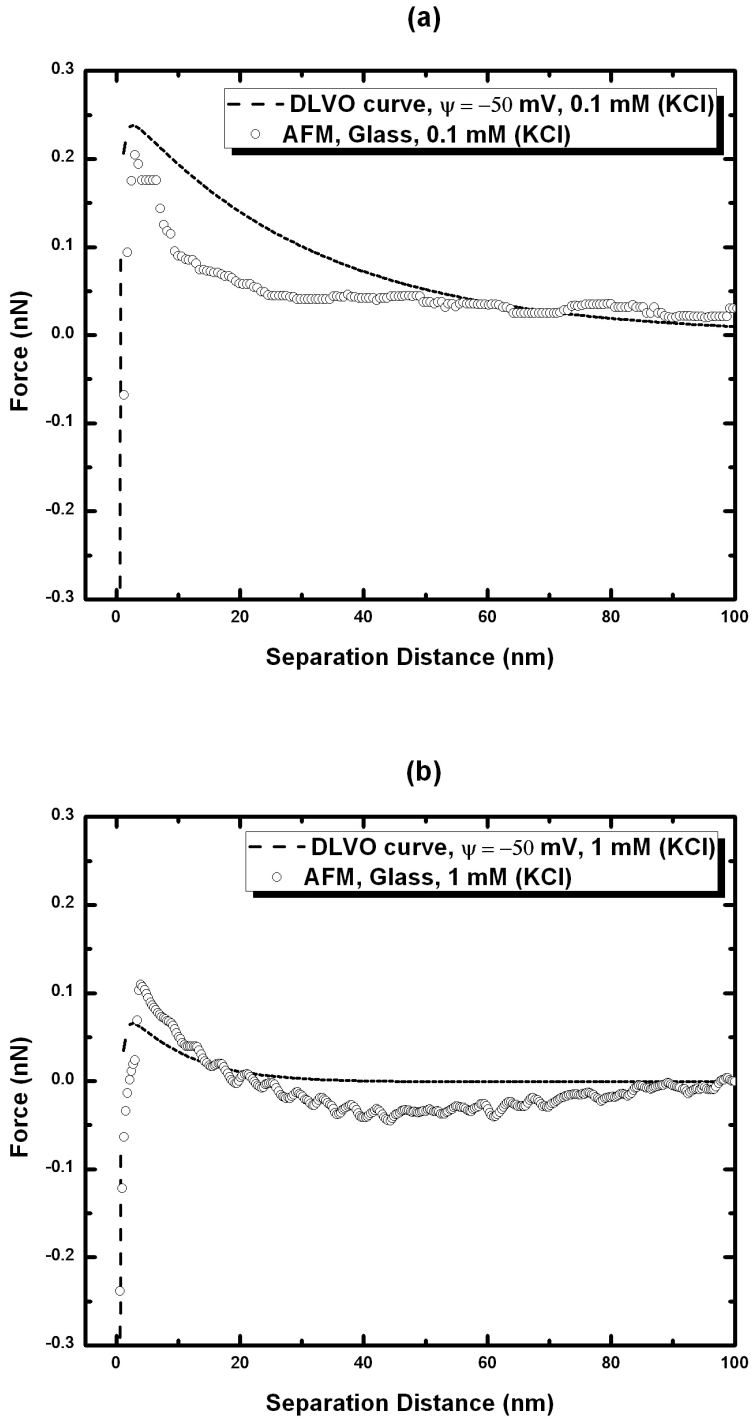

Figure 5.1: AFM force measurement results for DNP-S20 probe over glass under:**(a)** 0.1 mM KCl, and **(b)** 1 mM KCl. The results are compared against an analytically derived DLVO interaction force.

interaction force decrease. However, by comparing the results in Figure 5.1, it is seen that for higher ionic concentrations, the measurement error increases, or on the other word, AFM sensitivity decreases. As one possibility, this can be ascribed to the effect of hydration forces which are reported to be more significant in higher electrolyte concentrations [Butt, 1991, de Souza et al., 2001, Valle-Delgado et al., 2005]. In a range between 20 to 80 nm the experimental forces suggest that the probe is experiencing a negative (attractive) force with a maximum value of -0.04 nN, and it implies that in this range, there is an attraction between the probe and the surface. This is not true according to the DLVO force curve. However, both the experimental and DLVO force curves converge to 0 nN at the separation distance of 100 nm.

The results provided in Figure 5.2a and b correspond to force measurements under 10 and 100 mM KCl electrolyte solution. As shown in the DLVO curves associated to each plot in Figure 5.2, following the same trend as in Figure 5.1, the Debye length has decreased by increasing the salt concentration, and lesser forces are exerted to AFM probe. The AFM force measurement for 10 mM solution (Figure 5.2a) matched with the DLVO curve for this concentration. However, the forces obtained under 100 mM salt concentration, deviate from the DLVO interaction energy at separations smaller than 3 nm. In fact, the Debye length (2 nm) is extremely short in 100 mM ionic concentration in comparison with other lower concentrations. Therefore, as seen in the DLVO curve (dashed line in Figure 5.2b), the interacting bodies, having almost no interaction at far distances, experience an abrupt repulsive force only at the closest few nanometers (*i.e.*, 1 to 3 nm) separation distance with almost the same amplitude as for 10 mM concentration results (Figure 5.2a). This leads to a large gradient in the curve at this range. On the other hand, the larger attractive force, resulting from van der Waals interaction, that becomes more dominant at closer distances, has been detected accurately by AFM for both the 10 and 100 mM salt concentrations.

In Figure 5.3, a quantitative comparison can be made between all the force distance plots, in order to assess the influence of the ionic concentration on

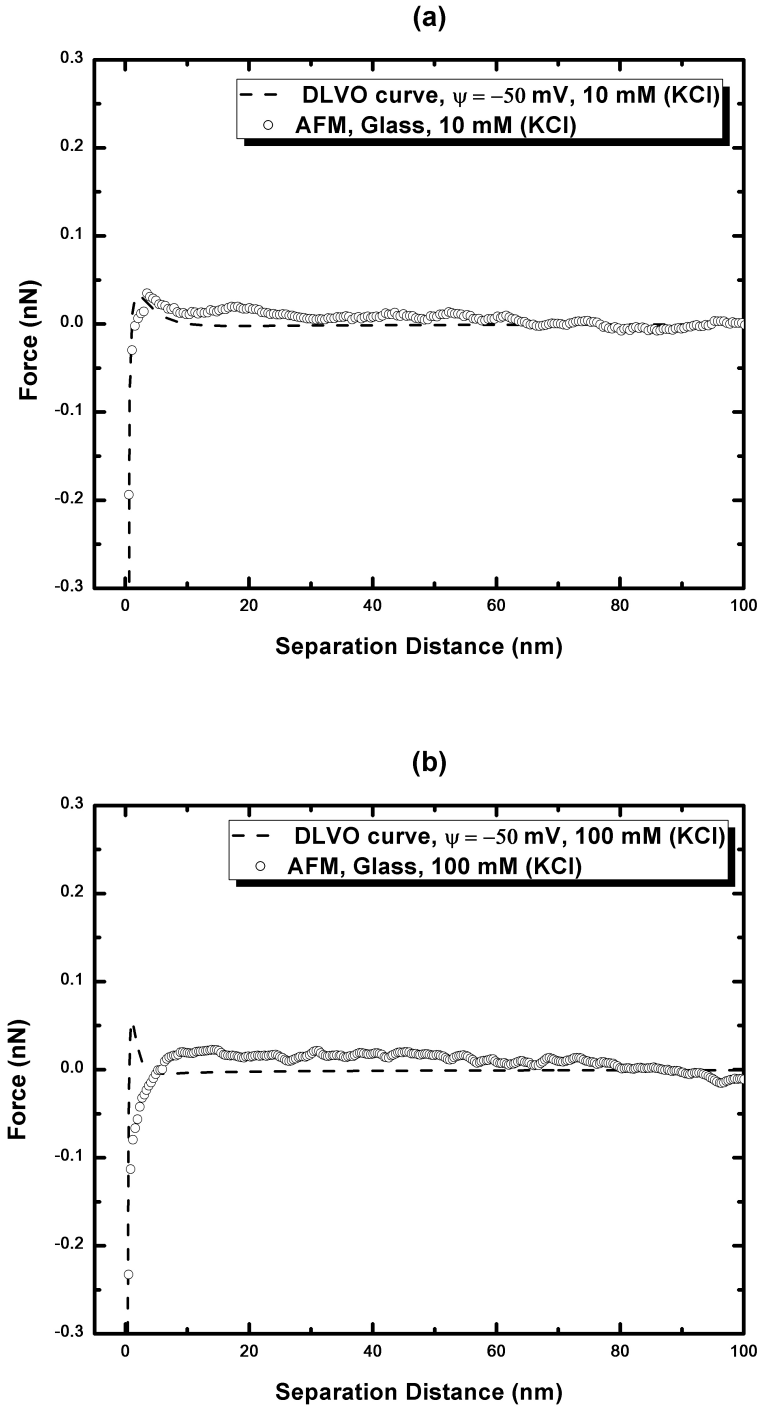

Figure 5.2: AFM force measurement results for DNP-S20 probe over glass under:**(a)** 10 mM KCl, and **(b)** 100 mM KCl. The results are compared against analytically derived DLVO interaction force.

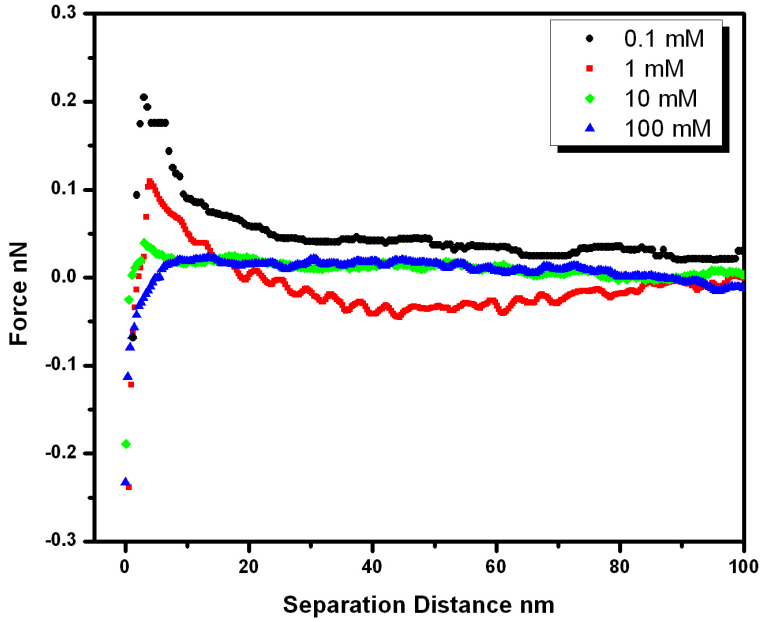

Figure 5.3: Comparison of AFM force measurement results for DNP-S20 probe over glass under 0.1, 1, 10, and 100 mM KCl.

the colloidal interactions between the DNP-S20 probe and a smooth surface. As discussed earlier, by increasing the molarity of the electrolyte solution, the Debye screening length decreases, and so does the maximum value of the repulsive force. This trend matches with DLVO theory, and is also clearly illustrated in the experimental measurements, in that the black symbols have the highest maximum followed by red, green and blue symbols, which represent the results corresponding to 0.1, 1, 10 and 100 mM KCl solutions. Besides, in all of the experiments, the forces have attenuated to almost zero at far separation distances.

The experimental observations of this study on glass using a Veeco Digital Instrument AFM, agreed with other investigations [Butt, 1991,de Souza et al., 2001] with nearly similar testing conditions. However, in some other studies [Kappl and Butt, 2002,Valle-Delgado et al., 2005,Zhao, 2009] where a colloidal probe was employed rather than the original sharp tip, the interactions are reported to be practically 10 times larger.

5.2.2 Effect of Surface Roughness on AFM Force Measurement

So far, the interaction forces have been investigated on a glass slide, representing an ideally smooth flat surface. However, in this research the effect of surface physical heterogeneities on the interaction forces are of interest. To this end, the five rough substrates introduced in chapter 4 are used to compare and contrast the experimentally obtained force plots with the previous results for a smooth flat surface. For these experiments, 0.1 mM KCl solution was selected as the electrolyte solution. Other researchers [Bowen and Doneva, 2000] have attempted to conduct the force analysis over rough surface by implementing the colloidal probe technique. In their experiments, they addressed the influence of roughness on electric double layer interactions, and quantitatively discussed the effect of surface peaks and valleys on these interaction. However, as mentioned before, using colloidal probe technique, one will not be able to characterize short-range interactions. Also, the geometrical parameters (*e.g.*, edge radius, pitch, or height) of the asperities in some of the samples used in the current research are in nano- scale, while a large colloidal particle fails to detect their topography. So, for the force measurement over rough surfaces, similar to the measurements over glass, the long $thin - legged$ sharp tip of the Veeco DNP-S20 probe was used.

Figure 5.4 depicts the force versus separation distance results for $nanopost - low$, and $nanopost - mid$ substrates. In both plots the experimental results (symbols) are compared against the theoretical DLVO interaction energy between a conical probe and its spherical tip with a smooth flat plate as in Figure 5.1a. It is clearly illustrated in Figure 5.4a, that the roughness of the surface has reduced the interaction forces exerted on the AFM probe. Additionally, these forces diminish faster in comparison with those on a glass substrate (Figure 5.1a). Figure 5.4b, shows the forces between the probe and $nanopost - mid$ substrate under similar condition. As seen in this plot, the roughness has reduced the amount of the interaction forces. As described in Table 4.2 in Chapter 3, the asperity size on $nanopost - low$ substrate are 10-20

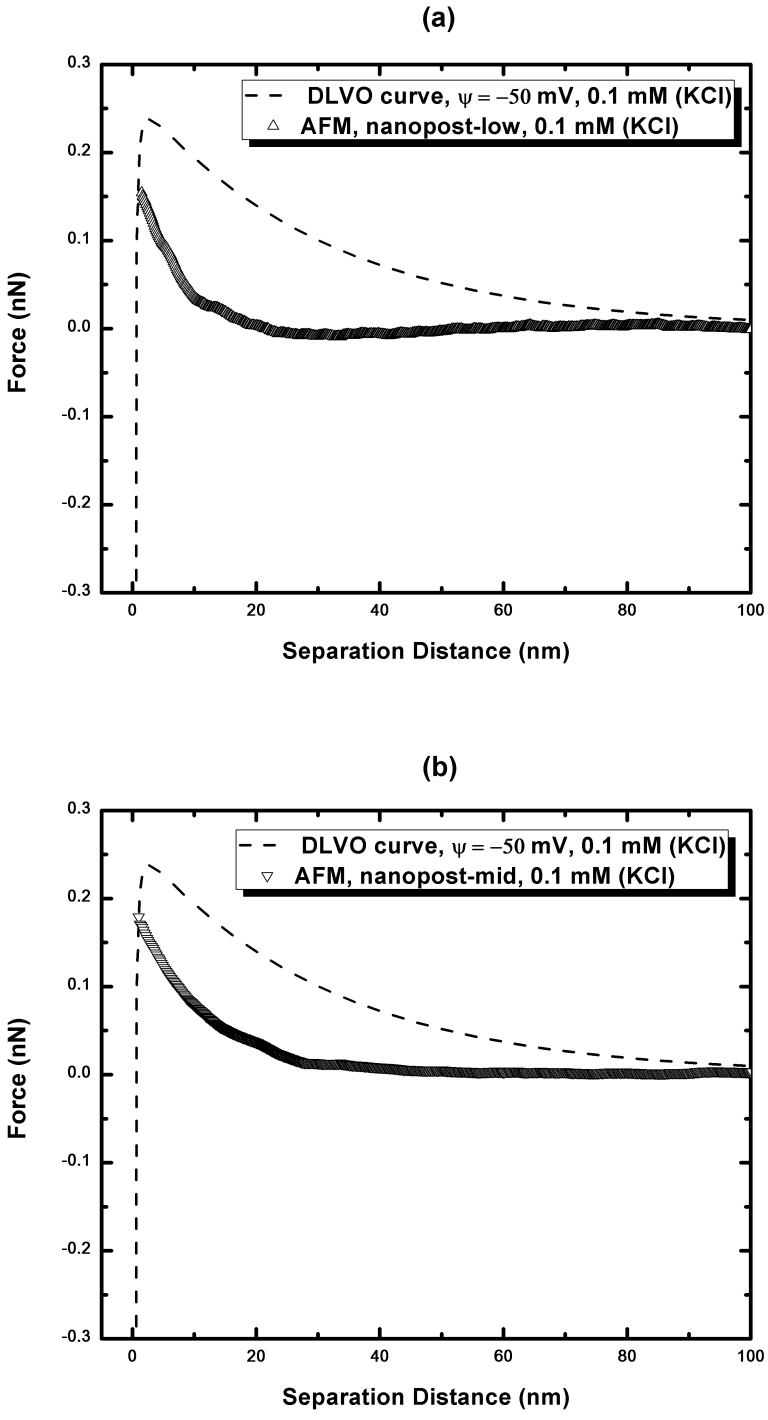

Figure 5.4: AFM force measurement results for DNP-S20 probe over: **(a)** *nanopost − low*, and **(b)** *nanopost − mid* under 0.1 mM KCl. The results are compared against analytically derived DLVO interaction force.

nm, while on *nanopost − mid* substrate, it is 100-200 nm, where the DNP-S20 hemispherical tip radius is 20 nm in average. The pitch distance on both substrates is 230 nm. Therefore, the effect of surface roughness on the colloidal forces are observed to be higher for smaller size asperities.

Generally, this behavior agrees with other numerical studies [Huang et al., 2010], where increasing the scaled radius of a spherical probe (probe radius divided by the asperity radius) leads to smaller interaction energy. From another point of view, this behavior can be explained in the context of physical constraints, and considering the geometry of DNP-S20 probe as a pyramid. In this regard, one may invoke the effect of probe wall angle, and that the larger asperities lead to more interaction with the inclined wall of the DNP-S20 pyramidal probe. So, the larger asperities of the *nanopost −mid* substrate cause less reduction in the interaction force.

coupled with the knowledge of the colloidal interactions variation with respect to the separation distance between the bodies,

Figure 5.5 presents the experimental results obtained for *DI − standard*, and *TGT01* substrates. As seen in both plots of this figure, despite to the *nanopost* substrates, the surface roughness of these two substrates had less influence on the interaction forces at closer separation distances. However, by accounting the geometrical relation of the probe and the substrates, these results can be explained. In both the *DI − standard*, and *TGT01*, the pitch distance (*i.e.*, 3 μm) is much larger than the radius of the DNP probe hemispherical tip (*i.e.*, 20 nm). Considering the size of upper pyramidal part of the probe that is almost 6 μm in height, and 4 $\mu m \times 4$ μm in base, it can be concluded that the probe is interacting with a smooth surface, rather than a rough surface, if the hemispherical tip is located at a location between the two adjacent asperities. Thus, if the pitch distance is considerably larger than the tip radius, one may observe that surface roughness will not cause a significant reduction in the interaction energy. However, it is reasonable to see that the reduction in energy/force become more pronounced, when the probe is located closer to peaks or valleys edges of the asperities.

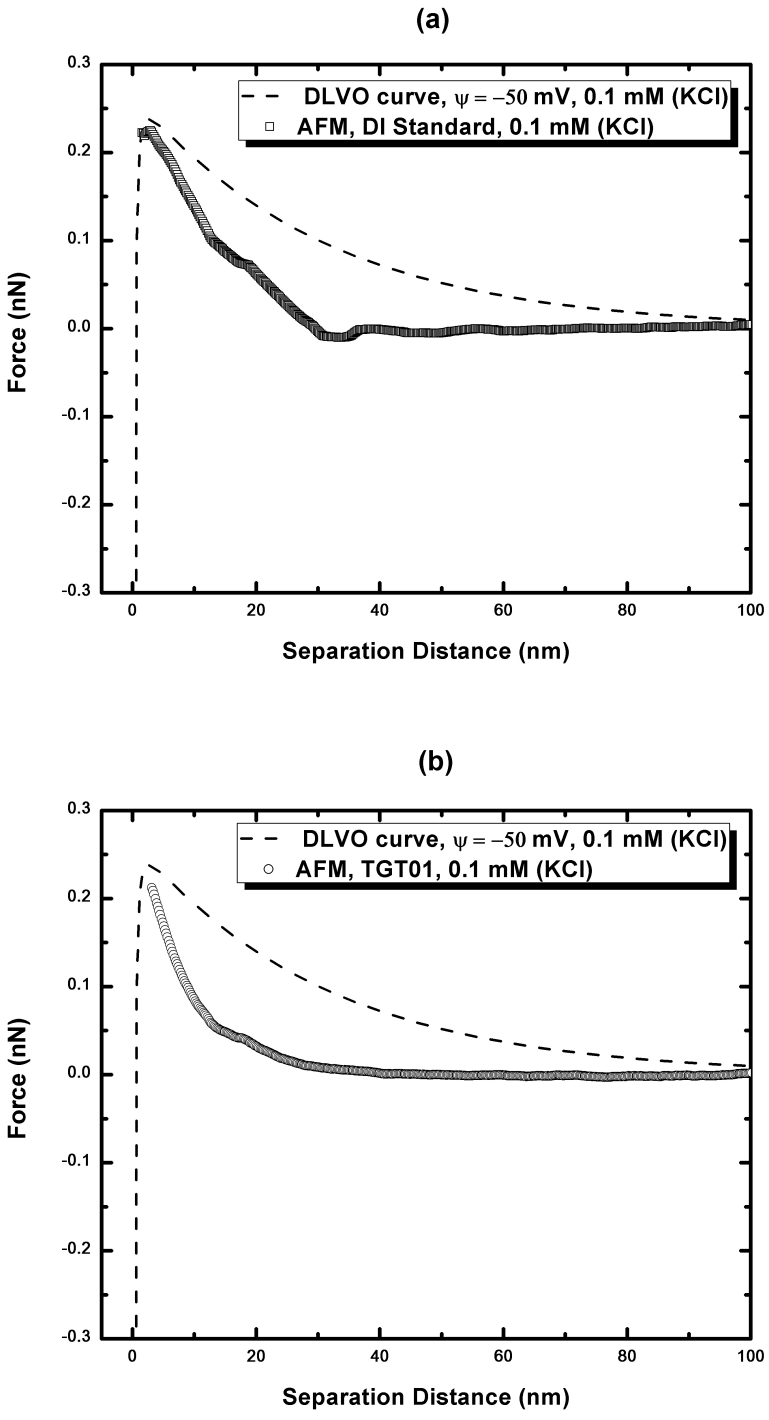

Figure 5.5: AFM force measurement results for DNP-S20 probe over: **(a)** *DIstandard*, and **(b)** *TGT01* under 0.1 mM KCl. The results are compared against analytically derived DLVO interaction force.

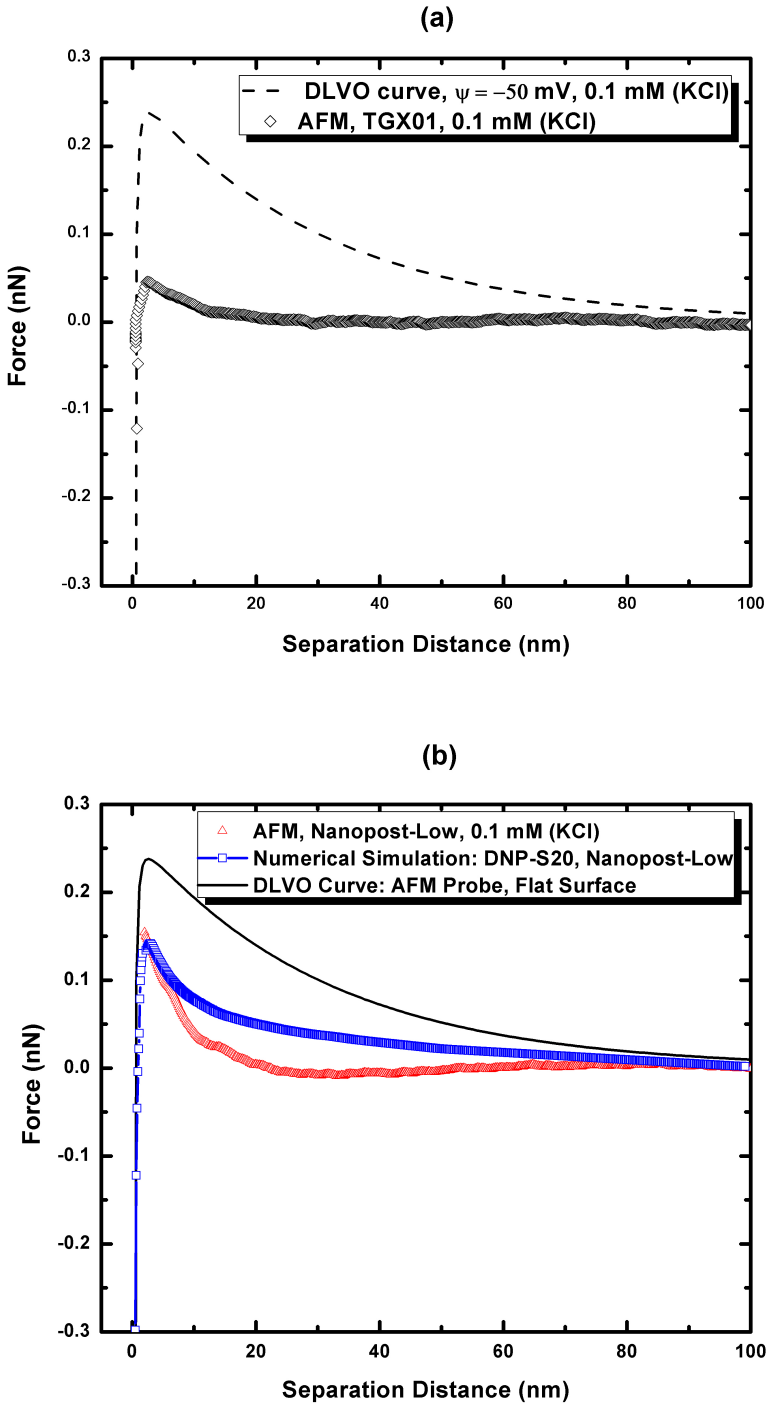

Figure 5.6: **(a)** AFM force measurement results for DNP-S20 probe over *TGX01* under 0.1 mM KCl. **(b)** Comparison of the AFM force measurement on $nanopost - low$ substrate with DLVO curve (solid black line) associated to a flat surface modeling, and a numerical simulation (blue symbols) associated to a rough surface modeling.

Finally, figure 5.6a depicts the force measurements corresponding to the *TGX01* substrates. This substrate has caused the largest divergence in interaction force among other rough substrates. This can also be explained in the same context provided in the previous paragraph, however in this case, it is more probable that the probe to be closer to one of the valleys. Considering the geometrical parameters of the probe and surface, one may relate the huge attraction observed in the force plot to the interaction between the probe inclined walls and the valleys of surface. It is also reported elsewhere [Bowen and Doneva, 2000] that the adhesion is greater in valleys of a substrate than the peaks. Also, it is obvious that this phenomenon is more probable to occur in *TGX01* than in $DI - standard$, since the pitch distance in *TGX01*, which is 3 μm, is less than one third than of that in $DI - standard$. Moreover, the surface area difference (SAD), calculated by AFM roughness analysis toolbox, is 25.78 % for *TGX01*, where this parameter is only 1.58 % for $DI - standard$, meaning that the percentage of depressions are much higher in *TGX01* [*cf.* chapter 3, Figures 4.2 and 4.3, parts **(c)** and **(e)**].

So far, according to the experimental fore measurements by AFM, it is observed that the magnitude of the interaction forces are lower on the model rough substrates than the smooth flat surface of a glass substrate. In fact, this the repulsive barrier between the probe and the surface, that has been decreased on the rough surfaces. To ensure that such a behavior can be interpreted by considering the surface heterogeneities (roughness) in the DLVO calculation, a numerical simulation has been developed, which simulates the interaction of a model probe and a rough surface. In this regard, the $nanopost - low$ substrate, among other four rough substrates, is chosen to be mathematically modeled. The roughness elements are modeled as hemispherical protrusions which are uniformly patterned on a square lattice unit as in Figure 3.2a in Chapter 3.

According to the geometrical parameters provided in Table 4.2 in Chapter 4, the radius of asperities is $a_s = 20$ nm, the pitch distance is $P = 0.23$ μm in the modeled surface. The total size of the model surface in X and Y direction

is 3.91×3.91 μm, comprising 17 asperities in each direction. The approaching probe was generated using a model proposed in Figure 3.6b in Chapter 3 for a pyramidal shape, in order to better represent an actual AFM DNP-S20 probe. The height of the model probe is $H = 5$ μm, and its hemispherical head radius is of $a_p = 20$ nm.The size of square base of the pyramidal probe is equal to the surface base (*i.e.*, 3.91×3.91 μm). The mesh size in X, Y direction in both of the modeled structures is 5 nm by 5 nm.

The mathematical calculation using SEI followed an algorithm provided in Figure 3.10 in Chapter 3 to find the van der Waals and electrostatic force for the above system. However, in this simulation, the interaction force, rather than energy, is of interest, since in AFM results the colloidal forces are presented. Therefore, the imported expressions of the Hamaker and the LSA energy per unit area (for van der Waals and EDL energies respectively) were substituted by their derivatives in terms of the separation distance h, in order to calculate the force rather than energy. The van der Waals and EDL forces are then added together to form the overall DLVO energy. The Hamaker constant $A_H = 2.258 \times 10^{-20}$, according to Eqn. (3.41), the probe and substrate surface potentials, ψ_p and ψ_s are assumed to be -50 mV (see section 3.4.1 in Chapter 3).

The result of this simulation is compared with the AFM force measurement over $nanopost - low$ substrate in Figure 5.6b. In this plot, the red symbols represent the experimental measurements, the blue symbols depict the numerical calculations for the system, and the black solid line is the DLVO curve for a probe interacting with a flat surface. According to this plot, it is evident that by including the surface roughness, the results obtained experimentally are closer to the theoretical calculations. However, the results of the numerical simulation are still not completely matched with the experimental observations. This might be due to one of the reasons as follows: The asperities of the surface were modeled as hemispherical elements, while the actual shape of the asperities was reported by Choi *et al* [Choi et al., 2007] to be in pointy shapes that cause lesser interaction than hemispheres; One may also ascribe

this difference to the insensitivity of AFM measurements at farther separations (10 to 60 nm). Nevertheless, this analysis clearly proves the profound need of inclusion of surface morphological parameters into the calculation of the colloidal forces, whereas the calculations based on a flat surface are much more inconsistent with the experimental observations.

Lastly, it is pertinent to mention that all the experimental results, presented in sections 5.2.1 and 5.2.2, are the average of 25 force measurements for each particular test, and the results are smoothed by taking the adjacent average values of individual data points of the AFM force plots. Also the results are taken from the *trace* path of the probe *trace/retrace* cycle in the experimental force measurements (see Chapter 4).

5.3 DLVO Interactions over Rough Surfaces

In the previous section, the AFM force measurements over smooth and rough surfaces with different nano-scale roughness patterns were presented. It was then concluded that although AFM provides general information about the influence of surface roughness on the colloidal interaction, the precision of the experimental results, and their sensitivity in detecting the small-range forces are not adequate to comprehensively characterize the divergence seen in the interaction energies as a result of the presence of physical heterogeneities. Yet, by simulating the interaction between a pyramidal probe and a rough surface (representing the DNP-S20 probe and the $itnanopost - low$ substrate, respectively), it was proved that by inclusion of the surface roughness into the calculations, the values of theoretical interactions become closer to the experimental measurements. Thus, in this section, it is attempted to find the correlation between the DLVO interaction energies and surface roughness mathematically. The analytical derivations developed for three sets of asperity shape, namely, hemispherical, conical, and cylindrical, modeled in the form of protrusion and depression, were presented in section 3.3 of chapter 3. In this section, the corresponding results for each of these asperities are presented.

5.3.1 Hemispherical Asperities

Hemispherical Protrusions

Figure 5.7a depicts the variation of the scaled van der Waals (VDW) interaction energy per unit area,[Chapter3: Eqn. (3.15)], with scaled separation distance $h^* = h_0/a$. All the lengths are scaled with respect to the hemispherical asperity radius. The results are shown for four different values of the scaled pitch, $P^* = P/a$, with $P^* = 2$ representing the closest (touching) configuration of two adjacent asperities (Figure 5.7).

In all cases, the presence of hemispherical asperities reduced the magnitude of the VDW interaction compared to the smooth flat plate energy. For scaled separations greater than 10, the interaction energy became identical to that between smooth flat plates irrespective of positioning of the asperities (scaled pitch). In other words, roughness had no influence on long-range VDW interactions. This was also cited in earlier experimental observations [Brant et al., 2006], where the disagreement in the interaction of a silica colloidal probe with a polymeric surface was less pronounced at larger separations.

In contrast, for smaller separation distances, the scaled interaction, E_r/E_s, was significantly reduced from its long-range value of unity. This was more prominent at larger values of P^*. Near contact [$h^* \approx 10^{-3}$], the scaled energy per unit area decreased as P^* increases. This behavior may be of significant interest in context of lowering adhesion between surfaces as the presence of minute asperities could prevent the two infinite flat plates from coming in contact with each other. On the other hand, even when the asperities were located with P^* equal to 2 (nearest neighbor), the contact energy was almost 3 orders of magnitude smaller than from the corresponding smooth plate energy. In summary, hemispherical protrusions dramatically decrease the magnitude of near field VDW interaction.

At this point, it is pertinent to discuss the implication of these results in context of retarded VDW interaction. For nano-scale colloidal objects, retardation is prominent only at large separations, with minimal effect on near

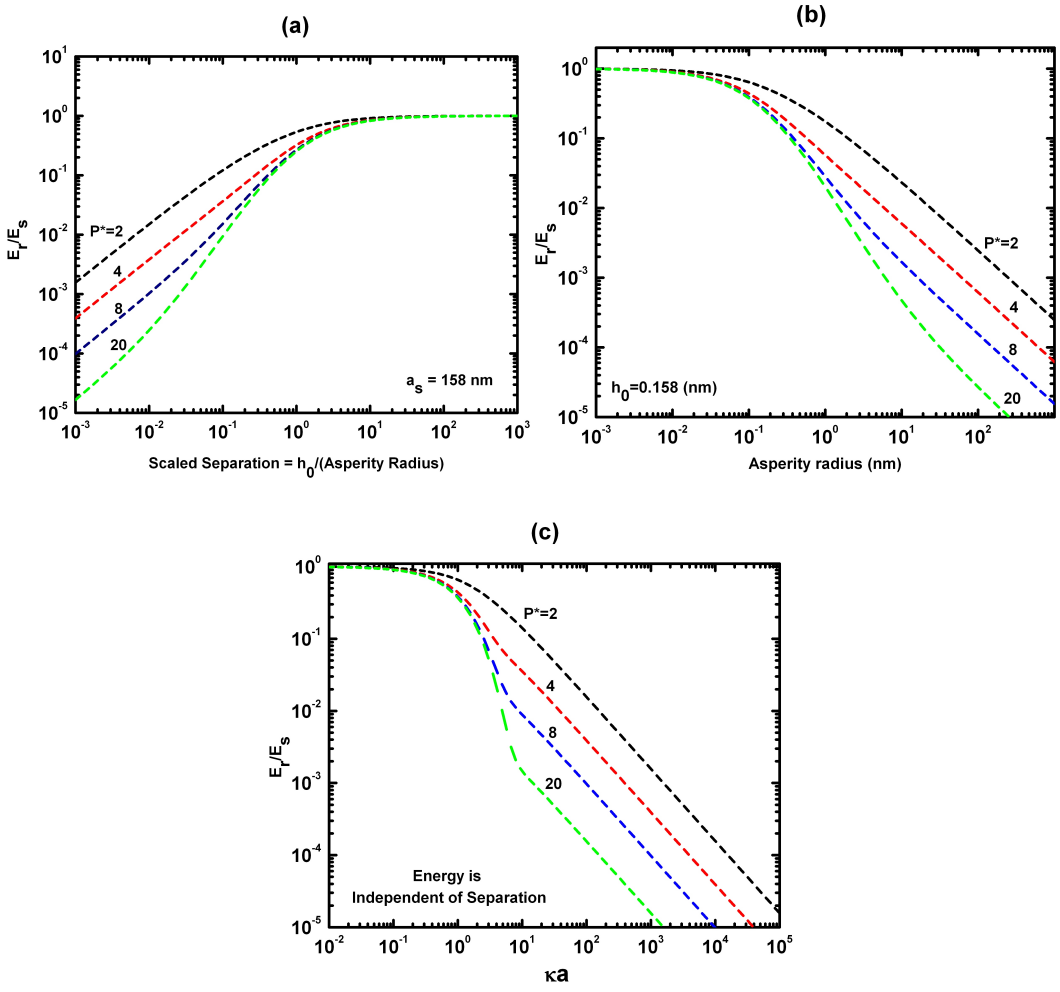

Figure 5.7: Normalized van der Waals **(a-b)** and electrostatic **(c)** interaction energy profiles per unit area of a rough surface consisting of hemispherical protrusions versus: **(a)** scaled separation, **(b)** asperity radius, and **(c)** κa.

field VDW interactions [Gregory, 1981]. Our analytical expressions for the VDW interactions, which are based on non-retarded dispersion forces, should therefore accurately predict the near field, and dominant effects of roughness on VDW interactions without need of invoking retardation.

Figure 5.7b shows the scaled VDW interaction energy per unit area at contact for a single asperity size. Defining a minimum cut-off distance for closest approach between two surfaces as 0.158 nm [Masliyah and Bhattacharjee, 2006], one may now plot in Figure 5.7b the scaled contact VDW interaction energy per unit area as a function of the asperity radius. It is evident from Figure 5.7b that for asperities larger than *ca.* 0.5 nm, the contact value of the specific VDW energy decreases considerably from the corresponding smooth surface energy. Once again, with increasing P^*, the decrease in energy becomes more pronounced. For 5 nm radius asperities, the reduction in the scaled specific energy is about 16 times for $P^* = 2$, and about 500 times for $P^* = 20$.

The profiles in Figure 5.7c represent the influence of protruding hemispherical features on the electric double layer (EDL) interaction energy. It was shown earlier in chapter 3, Eqn. (3.18), that the scaled energy, E_r/E_s, for the EDL interaction is independent of separation. In Figure 5.7c, the variation of the electrostatic energy per unit area is shown as a function of κa, where κ is the inverse Debye screening length, and a is the asperity radius. The parameter κa can be addressed as a measure of the ionic strength of the electrolyte solution for a fixed asperity radius, a. Similar to the VDW energy for protrusions (*i.e.*, Figure 5.7a and b), higher values of P^* reduced the EDL energy to a greater extent. Interestingly, the variation of the energy was linear (on the log-log plot) with respect to κa for $\kappa a > 10$. The behavior observed for the EDL interaction is applicable to any interaction with an exponentially decaying function. It is pertinent to mention here that the general trend of the variation of the EDL energy with respect to the κa depicted in this graph was previously observed in earlier experimental studies [Brant et al., 2006]. Brant *et al.* have addressed that the impact of surface roughness in deviation of the

AFM measurement data for surface zeta potential from its original value is more at higher ionic strengths.

Hemispherical Depressions

Figure 5.8a illustrates the variation of the VDW interaction energy per unit area for a rough surface consisting of hemispherical depressions (rather than protrusions), with the scaled separation distance. In order to compare the results with protruding asperities, the same set of scaled pitches, P^*, as in Figure 5.7 are chosen.

Similar to Figure 5.7a, in Figure 5.8a, the presence of asperities decreases the magnitude of VDW interaction energy. However, the reduction is almost negligible for $P^* \geq 20$. For higher asperity densities ($P^* = 8, 4, 2$), the reduction becomes more predominant at shorter separation distances. In Figure 5.8a, at the minimum separation, the scaled VDW interaction (E_r/E_s) was diminished by almost a factor of 5 for $P^* = 2$. This is in contrast to Figure 5.7a, where presence of asperities in protruding form and with identical pitch distances reduced the scaled contact energy by 3 orders of magnitude; hence, hemispherical protrusions alter VDW interaction energy much more severely than hemispherical depressions.

At scaled separations lower than *ca.* 0.1, the normalized VDW energy became practically independent of distance for all values of scaled pitch. For scaled separations between 0.1 and 10, the interaction energy ratio increased sigmoidally. For larger separations, the effect of depressions on the interaction energy can be neglected. Hemispherical protrusions and depressions behave oppositely in terms of the effect of the asperity density on the interaction. Lower values of P^* (*i.e.*, higher asperity density) reduce the VDW interaction in case of depression up to a greater extent, whereas for protrusions, lower values of P^* cause lesser reduction of the interaction energy. This is due to the inverse relation of the VDW energy to separation distance.

Figure 5.8b shows the scaled contact energy ratio for various asperity sizes. This figure also illustrates that the reduction in energy was detected for as-

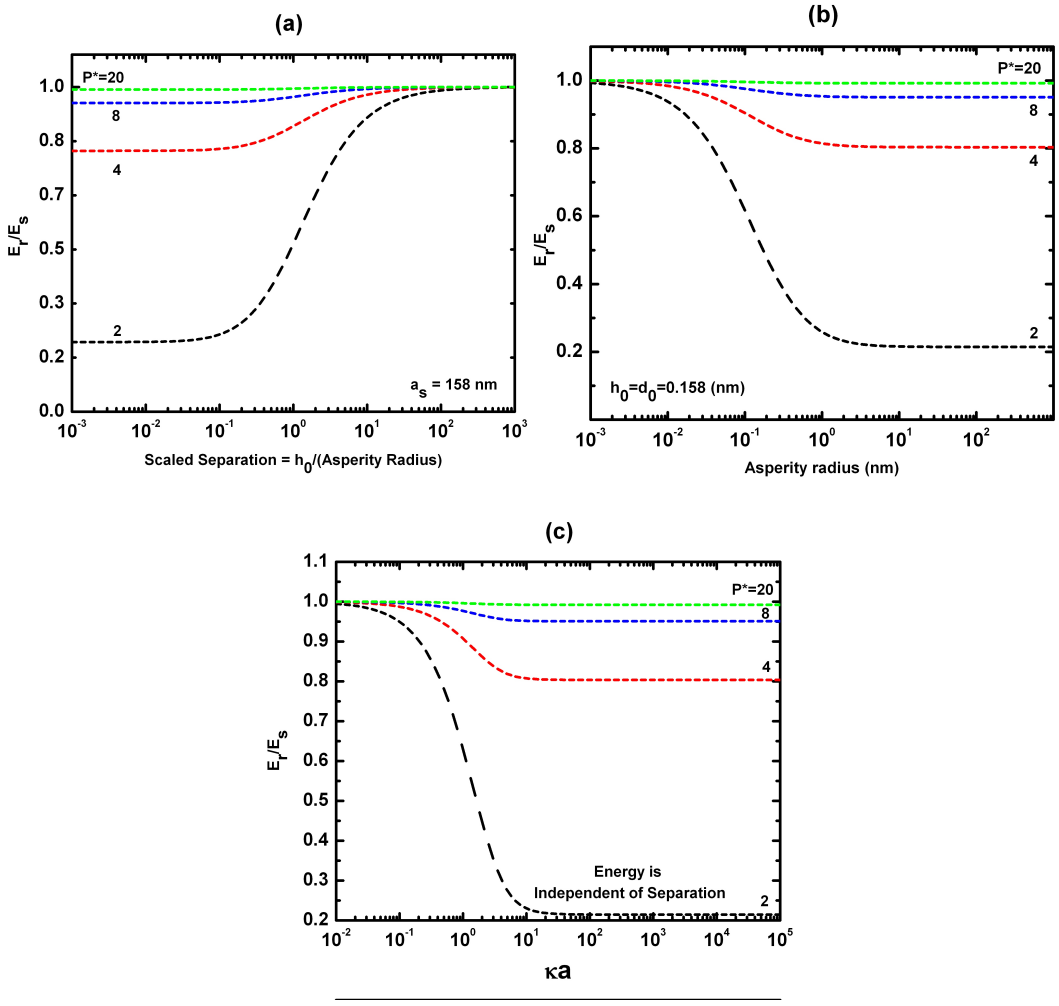

Figure 5.8: Normalized van der Waals **(a-b)** and electrostatic **(c)** interaction energy profiles per unit area of a rough surface consisting of hemispherical depressions versus: **(a)** scaled separation, **(b)** asperity radius, and **(c)** κa.

perities larger than 0.002 nm (*i.e*, 0.02 angstrom). Irrespective of P^*, the energy profiles became independent of distance for radii larger than 1 nm. By comparing Figure 5.7b and Figure 5.8b, it can again be highlighted that depressions reduced VDW energy to a lesser extent than protrusions. Figure. 5.8c depicts the variation of scaled EDL energy E_r/E_s versus the κa. For depressions, similar to the VDW interaction energy, smaller values of P^* have contributed to higher extent of reduction in EDL interaction energy. On the other hand, although the scaled EDL interaction energy is independent of the separation distance as in Figure 5.7c, the energies in this plot also become independent of κa for κa of larger than 10.

5.3.2 Conical Asperities

Conical Protrusions

In Figure 5.9a, b the variation of the normalized van der Waals (VDW), and in Figure 5.9c the variation of normalized electric double layer (EDL) interaction energies with respect to scaled separation and κd are presented respectively, where d is the vertical height of the cone (*cf*. Chapter 3: Figure 3.8). Generally, the interaction energies complies with the behavior seen for hemispherical protrusions, where larger P^* causes less divergence in E_r from E_s (Figure 5.9b, c). Also in part (a) of this figure, larger asperities contributed to higher reduction in the interaction energy (*i.e*., lesser E_r/E_s) at different separations. The energy profiles in parts (a), and (b) have a sigmoidal form, and they converge at lower separations, where it is in contrast with hemispherical protrusions. Increasing κd will decrease the scaled interaction energy as previously seen in hemispherical asperities.

Conical Depressions

The normalized energy profiles shown in Figure 5.10 correspond to a model rough surface with conical depressions as in Figure 3.8b (Chapter 3). Similarly, since the asperities are in depressed form, larger P^* will result in larger normalized interaction energy E_r/E_s at each separation distance. Figure 5.10b

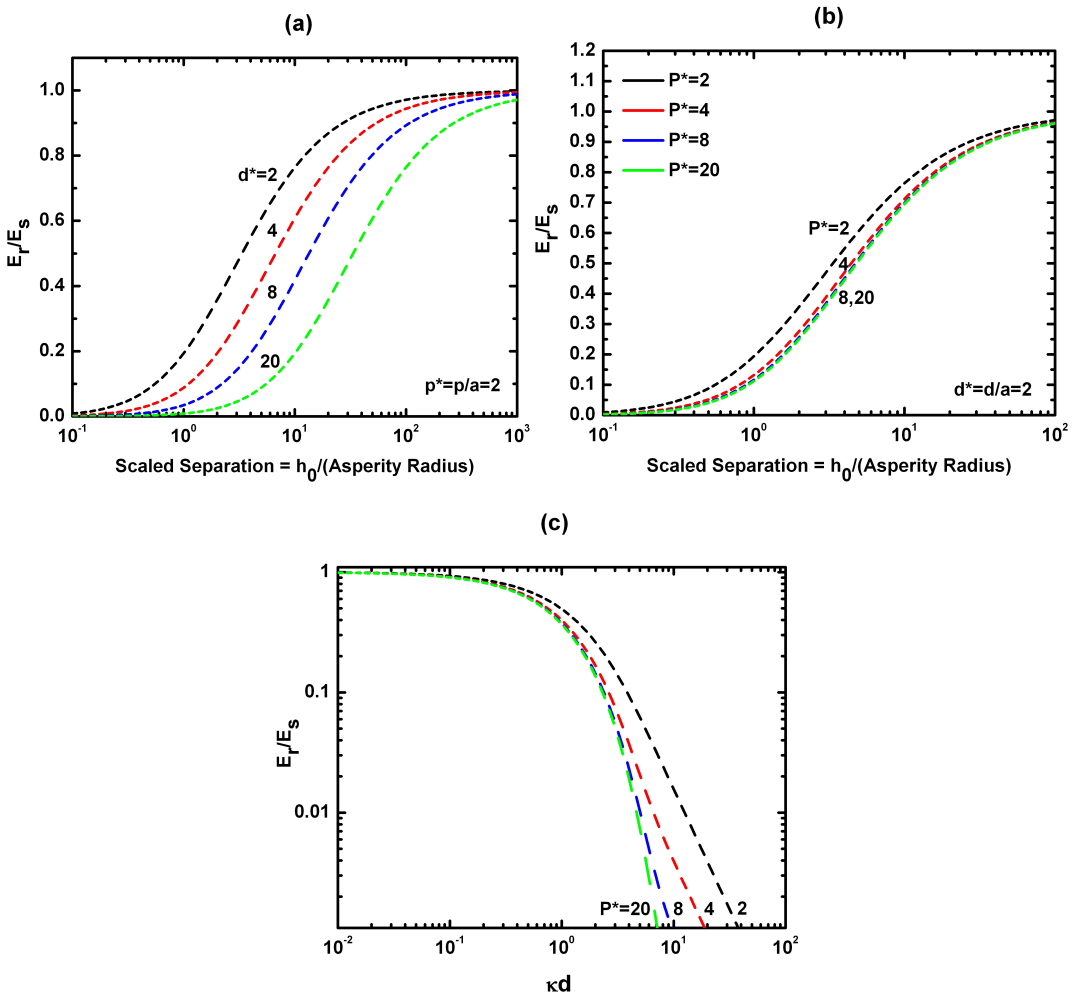

Figure 5.9: Normalized van der Waals **(a-b)** and electrostatic **(c)** interaction energy profiles per unit area of a rough surface consisting of conical protrusions versus: **(a-b)** scaled separation and **(c)** κd.

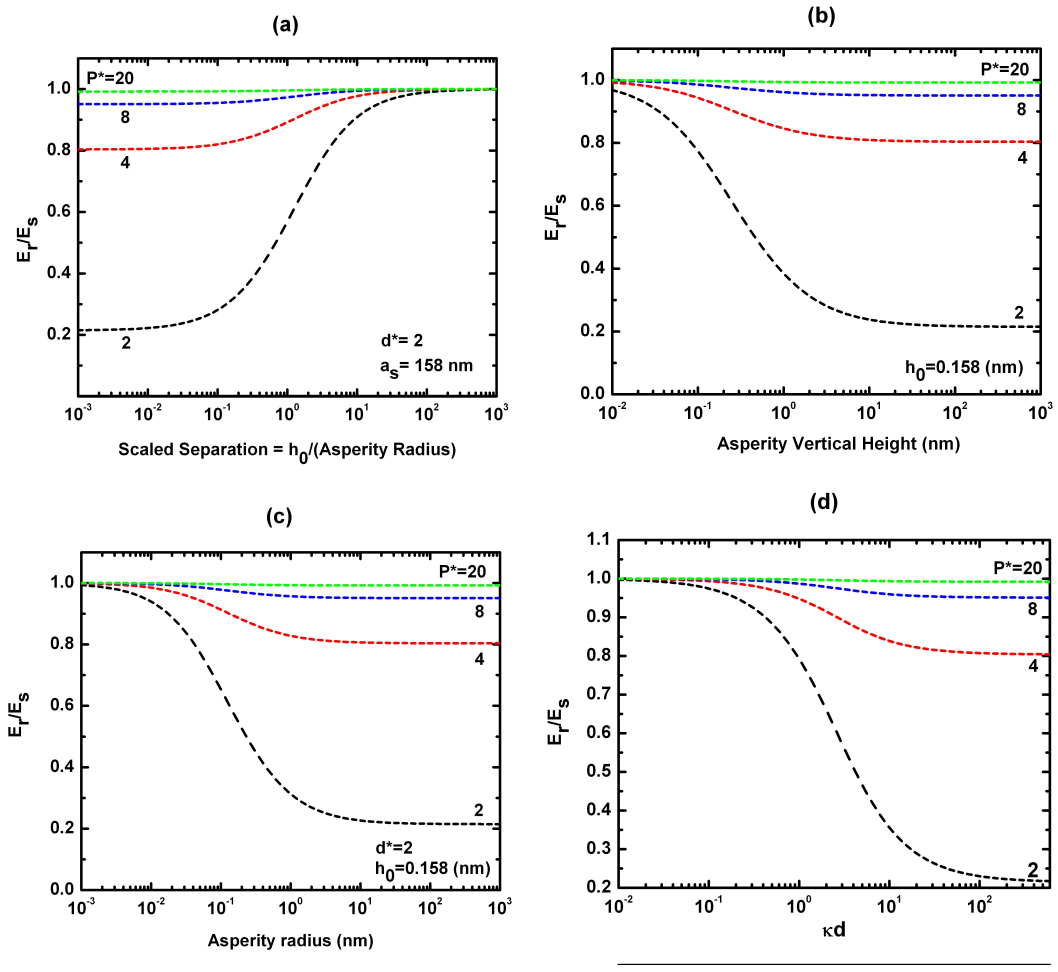

Figure 5.10: Normalized van der Waals **(a-c)** and electrostatic **(c)** interaction energy profiles per unit area of a rough surface consisting of conical depressions versus: **(a)** scaled separation, **(b)** asperity vertical height d, **(c)** asperity circular base radius, and **(d)** κd.

and (c) that depict the change in normalized energy as a function of asperity size, are almost identical to Figure 5.8b. However, the reduction in energy is more pronounced in hemispherical depressions than that in conical depressions. For instance, for the asperity radius of 0.1 nm and $P^* = 2$, E_r/E_s ratio is 0.5 for hemispherical (Figure 5.8b) and 0.7 for conical (Figure 5.8c) depressions. Also, it must be highlighted that this is for $d^* = 2$. Comparing Figures 5.8c and 5.10d for electrostatic energy, one may observe that conical depressions cause a similar response in normalized EDL energy, but the energy is less attenuated for κa (or κd) between 0.1 to 100 for conical features.

5.3.3 Cylindrical Asperities

Cylindrical Protrusions

Energy plots in figures 5.11 refer to the variation of normalized interaction energy as a consequence of the presence of cylindrical form protrusions as the roughness elements (Chapter 3: Figure 3.9). The variation of normalized van der Waals (VDW) energy against the scaled separation distance in Figure 5.11a has a sigmoidal form similar to what was previously seen for conical protrusions in Figure 5.9a. In contrast, comparing the individual energy profiles in Figures 5.9a and 5.11a, it is evident that reduction in energy is much more severe based on conical protrusions than cylindrical protrusions. As a matter of fact, the VDW energy is inversely proportional to the separation distance h. On the other hand, the cross-sectional area in a cylinder is constant, while in a cone it decreases at upper cross-sections until it reaches to zero, leading to less interaction energy between the two surfaces at a equal separation distances. For instance, for $b^* = 8$ and $d^* = 8$, and for $h^* = 10$, the normalized VDW energy E_r/E_s for cylindrical shapes is 0.85, whereas it is only 0.4 for conical elements. At closer separations, this quantity reaches its minimum of $\simeq$0.8 for cylinders, whereas it has diminished to zero for conical asperities.

One may also observe that the difference between energy profiles in Figure 5.11b, which distinguish the influence of scaled pitch distance P^*, are much higher than the difference between these profiles for conical asperities (Figure

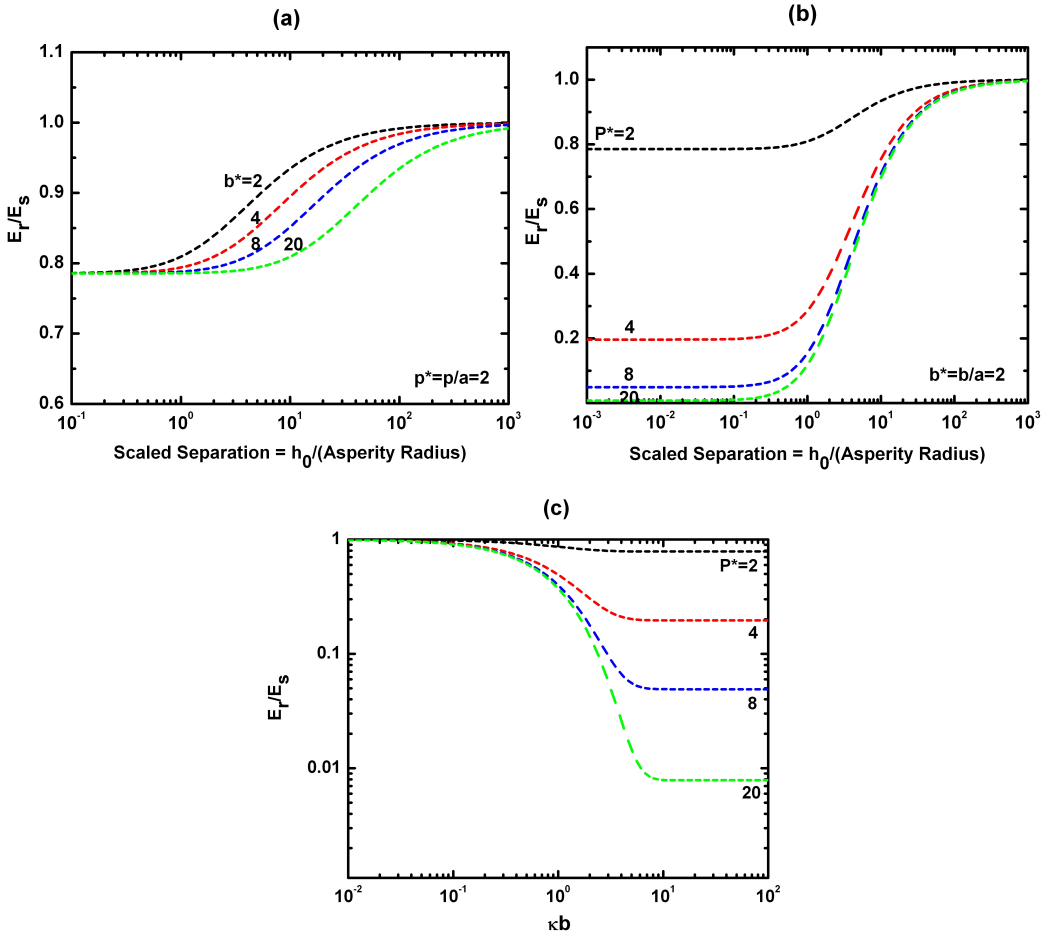

Figure 5.11: Normalized van der Waals **(a-b)** and electrostatic **(c)** interaction energy profiles per unit area of a rough surface consisting of cylindrical protrusions versus: **(a-b)** scaled separation and **(c)** κb.

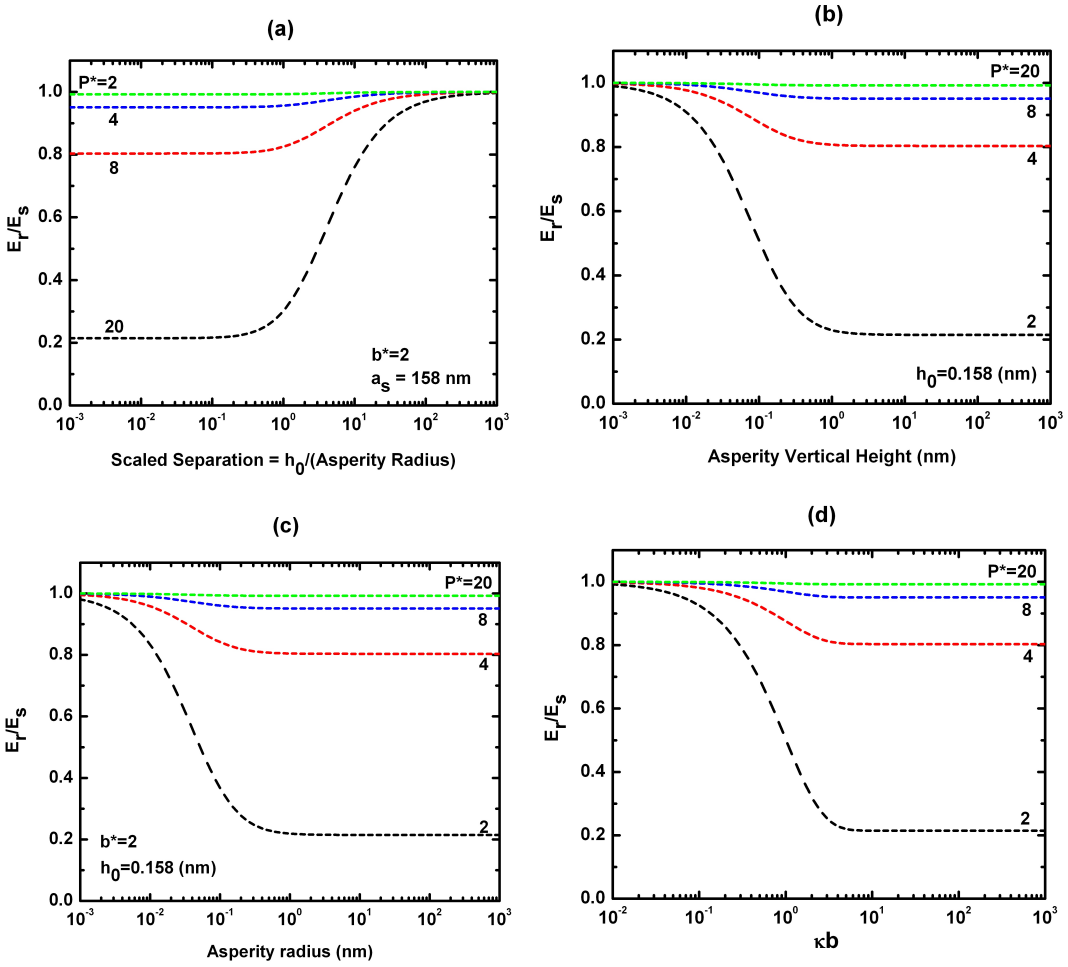

Figure 5.12: Normalized van der Waals **(a-c)** and electrostatic **(c)** interaction energy profiles per unit area of a rough surface consisting of cylindrical depressions versus: **(a)** scaled separation, **(b)** asperity vertical height d, **(c)** asperity circular base radius, and **(d)** κd.

5.9b) for $10^{-1} \leq h^* \geq 10^1$. This is again based on the fact that the energy attenuation is seen to be larger for conical shapes. In other words, for $P^* = 20$ the normalized energies have reduced to zero for both conical and cylindrical shape asperities at $h^* = 0.1$, while for $P^* = 2$, the E_r/E_s ratio reaches to 0.8 for cylindrical geometries, and it remains to zero for conical shapes. This interpretation is also valid for the variation of normalized electrostatic energy against the molarity strength κb depicted in Figure 5.11c for κb (or κd) larger than 2, as EDL energies are also inversely proportional to the separation distance.

Cylindrical Depressions

Finally, if the roughness features are modeled as cylindrical depressed elements, one may observe in Figure 5.12 that the normalized interaction energies are acting similar to the energy profiles in conical depressions. However, the depressions in cylindrical form decrease the DLVO interactions up to a higher extent, than the conical depressions. As explained in the previous section, this is opposite to what was seen for protruding asperities of theses two forms. Following the discussion in the previous section, this is due to the fact that inclined walls in conical holes contribute to more interaction energy to the interacting body at each separation distance, than the vertical walls of cylindrical holes.

5.4 Numerical Simulations

5.4.1 Energy Distribution as a Result of AFM Probe Relocation

As pointed earlier in section 5.2, the forces measured by AFM are based on a random lateral location of the probe over the surface. It was also cited in Zhao's *et al.* [Zhao et al., 2008] work, that the variety of results in the obtained force profiles can be attributed to the random roughness of the surface. In other words, the interaction curve is sensitive to the position of the probe over

the surface. In the present study, it was observed that the force plots gathered from AFM force measurement needed to be interpreted by having a knowledge about the tested surfaces morphology. In this section, it is demonstrated that how the probe-surface interaction varies, when the probe is moving over a surface laterally. To this end, the probe is modeled as a hemispherical tip as shown previously in Figure 3.4 (Chapter 3).

The topographical heterogeneities on the surface are decided to be patterned in a periodic order. Also the asperities are modeled as hemispherical protrusions. The periodicity of the substrate and hemispherical shape of the asperities assists us to develop a geometrical analysis, in which the variation of interaction over the entire surface can be investigated by defining a unit cell.

This unit cell is depicted in Figure 5.13. Assuming the center of the model spherical probe (blue circle) is initially located at the center of the unit cell, the $P \times P$ square is the area that the probe has to traverse to find the energy distribution over this unit cell. However, due to geometrical periodicity, the energy distribution over the red $P/2 \times P/2$ square, illustrated on the top corner of the unit cell, is symmetric along the X and Y axes. Therefore, in the numerical calculations, the probe center point is only traveled along the red square, and the results for other areas in the $P \times P$ square are found symmetrically.

As another geometrical relation between a_p and a_s, provided that the probe can touch the bottom flat surface of the cell ($i.e.$, Eqn. 5.1 applies), the probe can remains on the surface until it reaches to an area within a distance of R_{min} from the center point of the surface asperity. R_{min} can be found as follows:

$$\frac{R_{min}}{a_s} = \sqrt{1 + \frac{2a_p}{a_s}} \tag{5.1}$$

Figure 5.14 depicts the distribution of the normalized van der Waals interaction energy between a unit cell described above and a spherical probe. This map represents the interaction over a $P \times P$ square depicted in Figure 5.13. In this test, the pitch distance on the surface is $P = 1000$ nm, and the radii of the surface asperities and the spherical probe are $a_s = 400$ nm, and $a_p = 425$

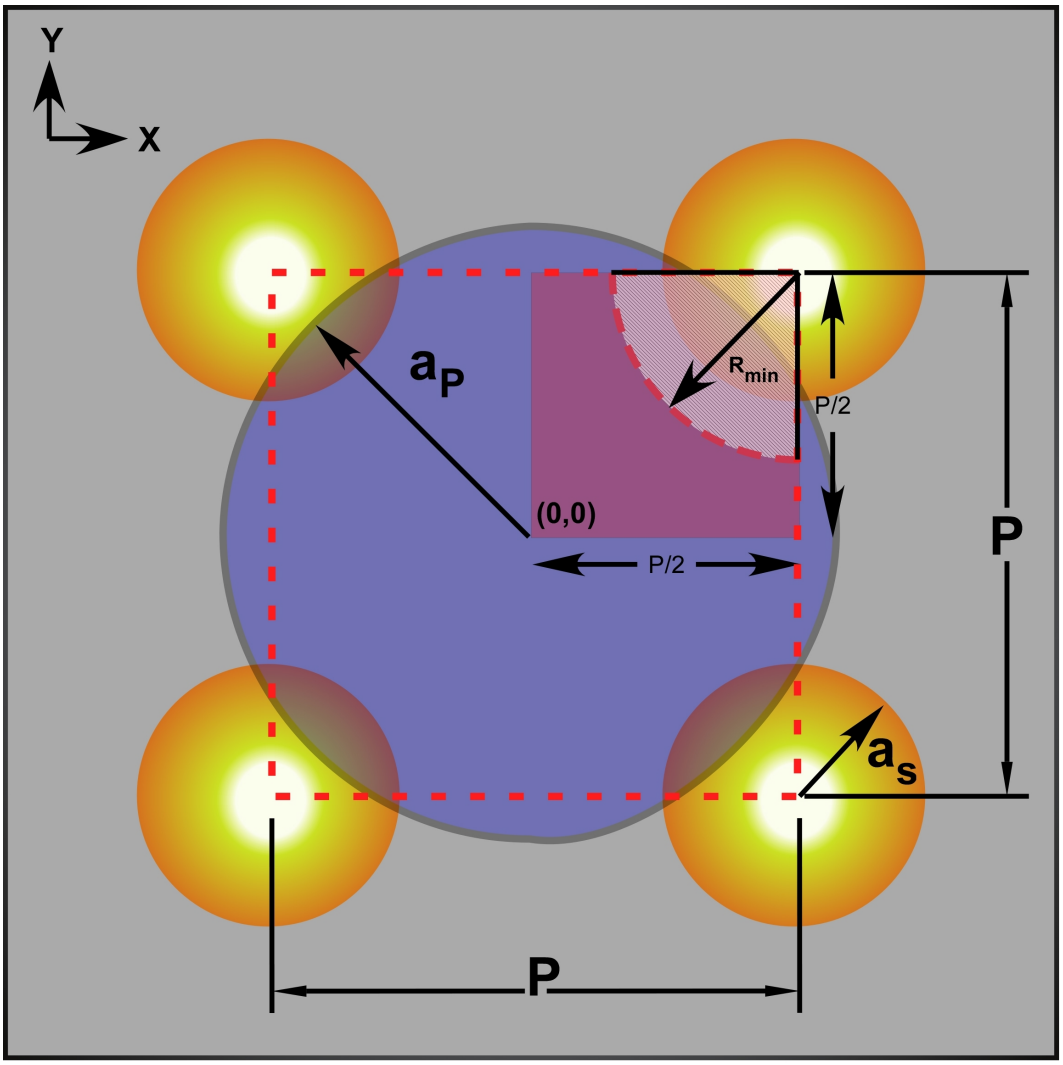

Figure 5.13: 2D schematic representing the unit cell used for investigation of energy distribution (Figures 5.14 and 5.15) over a periodically patterned surface, and its geometrical parameters.

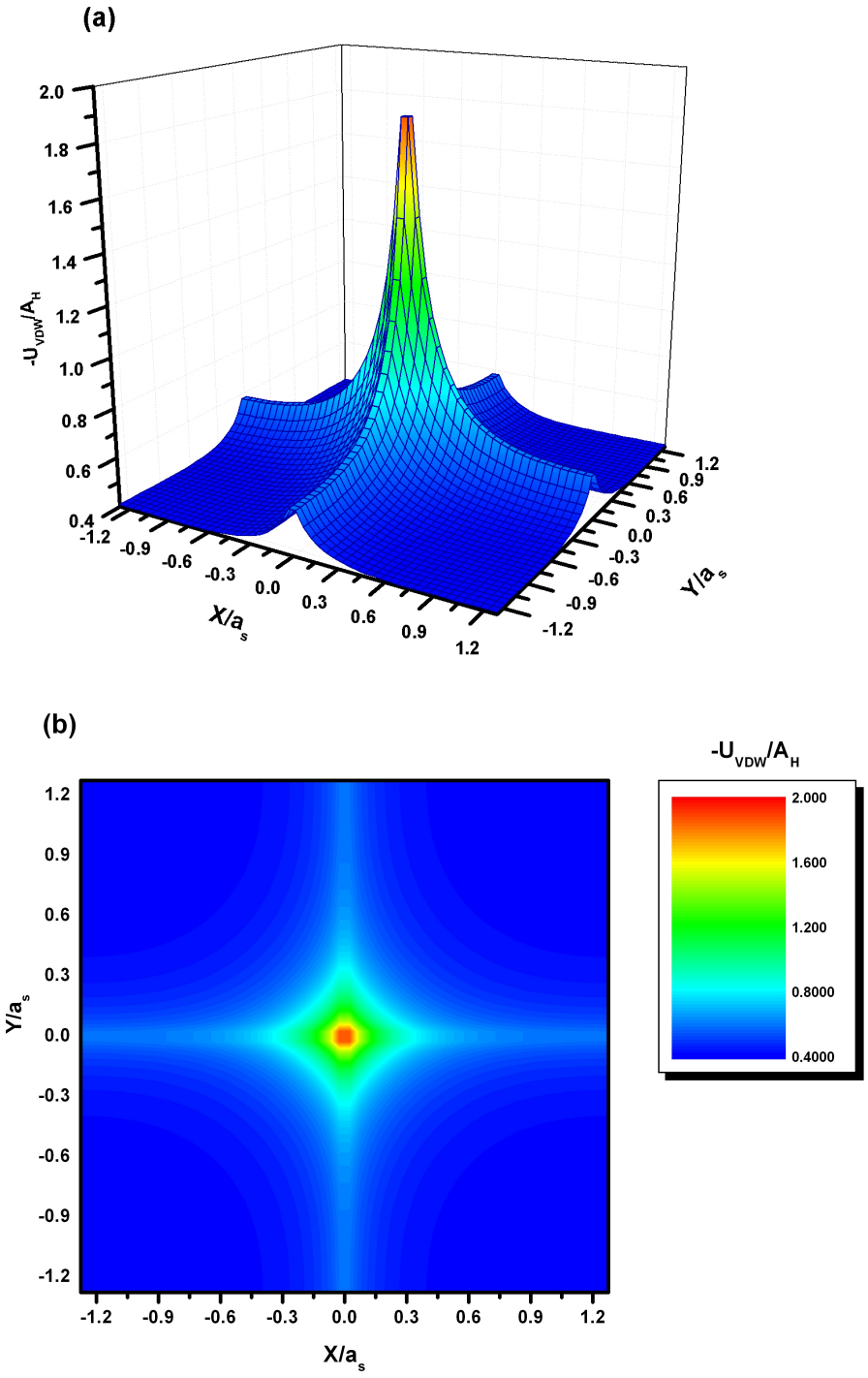

Figure 5.14: **(a)**: 3D map, and **(b)**: color map of the Distribution of normalized van der Waals interaction energy over a $P \times P$ unit cell illustrated in Figure 5.13. a_p=425 nm, a_s=400 nm, P=1000 nm, h_0=100 nm.

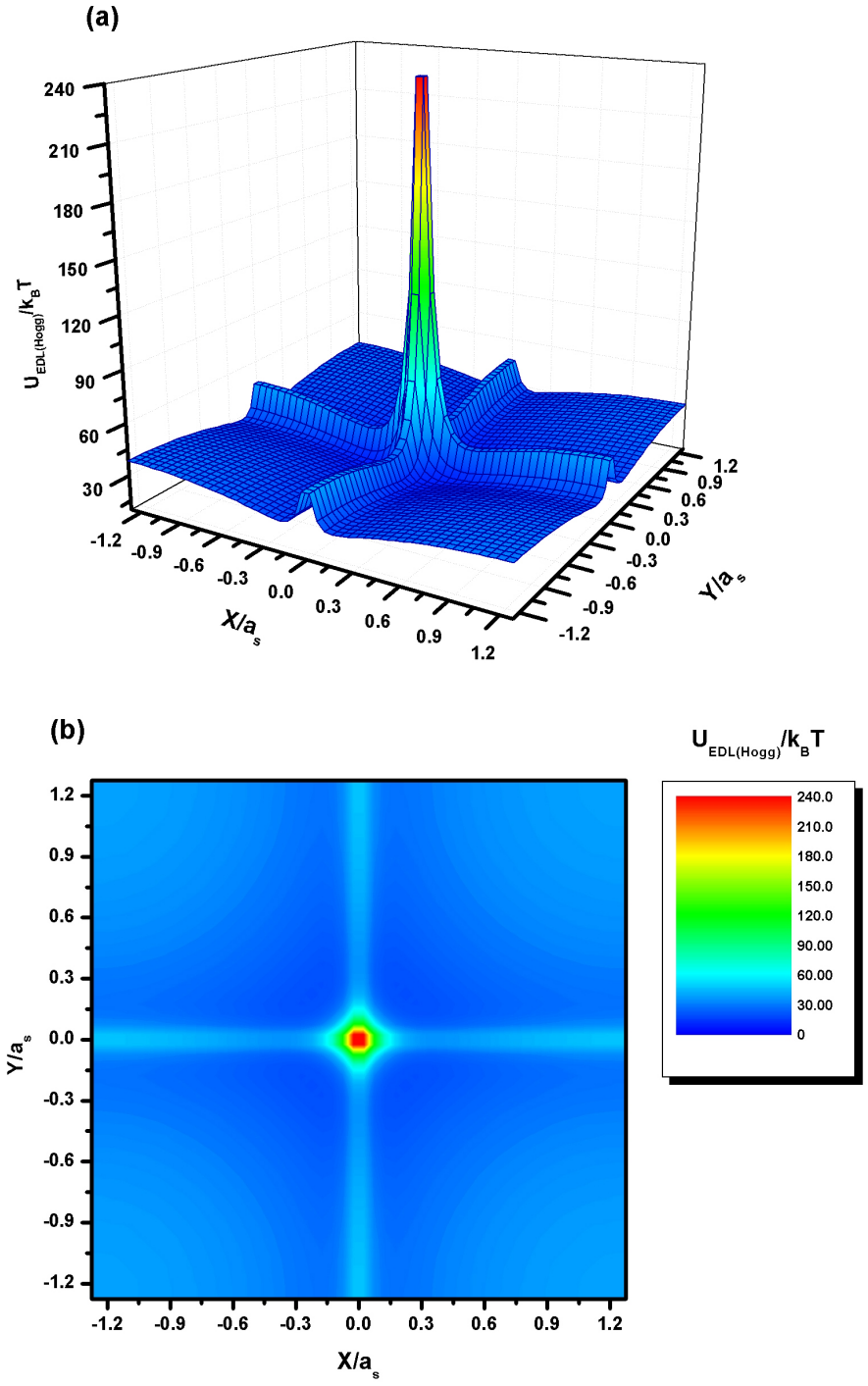

Figure 5.15: **(a)**: 3D map, and **(b)**: color map of the Distribution of normalized electrostatic interaction energy over a $P \times P$ unit cell illustrated in Figure 5.13. a_p=425 nm, a_s=400 nm, P=1000 nm, h_0=100 nm.

nm respectively. Based on these sizes, the left hand side and right hand side of the Eqn. 3.47 are equal; hence the model probe touches the surface only when its center is aligned to the point (0,0) in Figure 5.13, or on the other word, when the probe is located exactly at the middle of the four adjacent asperities. The initial distance between the lowest point of the probe and the flat surface underneath, namely the minimum separation distance h_0, is set to 100 nm. h_0 increases as a function of the probe relocation over the unit cell. As shown in Figure 5.14, although h_0 is identical over the entire unit cell area, the van der Waals energy varies at different lateral locations. The energy distribution in this figure declares that the probe has highest interaction with the surface, when it is placed between the asperities, and the energy has diminished as the probe moves away from this point. The normalized electrostatic energy distribution shown in Figure 5.15 has presented a similar behavior as van der Waals interaction. However the rate of decay in Figure 5.15 is much higher due to the exponential nature of the electric double layer interaction.

In an another scenario, the DLVO energy components distribution have been sought, when the probe has a constant separation distance from the bottom flat surface of model substrate in the entire unit cell tracking. Therefore, also in this analysis, the h_0 distance varies as a result of the surface asperities. Figures 5.16 and 5.17 depict the energy distribution for this scenario when the lowest point of the probe has held at a distance of 410 nm above the plain surface of the model substrate in Figure 5.13. Referring to the geometrical sizes mentioned in the third paragraph of this section, this means that the probe will stand only 10 nm above of the hemispherical asperities, when their centers align laterally. It must be noted that unlike to the previous scenario, the origin coordinate (0,0) of the $P \times P$ unit cell for this analysis is located at the center of the circular base of one of the hemispherical asperities. According to this explanation, it is observed in both the Figures 5.16, and 5.17 that the probe has the largest interaction with the surface when it is on top of the asperities, while it is opposite to the previous scenario.

Defining $\theta = 0^\circ$ along $X - X$ axis, and $\theta = 90^\circ$ along $Y - Y$ axis in the

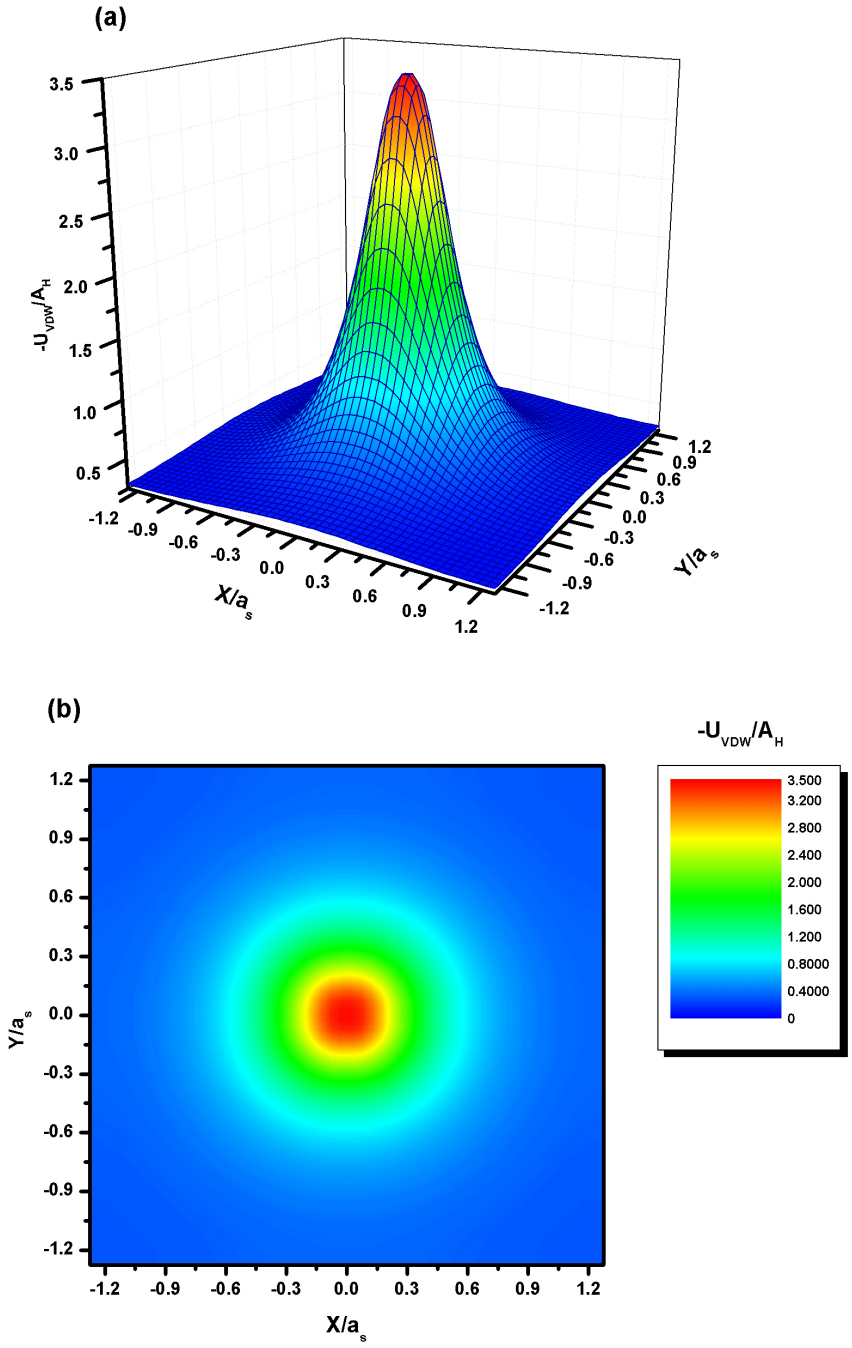

Figure 5.16: **(a)**: 3D map, and **(b)**: color map of the Distribution of normalized van der Waals interaction energy over a $P \times P$ unit cell, when its center is aligned with the center of one of the surface hemispherical asperities. The Probe is placed at a constant height of 410 nm from the bottom flat part of the sample substrate. a_p=425 nm, a_s=400 nm, P=1000 nm, 10 nm$\leq h_0 \leq$ 410 nm.

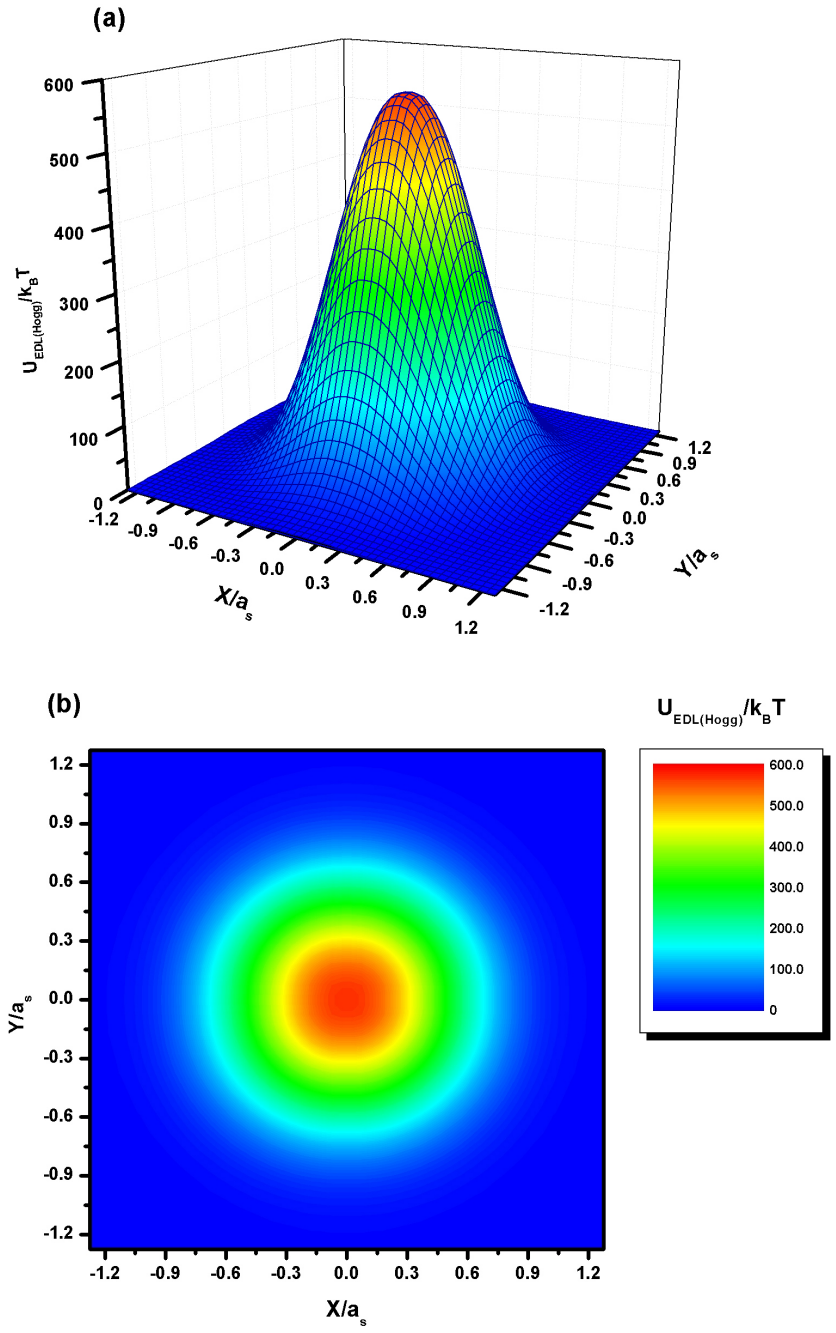

Figure 5.17: **(a)**: 3D map, and **(b)**: color map of the Distribution of normalized electrostatic interaction energy over a $P \times P$ unit cell, when its center is aligned with the center of one of the surface hemispherical asperities. The Probe is placed at a constant height of 410 nm from the bottom flat part of the sample substrate. a_p=425 nm, a_s=400 nm, P=1000 nm, 10 nm$\leq h_0 \leq$ 410 nm.

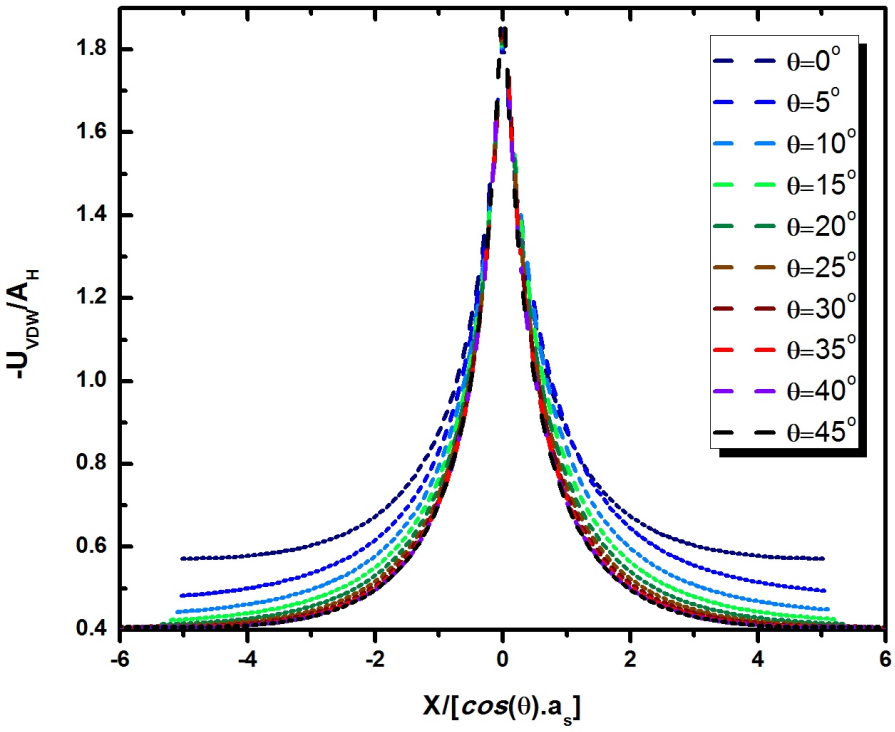

Figure 5.18: Energy profiles of van der Waals interaction energy distribution of Figure 5.14 at different angles.

color map of Figure 5.14b, one is able to extract the energy profiles of Figure 5.14a at different angles. These profiles are extracted for θ's of 0, 5, 10, up to 45 degrees as shown in Figure 5.18. A probability distribution analysis has been introduced on these energy profiles using a modified $Variance-Gamma$ probability distribution as the model function. This analysis will help us to use a mathematical model to introduce the effect of surface topographical heterogeneities without having any information about the size and other geometrical parameters of the roughness features. The curve fitting is performed by employing $Levenberg-Marquardt$ optimization algorithm which is a nonlinear form of the *least square* curve fitting approach. The modified $Variance-Gamma$ distribution function is given by:

$$\phi(x) = \frac{\gamma^{2\lambda}|x-\mu|^{\lambda-1/2}K_{\lambda-1/2}(\alpha|x-\mu|)}{\sqrt{\pi}\Gamma(\lambda)(2\alpha)^{\lambda-1/2}}e^{\beta(x-\mu)} + b(x-\mu)^2 \tag{5.2}$$

$$\gamma = \sqrt{\alpha^2-\beta^2} \tag{5.3}$$

where K_λ denotes a modified Bessel function of second kind, Γ denotes the Gamma function, and μ, α, β, λ and b are independent parameters. μ and β that represent the function center location and asymmetry of the distribution function with respect to the $X=0$ axis respectively, are equal to zero for the energy profiles presented in Figure 5.18. As a result, the curve fitting must be performed only by optimizing the values of α, λ and b which define the tail (height), scale, and base values for this model function. In this study, $\phi(x)$ represents the normalized energy. The optimized parameters are determined individually for each of the energy profiles shown in Figure 5.18, and the values are depicted in Figure 5.19a, b and c respectively.

The sum squared of residuals ($\sum r^2$) in the optimization process using $Levenberg-Marquardt$ algorithm varied from 5.91×10^{-6} to 3.77×10^{-4}. This provides sufficiently precise outputs in the line fitting operation. The optimized values for α, λ and b parameters shown in Figure 5.19 can be presented as a function of angle θ by fitting a polynomial of second order for α

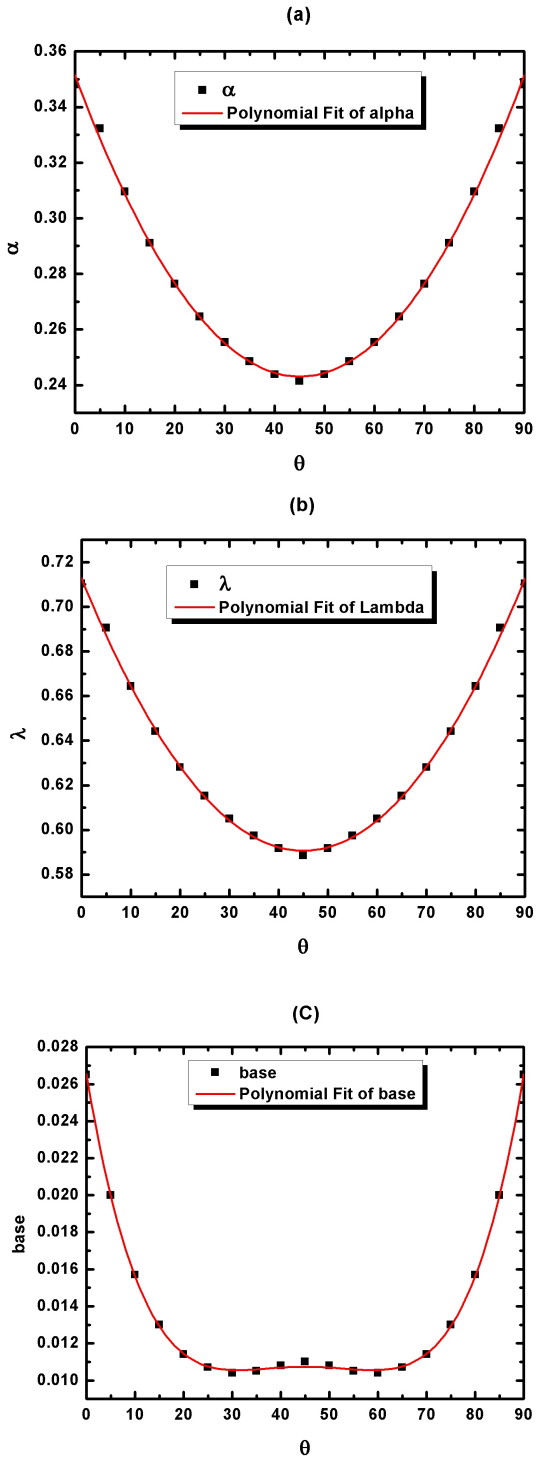

Figure 5.19: Optimized values of α, λ and b in Variance-Gamma model function, obtained from Levenberg-Marquardt algorithm for different energy profile of Figure 5.18, and the fitted polynomials.

and λ, and forth order for b. In particular, for the results shown in Figure 5.19, the equation of these polynomials (depicted as red lines) are as follows:

$$\alpha(\theta) = (-0.0048)\theta + (5.35 \times 10^{-5})\theta^2 + 0.3514 \tag{5.4}$$

$$\lambda(\theta) = (-0.0054)\theta + (6.02 \times 10^{-5})\theta^2 + 0.7127 \tag{5.5}$$

$$\begin{aligned} b(\theta) \quad &= (-0.0016)\theta + (5.61 \times 10^{-5})\theta^2 \\ &-(8.58) \times 10^{-7}\theta^3 + (4.77) \times 10^{-9}\theta^4 + 0.027 \end{aligned} \tag{5.6}$$

Replacing these functions into the Eqn. 5.2, one may fit a 3D mathematical model to the van der Waals energy distribution of the Figure 5.14. This analysis can be expanded for electrostatic energy, so that the effect of roughness for a set of particular topographical parameters cab be described using a mathematical equation.

5.4.2 Discussion on AFM Probe Exact Geometry Modeling

So far, in the current study, the interacting probe has been modeled as a hemispherical geometry. However, as described in chapter 4, the actual AFM probe (DNP-S20) has a pyramidal shape with a round head. Two different approaches for modeling the AFM probe was proposed in chapter 3, section 3.2.2. The first approach suggested to model the probe head by a hemispherical geometry, while in the more advance second approach, this geometry was a truncated hemisphere, such that it does not make any wall angle with the upper conical/pyramidal portion. In this section, it is attempted to investigate the difference between these two approaches for conical and pyramidal geometries, and also assess the role of other geometrical parameters in the interaction calculations. This is done by numerically calculating the interaction between the model probe and a smooth flat plate.

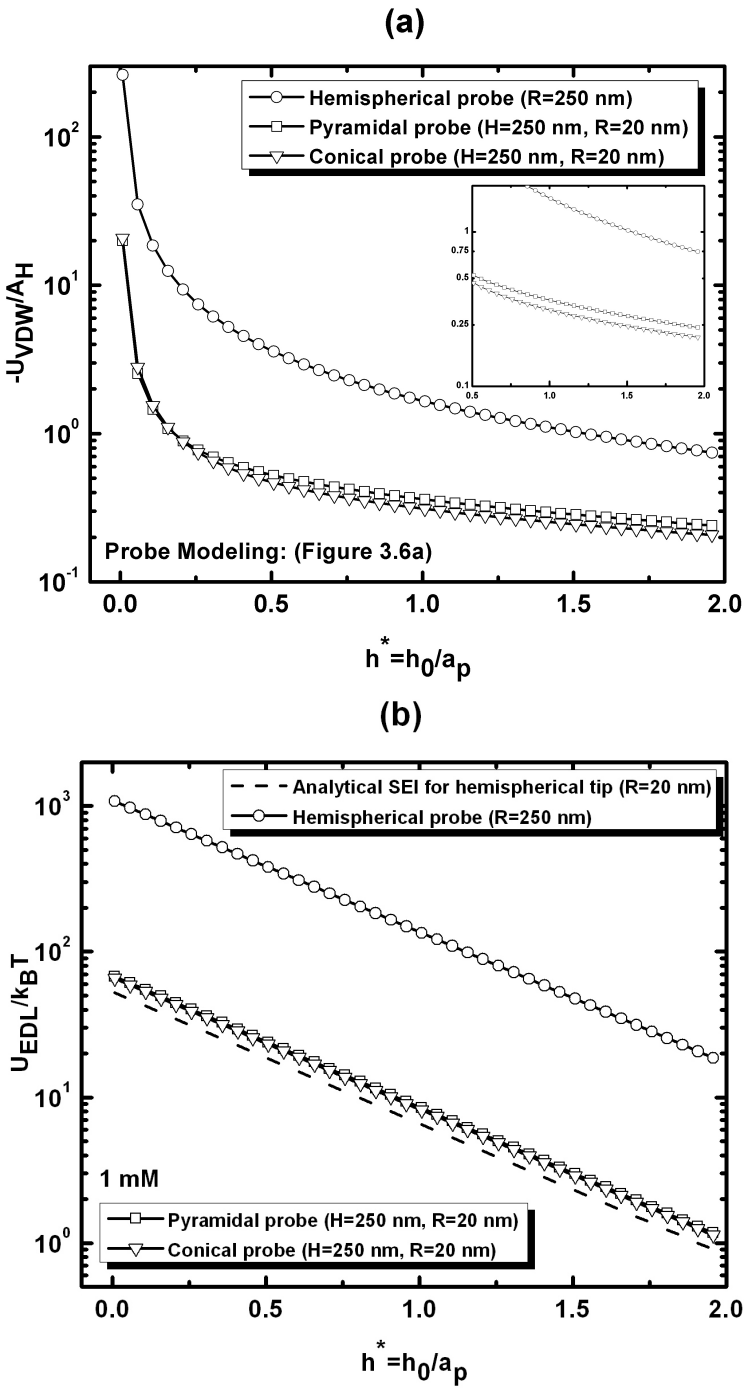

Figure 5.20: Comparison of **(a)**: van der Waals and **(b)**: electrostatic energies of hemispherical, pyramidal and conical model probes.

Before discussing about the two aforementioned approaches, Figure 5.20 depicts the difference between a pyramidal model with a conical and a hemispherical model. The first model is a hemisphere of radius of 250 nm. The second and third models are pyramidal and conical shapes, where their heads are modeled as a hemisphere with radii of 20 nm (first approach), while the total height of the model probes are 250 nm, and their wall angles are set to 45°. This is to the aim of making the size of the upper base of the pyramidal/conical probe equal to the hemispherical model. In the two plots of Figure 5.20, the interaction of the model probe against a smooth flat plate is numerically determined by employing SEI technique. It is observed that hemispherical model probe causes much larger interactions both in van der Waals and electrostatic energies. Pyramidal model also leads to higher interaction energy than the conical model, however their difference is more dominant in van der Waals interaction (see Figure 5.20a).

Figure 5.20b has depicted the electrostatic interactions for 1 mM electrolyte solution. In this figure, the interactions of the model probe are also compared against the analytically calculated interaction energy corresponding to a hemispherical tip of radius of 20 nm. This illustrates the significance of considering the upper pyramidal/conical structure into the calculations of electrostatic interaction energy. As a matter of fact, the small difference between the EDL energy of pyramidal/conical probe and the $R = 20$ nm small hemisphere declares that the EDL energy attenuates faster, and is less significant at larger separations.

The difference between using a sharp tip and a colloidal probe in AFM force measurement can also be explained in Figure 5.20, in that the energy profiles of the $R = 250$ nm hemispherical model probe can reasonably represent a colloidal probe where such a hemispherical particle is attached to a similar size pyramidal tip (see Figure 5.21a).

In Figures 5.22, and 5.23 the effects of varying the height and the side angles of a conical probe are depicted for van der Waals and electrostatic interaction energies respectively. The simulated probe for these results are modeled based

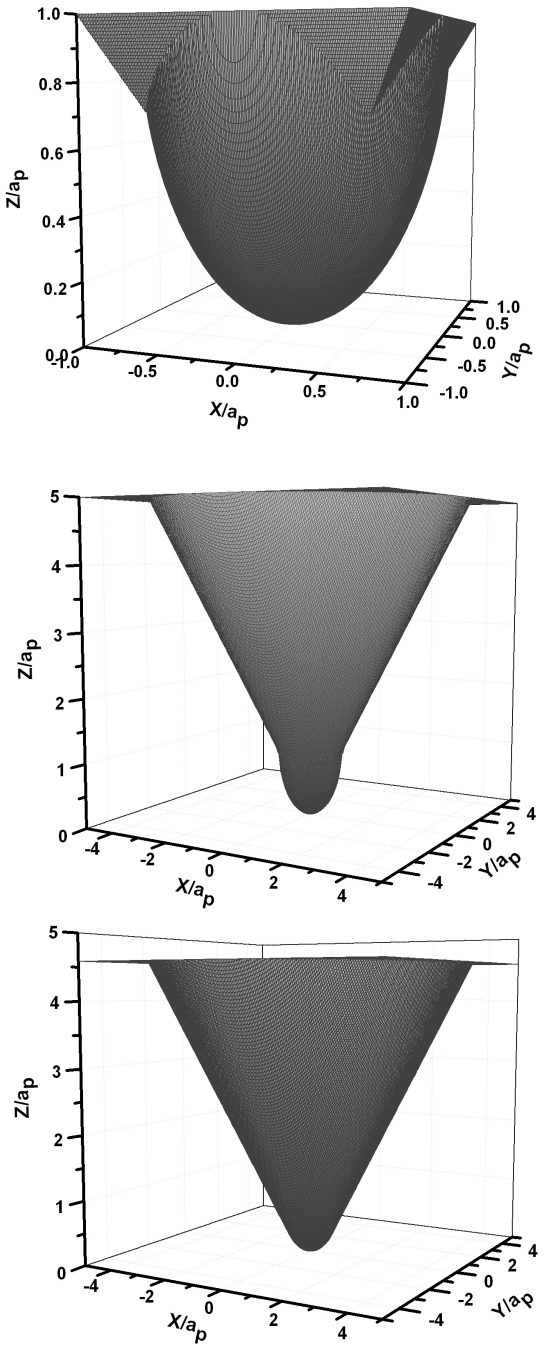

Figure 5.21: 3D schematic representing the simulated geometry for a **(a)**: colloidal probe, **(b)**: conical probe with hemispherical tip, and **(c)**: conical probe with truncated hemispherical tip.

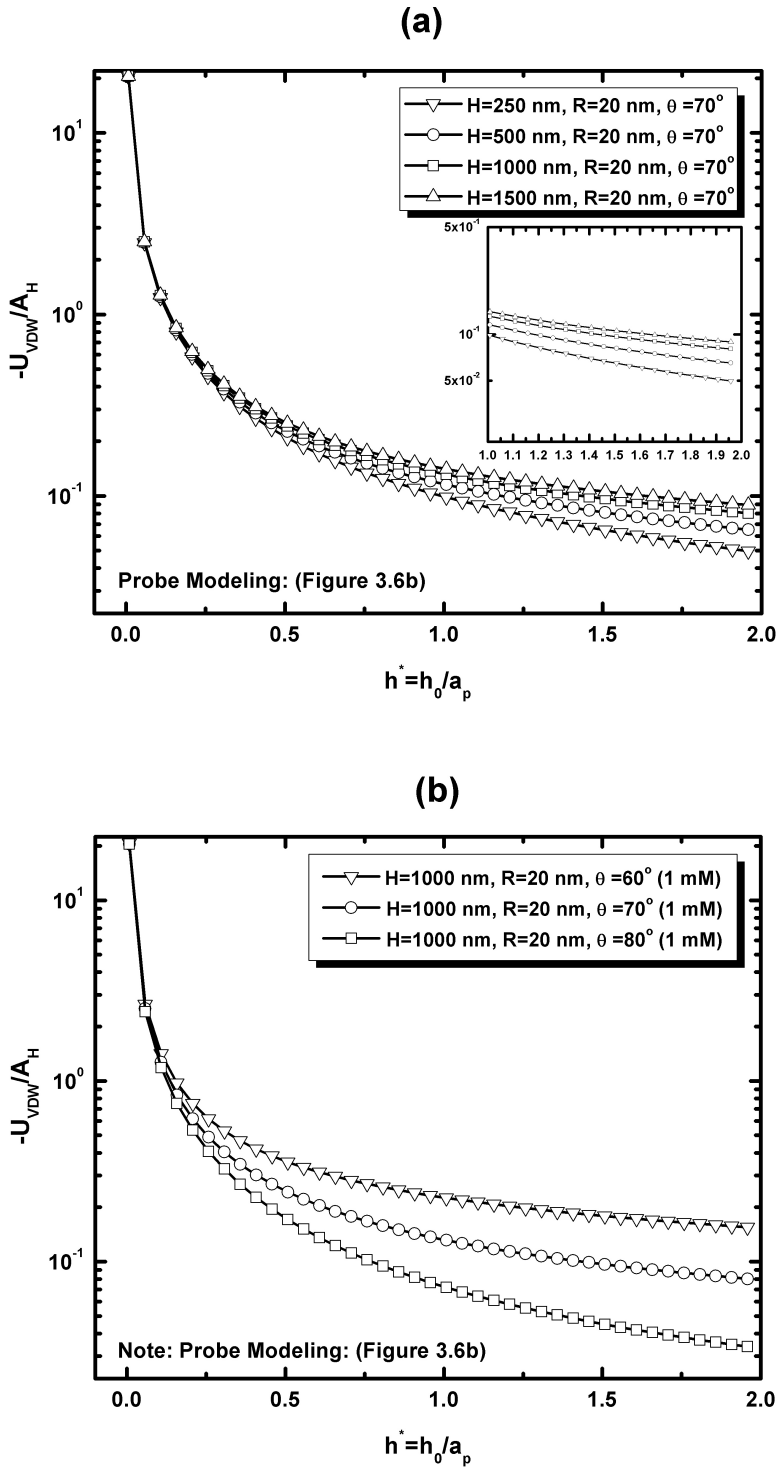

Figure 5.22: The numerical results assessing the effect of **(a)**: the height, and **(b)**: the wall angle of the modeled probe on the van der Waals interaction.

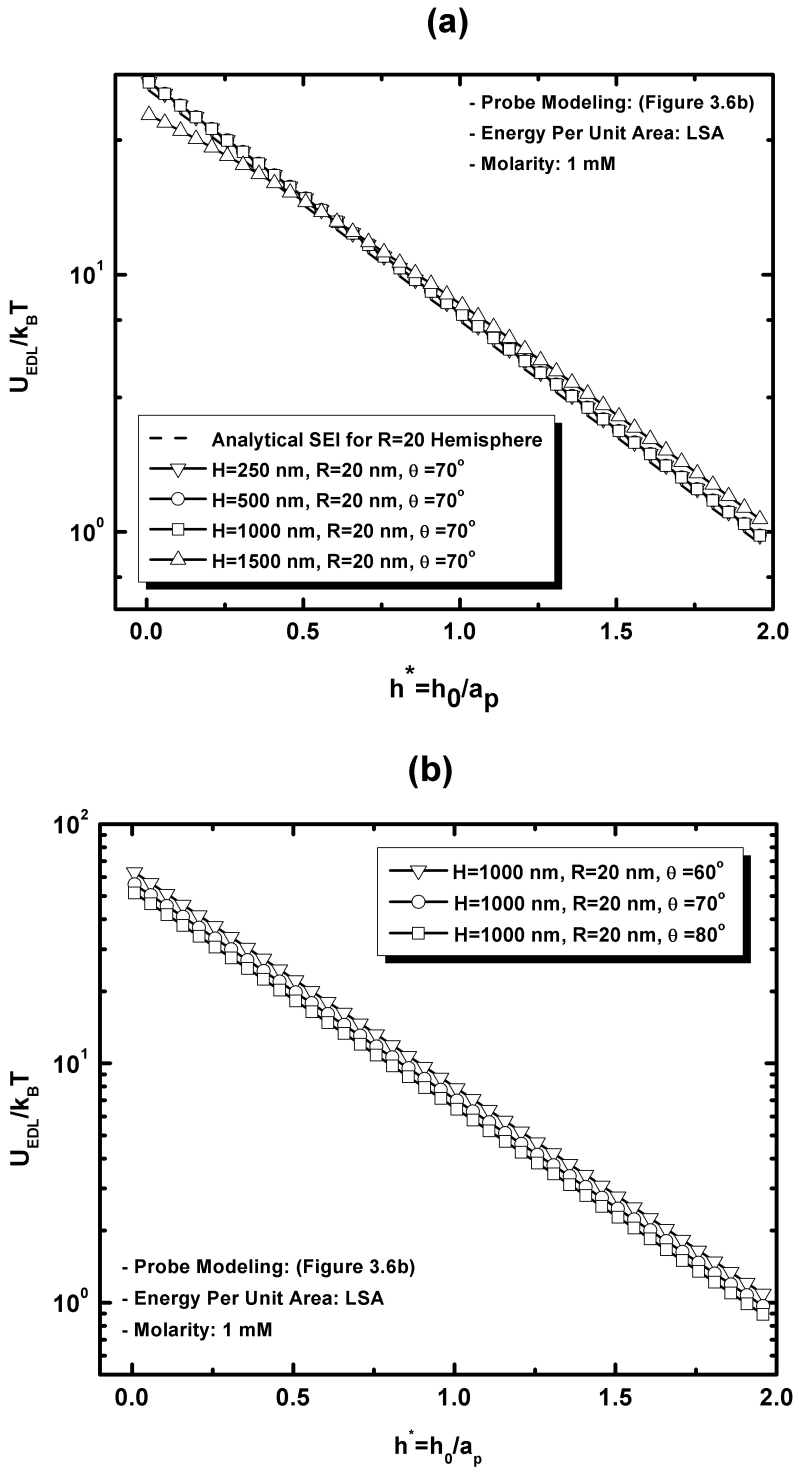

Figure 5.23: The numerical results assessing the effect of **(a)**: the height, and **(b)**: the wall angle of the modeled probe on the electrostatic interaction under 1 mM ionic concentration.

on the second approach (Figure 5.21c). The height effect is determined based on simulating the probes with different 250, 500, 1000 and 1500 nm vertical heights. Since the wall angle of the DNP-S20 probe was reported in chapter 4 to be almost 70°, the wall angles in the numerical analysis are considered to be 60°, 70°, and 80°. Figure 5.22a, clearly indicates that taller probe has more interaction with the surface. However, height effect becomes negligible as the height of the probe increases. Thus, it can be concluded that in the numerical modeling of a DNP-S20 probe, one may not need to model the entire geometry of the probe. Increasing the wall angle has also caused more interaction with the surface, as depicted in Figure 5.22b.

5.5 Summary

In this chapter, AFM force measurements were presented. In section 5.2.1 the force-distance plots obtained over glass, as a smooth flat substrate were discussed. The experiments were conducted under KCl (1:1) with ionic concentrations of 0.1 to 100 mM to evaluate the sensitivity of AFM on detecting the smaller forces at higher molarities of the electrolyte solution. AFM measurements generally followed the same trend as predicted by DLVO theory, in that by increasing the ionic concentration the Debye length decreases and the maximum peak in DLVO curve decreases. However, some discrepancy between the experimental and theoretical results still exists. On the other hand, the effect of surface roughness on colloidal interactions was experimentally revealed in section 5.2.2, by conducting AFM force measurement over 5 different rough surfaces. These surfaces provided good variety of physical heterogeneities, and therefore the AFM force measurements had different responses for each substrate. As predicted from literature, the magnitude of the interaction energies were generally attenuated in these tests. To ensure that this attenuation is caused due to the presence of surface roughness, a numerical calculation based on SEI technique was developed to simulate the AFM force measurement over one of the sample rough surfaces. In this simu-

lation, the AFM probe and the sample rough surface were modeled based on their real geometrical parameters. The results showed much better agreement with experimental measurement, than the DLVO calculation based on a flat surface. As a result, it was demonstrated that by considering the physical heterogeneities of the interacting surface, the interaction forces sensed by AFM probe can be much better described.

In section 5.3, the influence of surface roughness on DLVO interaction energy was clearly demonstrated by mathematically modeling rough surfaces with asperities in protruding and depressed forms. The interaction energy between a flat plate and a rough surface consisting the hemispherical, conical and cylindrical form of heterogeneities were comprehensively characterized based on the variation of size and pitch distance between the asperities. It was generally observed that protrusions behave oppositely to depressions in terms of increasing and decreasing the pitch distance. It was also shown that regardless of the separation distance, the electrostatic interactions, or any similar exponentially decaying interactions, will be attenuated to the same extent. It was observed that for protruding asperities, conical shapes caused the highest rate of the reduction in the interaction energy, followed by hemispherical and cylindrical shape asperities, respectively, at equal scaled separation distances. This order was exactly opposite in depressed form the asperities.

Numerical simulations in section 5.4 demonstrated that the interaction energy between the probe and the model rough surface vary with the change in lateral position of the probe. These analyses can be used to predict the variation of the experimental force measurements obtained from AFM. For symmetrically patterned surfaces, the energy distributions are also symmetric. Thus, a mathematical equation can be fit to the individual profiles of the energy distribution map, and hence to the distribution map itself. Generalizing this method will enable one to predict the topographical characteristics of the surface from the resulting energy distribution map and its corresponding fitted equations.

Finally, in section 5.4.2, apart from the surface roughness, the AFM probe

was modeled in a more precise manner, in order to be replaced with hemispherical model used in the previous numerical calculations. In this section, it was mainly attempted to investigate how different the modeling approaches, proposed in Chapter 3, are for simulating an AFM probe. Also, it was tried to show how the resulting interaction energies vary by changing the geometrical parameters in these simulations.

Chapter 6

Conclusions

6.1 Conclusions

The major conclusions that can be drawn from the present study are:

1. Surface roughness causes the van der Waals potential energy to be substantially reduced at shorter separation distances up to orders of magnitudes, whereas this effect is less pronounced as the separation distance increases, and even become insignificant at very high separations.

2. The influence of the surface roughness on the interaction energy increases by increasing the asperity size. This applies to all the different asperity shapes used in this study.

3. For protruding asperities, surfaces with lower roughness densities have reduced both the van der Waals and electrostatic energies up to higher extent, while this is opposite for depressed elements.

4. In contrast with van der Waals energy, surface roughness does not cause any change in electrostatic energy as a function of the separation distance between the surfaces. On the other hand, the electrostatic energy is diminished by increasing the inverse Debye length (or ionic concentration) of the intervening medium.

5. Conical shape asperities cause the most reduction in interaction energy, followed by spherical and cylindrical shapes, respectively, provided that

they are modeled as protrusions. This sequence is opposite for depressions.

6. Generally, the reduction in DLVO energy based on protrusions is more pronounced than the reduction based on the roughnesses in form of depression.

Further numerical investigations on DLVO interaction components reveal that the interaction between a model spherical probe is highly dependent on the relative lateral positions of the model probe and the surface. It is illustrated that the probe may experience much less interaction when it is located on top of an asperity, than when it is closer to the bottom flat area of a rough surface, even when the minimum separation distance between the probe and surface is identical in both cases. In another scenario, assuming that the probe is traversing over the surface, while separated with a constant distance from the surface base, the interaction energy is much higher when the probe is laterally closer to the asperities. These analyses apply for protruding elements, whereas for depressed elements these variations are opposite.

6.2 Future Work

The study presented in this research should be treated as an initial step toward a thorough understanding of the interfacial energies characterization over nano-structured surfaces in colloidal systems. Based on the results provided here, a few recommendations can be made, in order to more rigorously characterize the variation of colloidal energies based on the physical heterogeneities of the interacting surface.

1. During the experimental force measurements, the surface potentials of both of the probe and the substrate were assumed to be identically at -50 mV according to the previous literatures. This value was also used in the theoretical calculations. However, to more precisely quantify the

resulting force plots, the exact value of this quantity should be determined before or during the tests. Additionally, for examining the AFM sensitivity, as a following to the measurements under different ionic concentrations, one may also perform the measurements under electrolyte solutions with different pHs to find the effect of the solution acidity or basicity on the resulting forces.

2. Analytical derivations were based on the assumption that the approaching probe is a flat plate. Although these derivations could reasonably explain and characterize the influence of surface roughness, but for a more realistic scenario, the flat plate can be replaced by a spherical or any other more suitable shapes.

3. In the numerical simulations, developed for finding the distribution of DLVO energy over a rough surface, the asperities were modeled as hemispherical protrusions, uniformly patterned in a square lattice. This analysis can be generalized by considering other shape of asperities in form of protrusions or depressions, or a combination of these two. They can also be distributed in other forms, such as hexagonal lattice, and one can attempt to find the symmetry of the energy distribution for this patterning over the entire surface, by defining a new unit cell, and finding a set of new geometrical relations.

4. A mathematical equation was tried to be fitted to the 3D energy maps. These energy maps were obtained by conducting the simulation for a single separation distance between the probe and the sample surface. However, by repeating the simulations for different heights (separation distances), one may also add new parameters in the fitted equation that represent the existing separation distance. By generalizing the idea of fitting a mathematical equation to the energy maps, one then can use these equations to justify the topographical features of an unknown substrate, if the energy maps are available.

5. In the last stage of this research, the structure of AFM probe was attempted to be modeled according to its real geometrical size and parameters. It was shown that how the DLVO energy components may vary by increasing or decreasing some geometrical parameters, such as, the probe wall angle, the probe height, and weather the probe is modeled as a pyramid, cone or hemisphere. In these calculations, the model probe interaction was investigated over a model smooth flat surface. However, to achieve an even more realistic model in the investigation of the DLVO energy lateral distribution as a result the of probe movement, such a modeling for AFM probe can be replaced with the spherical probe, currently used in these analyses.

Bibliography

[Alerecht et al., 1990] Alerecht, T., Akamine, S., Carver, T., and Quate, C. (1990). Microfabrication of Cantilever Styli for the Atomic Force Microscope. *Journal of Vacuum Science & Technology A-Vacuum Surfaces and Films*, 8(4):3386–3396.

[Bell et al., 1970] Bell, G., Levine, S., and McCartney, L. (1970). Approximate Methods of Determining the Double-Layer Free Energy of Interaction between Two Charged Colloidal Spheres. *Journal of Colloids and Interface Science*, 33:335–359.

[Bhattacharjee and Elimelech, 1997] Bhattacharjee, S. and Elimelech, M. (1997). Surface Element Integration: A Novel Technique For Evaluation of DLVO Interaction Between a Particle And a Flat Plate. *Journal of Colloid and Interface Science*, 193(2):273–285.

[Bhattacharjee et al., 1998] Bhattacharjee, S., Ko, C., and Elimelech, M. (1998). DLVO Interaction Between Rough Surfaces. *Langmuir*, 14(12):3365–3375.

[Binnig et al., 1986] Binnig, G., Quate, C., and Gerber, C. (1986). Atomic Force Microscope. *Physical Review Letters*, 56(9):930–933.

[Bowen and Doneva, 2000] Bowen, W. and Doneva, T. (2000). Atomic Force Microscopy Studies of Membranes: Effect of Surface Roughness on Double-Layer Interactions and Particle Adhesion. *Journal of Colloid and Interface Science*, 229(2):544–549.

[Bowen et al., 2002] Bowen, W., Doneva, T., and Stoton, J. (2002). The Use of Atomic Force Microscopy to Quantify Membrane Surface Electrical Properties. *Colloids and Surfaces A Physiochemical And Engineering Aspects*, 201(1-3):73–83.

[Brant and Childress, 2002] Brant, J. and Childress, A. (2002). Assessing Short-Range Membrane-Colloid Interactions Using Surface Energetics. *Journal of Membrane Science*, 203(1-2):257–273.

[Brant et al., 2006] Brant, J., Johnson, K., and Childress, A. (2006). Examining the Electrochemical Properties of a Nanofiltration Membrane with Atomic Force Microscopy. *Journal of Membrane Science*, 276(1-2):286–294.

[Brunetti et al., 2010] Brunetti, V., Maiorano, G., Rizzello, L., Sorce, B., Sabella, S., Cingolani, R., and Pompa, P. P. (2010). Neurons Sense Nanoscale Roughness With Nanometer Sensitivity. *Proceeding of The National Academy of Sciences of The United States of America*, 107(14):6264–6269.

[Butt, 1991] Butt, H. (1991). Measuring Electrostatic, van der Waals, and Hydration Forces in Electrolyte-Solutions With an Atomic Force Microscope. *Biophysical Journal*, 60(6):1438–1444.

[Butt et al., 2003] Butt, H., Graf, K., and Kappl, M. (2003). *Physics and Chemistry of Interfaces*. Wiley.

[Butt et al., 1993] Butt, H., Siedle, P., Seifert, K., Fendler, K., Seeger, T., BamBerg, E., Weisenhorn, A., Goldie, K., and Engel, A. (1993). Scan Speed Limit in Atomic Force Microscopy. *Journal of Microscopy-Oxford*, 169(Part 1):75–84.

[Carnie and Chan, 1993] Carnie, S. and Chan, D. (1993). Interaction Free-Energy Between Identical Spherical Colloidal Particles - The Linearized Poisson-Boltzmann Theory. *Journal of Colloid and Interface Science*, 155(2):297–312.

[Chapel, 1994] Chapel, J. (1994). Electrolyte Species-Dependent Hydration Forces Between Silica Surfaces. *Langmuir*, 10(11):4237–4243.

[Choi et al., 2007] Choi, C.-H., Hagvall, S. H., Wu, B. M., Dunn, J. C. Y., Beygui, R. E., and Kim, C.-J. (2007). Cell Interaction With Three-Dimensional Sharp-Tip Nanotopography. *Biomaterials*, 28(9):1672–1679.

[Cleveland et al., 1993] Cleveland, J., Manne, S., Bocek, D., and Hansma, P. (1993). A Nondestructive Method for Determining the Spring Constant of

Cantilevers for Scanning Force Microscopy. *Review of Scientific Instruments*, 64(2):403–405.

[Considine and Drummond, 2001] Considine, R. and Drummond, C. (2001). Surface roughness and surface force measurement: A comparison of electrostatic potentials derived from atomic force microscopy and electrophoretic mobility measurements. *Langmuir*, 17(25):7777–7783.

[Cooper et al., 2001] Cooper, K., Gupta, A., and Beaudoin, S. (2001). Simulation of the Adhesion of Particles to Surfaces. *Journal of Colloid and Interface Science*, 234(2):284–292.

[de Souza et al., 2001] de Souza, E., Ceotto, G., and Teschke, O. (2001). Dielectric constant measurements of interfacial aqueous solutions using atomic force microscopy. *Journal of Molecular Catalysis A-Chemical*, 167(1-2):235–243. 2nd San Luis Conference on Surface Science and Catalysis, MAR DEL PLATA, ARGENTINA, APR 03-06, 2000.

[Derjaguin, 1934] Derjaguin, B. (1934). Analysis of Friction and Adhesion IV The Theory of The Adhesion of Small Particles. *Kolloid-Zeitschrift*, 69(2):155–164.

[Derjaguin and Landau, 1941] Derjaguin, B. and Landau, L. (1941). Theory of the stability of strongly charged lyophobic sols and of the adhesion of strongly charged particles in solution of electrolytes. *Acta Physiochim*, 14:633.

[Dorobantu et al., 2008] Dorobantu, L. S., Bhattacharjee, S., Foght, J. M., and Gray, M. R. (2008). Atomic Force Microscopy Measurement of Heterogeneity in Bacterial Surface Hydrophobicity. *Langmuir*, 24(9):4944–4951.

[Dorobantu et al., 2009] Dorobantu, L. S., Bhattacharjee, S., Foght, J. M., and Gray, M. R. (2009). Analysis of Force Interactions between AFM Tips and Hydrophobic Bacteria Using DLVO Theory. *Langmuir*, 25(12):6968–6976.

[Ducker et al., 1991] Ducker, W., Senden, T., and Pashley, R. (1991). Direct Measurement of Colloidal Forces Using An Atomic Force Microscope. *Nature*, 353(6341):239–241.

[Ducker et al., 1992] Ducker, W., Senden, T., and Pashley, R. (1992). Measurement of Forces In Liquids Using A Force Microscope. *Langmuir*, 8(7):1831–1836.

[Eichenlaub et al., 2006] Eichenlaub, S., Kumar, G., and Beaudoin, S. (2006). A Modeling Approach to Describe the Adhesion of Rough, Asymmetric Particles to Surfaces. *Journal of Colloid and Interface Science*, 299(2):656–664.

[Elimelech and O'Melia, 1990] Elimelech, M. and O'Melia, C. (1990). Effect of Particle-Size on Collision Efficiency in the Deposition of Brownian Particles With Electrostatic Energy Barriers. *Langmuir*, 6(6):1153–1163.

[Elimelech et al., 1997] Elimelech, M., Zhu, X., Childress, A., and Hong, S. (1997). Role of Membrane Surface Morphology in Colloidal Fouling of Cellulose Acetate and Composite Aromatic Polyamide Reverse Osmosis Membranes. *Journal of Membrane and Science*, 127(1):101–109.

[Giesbers, 2001] Giesbers, M. (2001). *Surface Forces Studied With Colloidal Probe Atomic Force Microscopy*. PhD thesis, Physical Chemistry and Colloid Science, Wageningen University.

[Gregory, 1973] Gregory, J. (1973). Approximate Expression for Interaction of Diffuse Electric Double-Layer at Constant Charge. *Journal of the Chemical Society-Faraday Transactions II*, 69(12):1723–1728.

[Gregory, 1975] Gregory, J. (1975). Interaction of Unequal Double-Layers at Constant Charge. *Journal of Colloid and Interface Science*, 51(1):44–51.

[Gregory, 1981] Gregory, J. (1981). Approximate Expressions For Retarded van der Waals Interaction. *Journal of Colloid and Interface Science*, 83(1):138–145.

[Hamaker, 1937] Hamaker, H. (1937). The London - Van Der Waals Attraction Between Spherical Particles. *Physica*, 4:1058–1072.

[Hoek and Agarwal, 2006] Hoek, E. and Agarwal, G. (2006). Extended DLVO interactions between spherical particles and rough surfaces. *Journal of Colloid and Interface Science*, 298(1):50–58.

[Hoek et al., 2003] Hoek, E., Bhattacharjee, S., and Elimelech, M. (2003). Effect of Membrane Surface Roughness on Colloid-Membrane DLVO Interactions. *Langmuir*, 19(11):4836–4847.

[Hogg et al., 1966] Hogg, R., Healy, T., and Fuersten.DW (1966). Mutual coagulation of colloidal dispersions. *Transactions of The Faraday Society*, 62(522P):1638–&.

[Horn et al., 1989] Horn, R., Smith, D., and Haller, W. (1989). Surface Forces And Viscosity of Water Measured Between Silica Sheets. *Chemical Physics Letters*, 162(4-5):404–408.

[Huang et al., 2010] Huang, X., Bhattacharjee, S., and Hoek, E. M. V. (2010). Is Surface Roughness a "Scapegoat" or a Primary Factor When Defining Particle-Substrate Interactions? *Langmuir*, 26(4):2528–2537.

[Hunter and White, 1987] Hunter, R. and White, L. (1987). *Foundation of Colloid Science*. Oxford University Press.

[Hutter and Bechhoefer, 1993] Hutter, J. and Bechhoefer, J. (1993). Calibration of Atomic Force Microscope Tips. *Review of Scientific Instruments*, 64(7):1868–1873.

[Israelachvili, 2007] Israelachvili, J. N. (2007). *Intermolecular and Surface Forces*. Academic Press.

[Janusz et al., 2003] Janusz, W., Patkowski, J., and Chibowski, S. (2003). Competitive adsorption of Ca2+ and Zn(II) ions at monodispersed SiO2/electrolyte solution interface. *Journal of Colloid and Interface Science*, 266(2):259–268.

[Johnson et al., 1971] Johnson, K., Kendall, K., and Roberts, A. (1971). Surface Energy and Contact of Elastic Solids. *Proceeding of the Royal Society of London Series A Mathematical and Physical Sciences*, 324(1558):301–&.

[Kang and Elimelech, 2009] Kang, S. and Elimelech, M. (2009). Bioinspired Single Bacterial Cell Force Spectroscopy. *Langmuir*, 25(17):9656–9659.

[Kappl and Butt, 2002] Kappl, M. and Butt, H. (2002). The colloidal probe technique and its application to adhesion force measurements. *Particle & Particle Systems Characterization*, 19(3):129–143.

[Kemps and Bhattacharjee, 2005] Kemps, J. and Bhattacharjee, S. (2005). Interactions between a Solid Spherical Particle and a Chemically Heterogeneous Planar Substrate. *Langmuir*, 21(25):11710–11721.

[Kihira and Matijevic, 1992] Kihira, H. and Matijevic, E. (1992). An Assessment of Heterocoagulation Theories. *Advances in Colloid and Interface Science*, 42:1–31.

[Kitching et al., 1999] Kitching, S., Williams, P., Roberts, C., Davies, M., and Tendler, S. (1999). Quantifying surface topography and scanning probe image reconstruction. *Journal of Vacuum Science & Technology*, 17(2):273–279.

[Liu, 2004] Liu, J. (2004). *Role of Colloidal Interactions in Bitumen Recovery from Oil Sands*. PhD thesis, Department of Chemical Engineering, University of Alberta.

[Liu et al., 2006] Liu, J. J., Zhang, L. Y., Xu, Z. H., and Masliyah, J. (2006). Colloidal interactions between asphaltene surfaces in aqueous solutions. *Langmuir*, 22(4):1485–1492.

[Martines et al., 2008] Martines, E., Csaderova, L., Morgan, H., Curtis, A. S. G., and Riehle, M. O. (2008). DLVO Interaction Energy Between a Sphere And a Nano-Patterned Plate. *Colloids and Surfaces A Physiochemical And Engineering Aspects*, 318(1-3):45–52.

[Masliyah and Bhattacharjee, 2006] Masliyah, J. and Bhattacharjee, S. (2006). *Electrokinetic and Colloid Transport Phenomena*. Wiley.

[McCormack et al., 1995] McCormack, D., Carnie, S., and Chan, D. (1995). Calculations of Electric Double-Layer Force and Interaction Free-Energy between Dissimilar Surfaces. *Journal of Colloid and Interface Science*, 169(1):177–196.

[Moxon et al., 2004] Moxon, K., Kalkhoran, N., Markert, M., Sambito, M., McKenzie, J., and Webster, J. (2004). Nanostructured Surface Modification of Ceramic-Based Microelectrodes to Enhance Biocompatibility For a Direct Brain-Machine Interface. *IEEE Transactions on Biomedical Engineering*, 51(6):881–889.

[Nermeister and Ducker, 1994] Nermeister, J. and Ducker, W. (1994). Lateral, Normal, and Longitudinal Spring Constants of Atomic-Force Microscopy Cantilevers. *Review of Scientific Instruments*, 65(8):2527–2531.

[O'Meila and Stumm, 1967] O'Meila, C. and Stumm, W. (1967). Theory of Water Filtration. *Journal of American Water Works Association*, 59:1393–1412.

[Palin et al., 2005] Palin, E., Liu, H., and Webster, T. (2005). Mimicking the Nanofeatures of Bone Increases Bone-Forming Cell Adhesion And Proliferation. *Nanotechnology*, 16(9):1828–1835.

[Press et al., 1992] Press, W. H., Teukolsky, S. A., Vetterling, W. T., and Flannery, B. P. (1992). *Numerical Recepies in FORTRAN*. Cambridge.

[Rajagopalan and Tien, 1979] Rajagopalan, R. and Tien, C. (1979). Theory of Deep Bed Filtration. *Progress in Filtration and Separation*, 1:179–269.

[Rizwan and Bhattacharjee, 2007] Rizwan, T. and Bhattacharjee, S. (2007). Initial deposition of colloidal particles on a rough nanofiltration membrane. *Canadian Journal of Chemical Engineering*, 85(5):570–579.

[Rizwan and Bhattacharjee, 2009] Rizwan, T. and Bhattacharjee, S. (2009). Particle Deposition onto Charge-Heterogeneous Substrates. *Langmuir*, 25(9):4907–4918.

[Russel et al., 1989] Russel, W., Saville, D., and Schowalter, W. (1989). *Colloidal Dispersions*. Cambridge University Press.

[Sader et al., 1995] Sader, J., Larson, I., Mulvaney, P., and White, L. (1995). Method for the Calibration of Atomic Force Microscope Cantilevers. *Review of Scientific Instruments*, 66(7):3789–3798.

[Sader and White, 1993] Sader, J. and White, L. (1993). Theoretical Analysis of the Static Deflection of Plates for Atomic Force Microscope Applications. *Journal of Applied Physics*, 74(1):1–9.

[Smith and Howard, 1994] Smith, S. and Howard, L. (1994). A Precision, Low-force Balance and Its Application to Atomic Force Microscope Probe Calibration. *Review of Scientific Instruments*, 65(4, Part 1):903–909.

[Suresh and Walz, 1996] Suresh, L. and Walz, J. (1996). Effect of Surface Roughness on The Interaction Energy Between a Colloidal Sphere And a Flat Plate. *Journal of Colloid and Interface Science*, 183(1):199–213.

[Torii et al., 1996] Torii, A., Sasaki, M., Hane, K., and Okuma, S. (1996). A method for determining the spring constant of cantilevers for atomic force microscopy. *Measurement Science & Technology*, 7(2):179–184.

[Valle-Delgado et al., 2005] Valle-Delgado, J., Molina-Bolivar, J., Galisteo-Gonzalez, F., Galvez-Ruiz, M., Feiler, A., and Rutland, M. (2005). Hydration forces between silica surfaces: Experimental data and predictions from different theories. *Journal of Chemical Physics*, 123(3).

[van Oss, 1993] van Oss, C. (1993). Acid-Base Interfacial Interactions in Aquous-Media. *Colloids and Surfaces A Physiochemical And Engineering Aspects*, 78:1–49.

[Verwey and Overbeek, 1948] Verwey, E. and Overbeek, J. (1948). *Theory of Stability of Lyophobic Colloids*. Elsevier.

[White, 1983] White, L. (1983). On The Deryaguin Approximation For The Interaction Of Macrobodies. *Journal of Colloid and Interface Science*, 95(1):286–288.

[Yao et al., 1971] Yao, K., Habibian, M., and O'Meila, C. (1971). Water and Waste Water Filtration: Concepts and Applications. *Environmental Science and Technology*, 5(11):1105–1112.

[Zhao, 2009] Zhao, H. (2009). *Role of Water Chemistry In Oil Sands Processes*. PhD thesis, Department of Chemical Engineering, University of Alberta.

[Zhao et al., 2008] Zhao, H., Bhattacharjee, S., Chow, R., Wallace, D., Masliyah, J. H., and Xu, Z. (2008). Probing Surface Charge Potentials of Clay Basal Planes and Edges by Direct Force Measurements. *Langmuir*, 24(22):12899–12910.

Appendix A

AFM Probe Spring Constant Calibration

Cantilever deflection is converted to force using Hooke's law:

$$F = -kZ \tag{A.1}$$

where F is force as a function of displacement (deflection) Z, and k is the spring constant of the cantilever. As mentioned in section 4.2.1 for AFM probes, DNP-S20 and RTESP7 series were used throughout this study, and Veeco NanoProbe^{TM} has specified the values of spring constants for these types of probes as indicated in table 4.1. However, there are various methods to measure the spring constant of cantilevers for AFM experiments. In this section some of these methods are briefly introduced.

The most obvious way to determine the spring constant, as proposed by Butt *et al.* [Butt et al., 1993], is to apply a known force to the end of the cantilever, and measure the resulting deflection. In another method, developed by Torii *et al.* [Torii et al., 1996], Smith and Howard [Smith and Howard, 1994], a large-scale cantilever with a known spring constant is used to apply an increasing force to the AFM cantilever. The deflection of both cantilevers can be measured by interferometry, and since the spring constant of the large-scale cantilever is accurately known, the spring constant of the AFM probe cantilever can be determined.

Other studies [Alerecht et al., 1990,Nermeister and Ducker, 1994,Sader and

White, 1993] have tried to calculate the spring constant based on the cantilever shape, dimension and material properties through the following expression:

$$k = -\left(\frac{t}{l}\right)^3 \frac{Ew}{4} \tag{A.2}$$

where E is the elastic modulus ($i.e.$, the Young's modulus of the bulk material), and t, l, and w are the the cantilever thickness, length and width respectively.

Apart from the static methods introduced in the previous two paragraphs, a number of attempts [Cleveland et al., 1993, Sader et al., 1995] have been made in order to determine the spring constant from the resonance frequency of the unloaded cantilever, or the shift in this frequency when the cantilever is loaded. In this regard, Cleveland [Cleveland et al., 1993] has proposed a method in which by calculating the resonance frequency of a loaded cantilever the spring constant is determined using the following relation.

$$\nu = \frac{1}{2\pi}\sqrt{\frac{k}{m+M}} \tag{A.3}$$

Here, ν is the resonance frequency, m is the mass of cantilever, and M is the added mass. Rearranging the Eqn. A.3, gives:

$$k = (M+m)(2\pi\nu)^2 \tag{A.4}$$

However, the most standard way for spring constant calibration in AFM experiments is thermal noise analysis [Hutter and Bechhoefer, 1993]. This analysis states that the free end of the cantilever is continuously fluctuating due to thermal vibration of the environment, and this energy is equivalent to the thermal energy of the cantilever due to its absolute temperature. This can be mathematically described using the following equation.

$$\frac{1}{2}k_B T = \frac{1}{2}k\langle q^2\rangle \tag{A.5}$$

where k_B is the Boltzmann constant, and q is the average value of the vertical deflection of the cantilever over a certain period of time. This technique is most

suited for soft cantilevers ($e.g.$, $thin-legged$ 205 μm DNP-S20 cantilever that were used throughout this study), which their fluctuation is more significant.

The methods described in this section are referred to as the most common techniques for spring constant calibration; however, since the spring constant values reported by Veeco NanoProbe^{TM} were sufficiently precise for the force analysis required in the present study, the obtained forces are achieved by relying on the values listed in Table 4.1 in Chapter 4.

Appendix B

MATLAB Codes

PROGRAM 1:

The following program generates a pyramidal shape probe.

```
%%%%%%%%%%%%%%%%%%%%%
 <<<THIS PROGRAM GENERATES THE
PYRAMIDAL PROBE>>>
%%%%%%%%%%%%%%%%%%%%%
clc, clear all, close all,

question=input('please enter 1 for "cut"
hemisphere, or 0 for "full"
hemispherical tip to be attached! : ');
H=1000;
t=70*(pi/180);  % the inside angle at base !
r=10;           % tip radius !
s=1;
i=1;
%%%%%%%%%%%%%%%%%%%%%
<<<PYRAMIDAL SECTION>>>
%%%%%%%%%%%%%%%%%%%%%
X=2*round(H*cot(t));
Y=2*round(H*cot(t));
for y=-Y/2:s:Y/2
   for x=-X/2:s:X/2
      if y>=x & y<-x
         tip(i,1)=x;
         tip(i,2)=y;
         tip(i,3)=-tan(t)*x;
      elseif y<x & y<=-x
         tip(i,1)=x;
         tip(i,2)=y;
         tip(i,3)=-tan(t)*y;
      elseif y<=x & y>-x
         tip(i,1)=x;
         tip(i,2)=y;
         tip(i,3)=tan(t)*x;
      elseif y>x & y>=-x
         tip(i,1)=x;
         tip(i,2)=y;
         tip(i,3)=tan(t)*y;
      end
      i=i+1;
   end
   [x,y]
end

if question==1
    tip(:,3)=tip(:,3)-(r*sin(t)*H/(X/2)-(r-
r*cos(t)));
end
plot3(tip(:,1),tip(:,2),tip(:,3),'.')
%%%%%%%%%%%%%%%%%%%%%
<<<HEMISPHERICAL SECTION>>>
%%%%%%%%%%%%%%%%%%%%%
i=1;
for y=-r:s:r
   for x=-round(sqrt(r^2 -
y^2)):s:round(sqrt(r^2-y^2))
      hsphere(i,1)=x;
      hsphere(i,2)=y;
      hsphere(i,3)=-sqrt(r^2-(x)^2-(y)^2);
      i=i+1;
   end
end
hsphere(:,1)=hsphere(:,1);
hsphere(:,2)=hsphere(:,2);
hsphere(:,3)=hsphere(:,3)+(r);
%%%%%%%%%%%%%%%%%%%%%
<<<CUTTING THE HEMISPHERE>>>
%%%%%%%%%%%%%%%%%%%%%
k=1;
for i=1:size(hsphere,1)
   if hsphere(i,3)<=r-r*cos(t)
      hsphere_c(k,1:3)=hsphere(i,1:3);
      k=k+1;
   end
end
figure
plot3(hsphere(:,1),hsphere(:,2),hsphere(:,3),
'.')
```

```
figure
plot3(hsphere_c(:,1),hsphere_c(:,2),
hsphere_c(:,3),'.r')
%%%%%%%%%%%%%%%%%%%%
<<<HEMISPHERICAL SECTION
ATTACHMENT TO PYRAMIDAL
SECTION>>>
%%%%%%%%%%%%%%%%%%%%
if question==1
   HSPHERE=hsphere_c;
else
   HSPHERE=hsphere;
end

for i=1:size(HSPHERE,1)
   for j=1:size(tip,1)
      if HSPHERE(i,2)==tip(j,2) &
HSPHERE(i,1)==tip(j,1)
         tip(j,3)=HSPHERE(i,3);
      end
      j=j+1;
   end
   i=i+1;
end

%%%%%%%%%%%%%%%%%%%%
<<<NONDIMENSIONALIZATION>>>
%%%%%%%%%%%%%%%%%%%%
tip=tip/r;
n=sqrt(size(tip,1));
for i=1:n
   TIP(i,1:n)=tip((i-1)*n+1:i*n,3);    %HT is
a square matrix.!
end
figure
[XX,YY] = meshgrid(-
round(H*cot(t))/r:s/r:round(H*cot(t))/r);
mesh(XX,YY,TIP,'EdgeColor','black');
 %%%%%%%%%%%%%%%%%%%%
```

PROGRAM 2:

The following program generates a conical shape probe.

```
%%%%%%%%%%%%%%%%%%%%
<<<THIS PROGRAM GENERATES THE
CONICAL PROBE>>>
%%%%%%%%%%%%%%%%%%%%
clc, clear all, close all,
question=input('please enter 1 for "cutted"
hemisphere, or 0 for "full"
hemispherical tip to be attached! : ');
H=1000;
t=70*(pi/180);    % the inside angle at base !
r=25;             % tip radius !
tt=pi/2-t; % half of the angle at the cone tip !
s=1;
i=1;
%%%%%%%%%%%%%%%%%%%%
<<<CONICAL SECTION>>>
%%%%%%%%%%%%%%%%%%%%
X=2*round(H*tan(tt));
Y=2*round(H*tan(tt));
for y=-Y/2:s:Y/2
   for x=-X/2:s:X/2
      cone(i,1)=x;
      cone(i,2)=y;
      if x^2+y^2<=(X/2)^2

cone(i,3)=sqrt((x^2+y^2)/(tan(tt))^2);
      else
      cone(i,3)=H;
      end
      i=i+1;
   end
   [x,y]
end
 if question==1
    cone(:,3)=cone(:,3)-(r*sin(t)*H/(X/2)-(r-
r*cos(t)));
 end
 plot3(cone(:,1),cone(:,2),cone(:,3),'.')
%%%%%%%%%%%%%%%%%%%%
<<<HEMISPHERICAL SECTION>>>
%%%%%%%%%%%%%%%%%%%%
i=1;
for y=-r:s:r
   if  rem(round(sqrt(r^2-y^2)),2)==0
      xx=round(sqrt(r^2-y^2));
      else
         xx=round(sqrt(r^2-y^2))+1;
   end
   for x=-xx:s:xx
      hsphere(i,1)=x;
      hsphere(i,2)=y;
      hsphere(i,3)=-sqrt(r^2-(x)^2-(y)^2);
      i=i+1;
   end
   [x,y]
end
hsphere(:,3)=hsphere(:,3)+(r);
%%%%%%%%%%%%%%%%%%%%
<<<CUTTING THE HEMISPHERE>>>
%%%%%%%%%%%%%%%%%%%%
```

```
k=1;
for i=1:size(hsphere,1)
   if hsphere(i,3)<=r-r*cos(t)
      hsphere_c(k,1:3)=hsphere(i,1:3);
      k=k+1;
   end
end
figure
plot3(hsphere(:,1),hsphere(:,2),hsphere(:,3),'.
')
figure
plot3(hsphere_c(:,1),hsphere_c(:,2),hsphere_
c(:,3),'.')
%%%%%%%%%%%%%%%%%%%%
<<<HEMISPHERICAL SECTION
ATTACHMENT TO PYRAMIDAL
SECTION>>>
%%%%%%%%%%%%%%%%%%%%
if question==1
   HSPHERE=hsphere_c;
else
   HSPHERE=hsphere;
end
for i=1:size(HSPHERE,1)
   for j=1:size(cone,1)
      if HSPHERE(i,2)==cone(j,2) &
HSPHERE(i,1)==cone(j,1)
         cone(j,3)=HSPHERE(i,3);
      end
      j=j+1;
   end
   i=i+1;
end
%%%%%%%%%%%%%%%%%%%%
<<<NONDIMENSIONALIZATION>>>
%%%%%%%%%%%%%%%%%%%%
cone=cone/r;
n=sqrt(size(cone,1));
for i=1:n
   CONE(i,1:n)=cone((i-1)*n+1:i*n,3);
%CONE is a square matrix.!
end
figure
[XX,YY] = meshgrid(-X/(2*r):s/r:X/(2*r));
mesh(XX,YY,CONE,'EdgeColor','black');
%%%%%%%%%%%%%%%%%%%%
```

PROGRAM 3:

The following program generates a rough surface consisting of hemispherical asperities arranged on a square lattice.

```
%%%%%%%%%%%%%%%%%%%%
<<<THIS PROGRAM GENERATES A
ROUGH SURFACE CONSISTING OF
HEMISPHERICAL ASPERITIES>>>
%%%%%%%%%%%%%%%%%%%%
clc, clear all, close all,

rr=20;   %'rr'=tip radius= 'r' in tip generator
subroutines.! ==> here: = asperity radius
(as)
r=250;
pitch=500;
s=2;  %step (Resolution)!
X=500;
Y=500;
i=1;
for b=1:Y/pitch
   if b==Y/pitch
      B=b*pitch;
   else B=b*pitch-1;
   end
   for y=(b-1)*pitch:s:B
      for a=1:X/pitch
         if a==X/pitch
            A=a*pitch;
         else A=a*pitch-1;
         end
         for x=(a-1)*pitch:s:A
            surf(i,1)=(x-X/2);
            surf(i,2)=(y-Y/2);
            surf(i,3)=-(sqrt(r^2-(x-(2*a-
1)*pitch/2)^2-(y-(2*b-1)*pitc
            h/2)^2));
            i=i+1;
         end
         [x,y]
      end
   end
end
for i=1:size(surf,1);
   if (surf(i,3))^2<0
      surf(i,3)=0;
   end
end
```

```
%%%%%%%%%%%%%%%%%%%%%
<<<NONDIMENSIONALIZATION>>>
%%%%%%%%%%%%%%%%%%%%%
surf=surf/rr;
surf(:,3)=surf(:,3)+(X/2)/rr;

n=sqrt(size(surf,1));
for i=1:n
   SURF(i,1:n)=surf((i-1)*n+1:i*n,3);
%SURF is a square matrix.!
end
[XX,YY] = meshgrid(-
X/(2*rr):s/(rr):X/(2*rr));
mesh(XX,YY,SURF,'EdgeColor','black');
% colormap hsv
% surf(XX,YY,SURF)
% plot(surf(:,1),surf(:,3),'-');
% figure
% plot3(surf(:,1),surf(:,2),surf(:,3),'.');
%%%%%%%%%%%%%%%%%%%%%
```

PROGRAM 4:

The following subroutine is used to calculate the electrostatic energy based on HHF expression.

```
%%%%%%%%%%%%%%%%%%%%%
function [Y]=electrostatic_HHF(X,R)
%%%%%%%%%%%%%%%%%%%%%
<<<R=r=scaling Radius Loaded From Main
Program>>>
%%%%%%%%%%%%%%%%%%%%%
ep=(6.95*10^-10);
% ep=C/(V.m) = 10^-9 * C/(V.nm)
M=.1e-3;
kappa=(((3.04/(sqrt(M)))*10^-10)^-1);
% k=1/m = 10^-9 * 1/nm
v=1;
e=(1.602*10^-19);
KB=1.381*10^-23;
shai1=-50*10^-3;
shai2=shai1;
shai=shai1;
T=298;

A=(ep*kappa)*(R*1e-9)^2/2;
B=shai1^2+shai2^2;
C=2*shai1*shai2;
kappa_nm=kappa*1e-9;
for i=1:size(X,1)
   for j=1:size(X,2)
      Y(i,j)=A*(B*(1-
coth(kappa_nm*R*X(i,j)))+C*csch(kappa_n
m*R*X(i,j)));
   end
end
%%%%%%%%%%%%%%%%%%%%%
```

PROGRAM 5:

The following subroutine is used to calculate the electrostatic energy based on LSA expression.

```
%%%%%%%%%%%%%%%%%%%%%
function [Y]=electrostatic_LSA(X,R)
ep=(6.95*10^-10);
% ep=C/(V.m) = 10^-9 * C/(V.nm)
M=.1e-3;
kappa=((3.04/(sqrt(M))*10^-10)^-1);
% k=1/m = 10^-9 * 1/nm
v=1;
e=(1.602*10^-19);
KB=1.381*10^-23;
shai1=-50*10^-3;
shai2=shai1;
shai=shai1;
T=298;

A=32*(ep*kappa)*(R*1e-
9)^2*tanh(v*e*shai1/(4*KB*T))*tanh(v*e*
shai2/(4*KB*T)
)*(KB*T/(v*e))^2;
for i=1:size(X,1)
   for j=1:size(X,2)
      Y(i,j)=A*exp(-kappa*R*1e-9*X(i,j));
   end
end
%%%%%%%%%%%%%%%%%%%%%
```

PROGRAM 6:

The following program is for the flowchart in Figure 3.10 (for van der Waals energy).

```
%%%%%%%%%%%%%%%%%%
<<<THIS PROGRAM CALCULATE THE
VAN DER WAALS INTERACTION
ENERGY BETWEEN TWO IMPORTED
GEOMETRY AS A FUNCTION OF
THEIR SEPARATION DISTANCE.
REFER TO THE
FLOWCHART IN FIGURE 3.10.>>>
%%%%%%%%%%%%%%%%%%
clc, clear all, close all,
format long
load('..\probe.mat');
load("..\surface.mat');

x=-X/(2*r):s/r:X/(2*r);
y=-Y/(2*r):s/r:Y/(2*r);

%%%%%%%%%%%%%%%%%%%%%
<<<INTERACTION ENERGY
PARAMETERS>>>
%%%%%%%%%%%%%%%%%%%%%

AH=2.258*10^-20;

%%%%%%%%%%%%%%%%%%%%%
<<<CHECK THE "TIP" AND "SURFACE"
MATRICES SIZE AND ELEMENT>>>
%%%%%%%%%%%%%%%%%%%%%
if size(tip)~=size(surf)
   disp('size of the matrices are not equal')
   fprintf('\n size of surface matrix is %3.2f
by %3.2f:\n',size(surf,1),
   size(surf,2))
   fprintf('\n while size of tip matrix is %3.2f
by %3.2f:\n',size(tip,1),
   size(tip,2))
end

for i=1:size(tip,1)
   if surf(i,1)~=tip(i,1) | surf(i,2)~=tip(i,2)
      fprintf('\n The matrices X or Y are not
equal at row %3.2f !\n',i)
      fprintf('\n surface coordination at row
%3.2f is:\n %3.2f %3.2f !\n
      ',i,surf(i,1),surf(i,2))
      fprintf('\n tip coordination at row %3.2f
is:\n %3.2f %3.2f !\n',i,
      tip(i,1),tip(i,2))
   end
end
fprintf('\n <<<IN THIS PROGRAM>>>: \n
THE SCALING RADIUS IS: %3.2f nm \n
THE STRUCTURE RESOLUTION IS:
%3.2f nm \n \n',r,s)
%%%%%%%%%%%%%%%%%%%%%%
<<<HEIGHT MATRIX, ENERGY
PRIMARY MATRIX>>>
%%%%%%%%%%%%%%%%%%%%%%
height(:,1:2)=tip(:,1:2);

vw=input('Please enter "1" for calculating
Van der Waals ENERGY, "2" for
calculating the van der Waals FORCE: ');
analytical=input('Please enter "1" to TURN
ON, or "0" to TURN OFF the
analytical results: ');
step=input('Please enter the separation step
in (nm): ');
%%%%%%%%%%%%%%%%%%%%%
<<<SEPERATION LOOP>>>
%%%%%%%%%%%%%%%%%%%%%
k=1;
for hh=0.158/r:step/r:(2*r)/r
%"hh" is the actual separation !
   for i=1:size(tip,1)
      height(i,3)=(tip(i,3)-surf(i,3))+hh;
   end
   n=sqrt(size(height,1));
   for i=1:n
      HT(i,1:n)=height((i-1)*n+1:i*n,3);
%HT is a square matrix.!
   end
   if vw==1
      VW=van_der_waals(HT);
%=-U*12*pi/AH
   else if vw==2
         VW=Force_van_der_waals(HT);
%=-F*6*pi/AH
      end
   end


%%%%%%%%%%%%%%%%%%%%%
<<<INTEGRATION>>>
%%%%%%%%%%%%%%%%%%%%%
   for i=1:size(VW,1)
      int_x(i)=trapz(x,VW(i,:));
   end
   int_y(k,1)=hh;
   int_y(k,2)=trapz(y,int_x);
```

```
   if vw==1
        int_y(k,2)=(int_y(k,2)-((4-
pi)/(1+hh)^2))/(12*pi);
   else if vw==2
        int_y(k,2)=-
(int_y(k,2))/(6*pi)*AH*1e18;
      end
   end
   SEI(k,1)=hh;
   SEI(k,2)=1/6*(1/hh+log(hh/(1+hh)));
%=-Uvw/AH

   Hamaker(k,1)=hh;

Hamaker(k,2)=1/6*(1/hh+1/(hh+2)+log(hh/(
hh+2)));

   DA(k,1)=hh;
   DA(k,2)=1/(6*hh);
   k=k+1;
   hh
end

n=sqrt(size(surf,1));
for i=1:n
   SURF(i,1:n)=surf((i-1)*n+1:i*n,3);
%SURF is a square matrix.!
   TIP(i,1:n)=tip((i-1)*n+1:i*n,3);
%TIP is a square matrix.!
end

semilogy(int_y(:,1),int_y(:,2),'b^');
if analytical==1
   hold on
   semilogy(SEI(:,1),SEI(:,2),'r');
   semilogy(Hamaker(:,1),Hamaker(:,2),'k--
');
   semilogy(DA(:,1),DA(:,2),'g-.');
end
xlabel('h/r')
if vw==1
   ylabel('-U/AH')
else
   ylabel('nN')
end
%%%%%%%%%%%%%%%%%%%%
```

PROGRAM 7:

The following program is for the flowchart in Figure 3.12 (for electrostatic energy).

```
%%%%%%%%%%%%%%%%%%%%
<<<THIS PROGRAM CALCULATES
THE ELECTROSTATIC INTERACTION
ENERGY BETWEEN TWO IMPORTED
GEOMETRY, SEPARATED WITH A
CAERTAIN DISTANCE, AS THE PROBE
CHANGES ITS LATERAL POSITION
OVER THE SURFACE. REFER TO
THEFLOWCHART IN FIGURE 3.12.>>>
%%%%%%%%%%%%%%%%%%%%
clc, clear all, close all,

format long
load('..\probe.mat');
load('..\surface.mat');

x=-X/(2*r):s/r:X/(2*r);
y=-Y/(2*r):s/r:Y/(2*r);
%%%%%%%%%%%%%%%%%%%%
<<<INTERACTION ENERGY
PARAMETERS>>>
%%%%%%%%%%%%%%%%%%%%
KB=1.381*10^-23;
T=298;
%%%%%%%%%%%%%%%%%%%%
<<<CHECK THE "TIP" AND "SURFACE"
MATRICES SIZE AND ELEMENT>>>
%%%%%%%%%%%%%%%%%%%%
if size(tip)~=size(surf)
   disp('size of the matrices are not equal')
   fprintf('\n size of surface matrix is %3.2f
by %3.2f:\n',size(surf,1),
   size(surf,2))
   fprintf('\n while size of tip matrix is %3.2f
by %3.2f:\n',size(tip,1),
   size(tip,2))
end
for i=1:size(tip,1)
   if surf(i,1)~=tip(i,1) | surf(i,2)~=tip(i,2)
      fprintf('\n The matrices X or Y are not
equal at row %3.2f !\n',i)
      fprintf('\n surface coordination at row
%3.2f is:\n %3.2f %3.2f !\
      n',i,surf(i,1),surf(i,2))
      fprintf('\n tip coordination at row %3.2f
is:\n %3.2f %3.2f !\n',i,
      tip(i,1),tip(i,2))
```

```
   end
end
%%%%%%%%%%%%%%%%%%%%
<<<HEIGHT MATRIX, ENERGY
PRIMARY MATRIX>>>
%%%%%%%%%%%%%%%%%%%%
height(:,1:2)=tip(:,1:2);
double_layer=input('please enter 1 for
calculating HHF (Energy), 2 for LSA
(Energy), 3 for HHF based force! : ');
Xs=pitch/(2*r);    %nondimensionalized
(w.r.t) r (asperity size) !
Ys=pitch/(2*r);    %nondimensionalized
(w.r.t) r (asperity size) !

for ii=0:pitch/(2*s)
   for jj=0:pitch/(2*s)
      TIP_D=circshift(TIP,[ii,jj]);
%TIP_D = TIP_Dynamic !

      Xp=0+(jj*s)/r;  %nondimensionalized
(w.r.t) r (asperity size) !
      Yp=0+(ii*s)/r;  %nondimensionalized
(w.r.t) r (asperity size) !

      X0=abs(Xs-Xp);  %center to center
distance
      Y0=abs(Ys-Yp);  %center to center
distance
      if rp>1/2*(pitch^2/(2*r)-r)
         Z_r=-rp/r+sqrt((1+rp/r)^2-(X0)^2-
(Y0)^2);
      else if
sqrt(X0^2+Y0^2)>=sqrt(r^2+2*rp*r)
% sqrt(X0^2+Y0^2)=R
            Z_r=0;
         else
            Z_r=-rp/r+sqrt((1+rp/r)^2-(X0)^2-
(Y0)^2);
         end
      end

      TIP_D=TIP_D+Z_r;

%%%%%%%%%%%%%%%%%%%%
<<<SEPERATION LOOP>>>
%%%%%%%%%%%%%%%%%%%%
      for hh=100/r:100/r:100/r
%"hh" is the actual separation !
         for i=1:size(TIP,1)
            for j=1:size(TIP,2)
               HT(i,j)=TIP_D(i,j)-
SURF(i,j)+hh;
            end
         end
         if double_layer==1
            elec=electrostatic_HHF(HT,r);
%=-U*12*pi/AH
         else if double_layer==2
               elec=electrostatic_LSA(HT,r);
            else if double_layer==3

elec=Force_electrostatic_HHF(HT,r);
               end
            end
         end
%%%%%%%%%%%%%%%%%%%%
<<<INTEGRATION>>>
%%%%%%%%%%%%%%%%%%%%
         for i=1:size(elec,1)
            int_x(i)=trapz(x,elec(i,:));
         end
         int_y(ii+1,jj+1)=trapz(y,int_x);
         if double_layer==1 |
double_layer==2

int_y(ii+1,jj+1)=(int_y(ii+1,jj+1))/(KB*T);
         end
         if double_layer==3

int_y(ii+1,jj+1)=(int_y(ii+1,jj+1))*1e10;
         end
      end
   end
   [ii,jj]
end
for i=1:size(int_y,1)
   for j=1:size(int_y,2)
      int1=int_y;
      int2(i,j)=int_y(i,size(int_y,2)+1-j);
      int3(i,j)=int_y(size(int_y,1)+1-i,j);
      int4(i,j)=int_y(size(int_y,1)+1-
i,size(int_y,2)+1-j);
   end
end
int(1:size(int_y,1),1:size(int_y,2))=int4;
int(size(int_y,1)+1:2*size(int_y,1),1:size(int
_y,2))=int2;
int(1:size(int_y,1),size(int_y,2)+1:2*size(int
_y,2))=int3;
int(size(int_y,1)+1:2*size(int_y,1),size(int_y
,2)+1:2*size(int_y,2))=int1;

%%%%%%%%%%%%%%%%%%%%
4,2,3,1 :::::::::::::: 1,3,2,4
%%%%%%%%%%%%%%%%%%%%

profile0(1:size(int,1),1)=-(size(int,1)-
1)/2*s/r:s/r:(size(int,1)-1)/2*s/r;
```

```
profile0(1:size(int,1),2)=int(size(int,1)/2,1:si
ze(int,1));

profile45(1:size(int,1),1)=-(size(int,1)-
1)/2*s*sqrt(2)/r:s*sqrt(2)/r:(size
(int,1)-1)/2*s*sqrt(2)/r;
k=1;
for i=1:size(int,1)
   profile45(k,2)=int(i,i);
   k=k+1;
end
figure
plot(profile0(:,1),profile0(:,2),'r')
hold on
plot(profile45(:,1),profile45(:,2),'b')
figure
contourf(int)
[XX,YY]=meshgrid(1:size(int_y,1));
clear surf
figure
surf(int)
%%%%%%%%%%%%%%%%%%%%
```

PROGRAM 8:

Variance-Gamma function

```
%%%%%%%%%%%%%%%%%%%%
<<<VARIANCE-GAMMA FUNCTION
THAT IS USED IN LEVENBERG-
MARQUARDT ALGORITHM>>
%%%%%%%%%%%%%%%%%%%%
function r = vg(z)
alfa=z(1);
lambda=z(2);
base=z(3);
mu=0;
betta=0;
gama=sqrt(alfa.^2-betta.^2);

load('..\profile.txt');
r=[];
for j=1:size(profile,1)
       x= profile (j,1);
       y= profile (j,2);
   r=[r;((gama.^(2*lambda).*abs(x-
mu).^(lambda-0.5).*besselk(lambda-
0.5,alfa.*abs(x-
mu)))/(sqrt(pi)*gamma(lambda).*(2*alfa).^(
lambda-0.5)).*exp(betta.*(x-mu))+base*(x-
mu)^2-y)];
end
%%%%%%%%%%%%%%%%%%%%
```